

Jordan Journal of
P H Y S I C S

An International Peer-Reviewed Research Journal

Volume 2, No. 2, 2009, 1430 H

Jordan Journal of Physics (JJP): An International Peer-Reviewed Research Journal established by the Higher Research Committee, Ministry of Higher Education & Scientific Research, Jordan, and published quarterly by the Deanship of Research & Graduate Studies, Yarmouk University, Irbid, Jordan.

EDITOR-IN-CHIEF:

Ibrahim O. Abu Al-Jarayesh

Department of Physics, Yarmouk University, Irbid, Jordan.
ijaraysh@yu.edu.jo

EDITORIAL BOARD:

Dia-Eddin M. Arafah

Department of Physics, University of Jordan, Amman, Jordan.
darafah@ju.edu.jo

Nabil Y. Ayoub

German Jordanian University, Amman, Jordan.
nabil.ayoub@gju.edu.jo

Hisham B. Ghassib

President: Princess Sumaya University for Technology, Amman, Jordan.
ghassib@psut.edu.jo

Jamil M. Khalifeh

Department of Physics, University of Jordan, Amman, Jordan.
jkhalifa@ju.edu.jo

Sami H. Mahmood

Department of Physics, Yarmouk University, Irbid, Jordan.
mahmoods@yu.edu.jo

Marwan S. Mousa

Department of Physics, Mu'tah University, Al-Karak, Jordan.
mmousa@mutah.edu.jo

Nihad A. Yusuf

Department of Physics, Yarmouk University, Irbid, Jordan.
nihadyusuf@yu.edu.jo

EDITORIAL SECRETARY: Majdi Al-Shannaq.

Manuscripts should be submitted to:

Prof. Ibrahim O. Abu Al-Jarayesh
Editor-in-Chief, Jordan Journal of Physics
Deanship of Research and Graduate Studies
Yarmouk University-Irbid-Jordan
Tel. 00 962 2 7211111 Ext. 3735
E-mail: jjp@yu.edu.jo
Website: <http://Journals.yu.edu.jo/jjp>
<http://jjp.yu.edu.jo>

Jordan Journal of
P H Y S I C S

An International Peer-Reviewed Research Journal

Volume 2, No. 2, 2009, 1430 H

INTERNATIONAL ADVISORY BOARD

Prof. Dr. Ahmad Saleh

Department of Physics, Yarmouk University, Irbid, Jordan.
salema@yu.edu.jo

Prof. Dr. Aurore Savoy-Navarro

LPNHE Université de Paris 6/IN2P3-CNRS, Tour 33, RdC 4,
Place Jussieu, F 75252, Paris Cedex 05, France.
aurore@lpnhep.in2p3.fr

Prof. Dr. Bernard Barbara

Laboratoire Louis Neel, Salle/Room: D 108, 25, Avenue des
Martyrs BP 166, 38042-Grenoble Cedex 9, France.
Barbara@grenoble.cnrs.fr

Prof. Dr. Bruno Guiderdoni

Observatoire Astronomique de Lyon, g, avenue Ch. Antre-F-69561,
Saint Genis Laval Cedex, France.
Bruno.guiderdoni@olos.univ-lyon1.fr

Prof. Dr. Buford Price

Physics Department, University of California, Berkeley, CA 94720,
U. S. A.
bprice@berkeley.edu

Prof. Dr. Colin Cough

School of Physics and Astronomy, University of Birmingham, B15
2TT, U. K.
c.gough@bham.ac.uk

Prof. Dr. Desmond Cook

Department of Physics, Condensed Matter and Materials Physics
Research Group, Old Dominion University, Norfolk, Virginia
23529, U. S. A.
Dcook@physics.odu.edu

Prof. Dr. Evgeny Sheshin

MIPT, Institutskij per. 9, Dogoprudnyi 141700, Russia.
sheshin@lafeet.mipt.ru

Prof. Dr. Hans Ott

Laboratorium fuer Festkorperphysik, ETH Honggerberg, CH-
8093 Zurich, Switzerland.
ott@solid.phys.ethz.ch

Prof. Dr. Herwig Schopper

President SESAME Council, Chairman Scientific Board UNESCO
IBSP Programme, CERN, 1211 Geneva, Switzerland.
Herwig.Schopper@cern.ch

Prof. Dr. Humam Ghassib

Department of Physics, Jordan University, Amman, Jordan.
humam@atf.org.jo

Prof. Dr. Ingo Hofmann

GSI Darmstadt, Planckstr. 1, 64291, Darmstadt, Germany.
i.hofmann@gsi.de

Prof. Dr. Jozef Lipka

Department of Nuclear Physics and Technology, Slovak University
of Technology, Bratislava, Ilkovicova 3, 812 19 Bratislava,
Slovakia.
Lipka@elf.stuba.sk

Prof. Dr. Khalid Touqan

Chairman of Jordan Atomic Energy Commission, Amman, Jordan.

Prof. Dr. Mark J. Haggmann

Desert Electronics Research Corporation, 762 Lacey Way, North
Salt Lake 84064, Utah, U. S. A.
MHaggmann@NewPathResearch.Com

Prof. Dr. Nasr Zubeidey

President: Al-Zaytoonah University of Jordan, Amman, Jordan.
President@alzaytoonah.edu.jo

Prof. Dr. Patrick Roudeau

Laboratoire de l'Accelérateur, Lineaire (LAL), Université Paris-
Sud 11, Batiment 200, 91898 Orsay Cedex, France.
roudeau@mail.cern.ch

Prof. Dr. Paul Chu

Department of Physics, University of Houston, Houston, Texas
77204-5005, U. S. A.
Ching-Wu.Chu@mail.uh.edu

Prof. Dr. Peter Dowben

Nebraska Center for Materials and Nanoscience, Department of
Physics and Astronomy, 255 Behlen Laboratory (10th and R
Streets), 116 Brace Lab., P. O. Box 880111, Lincoln, NE 68588-
0111, U. S. A.
pdowben@unl.edu

Prof. Dr. Peter Mulser

Institute fuer Physik, T.U. Darmstadt, Hochschulstr. 4a, 64289
Darmstadt, Germany.
Peter.mulser@physik.tu-darmstadt.de

Prof. Dr. Rasheed Azzam

Department of Electrical Engineering, University of New Orleans
New Orleans, Louisiana 70148, U. S. A.
razzam@uno.edu

Prof. Dr. Richard G. Forbes

University of Surrey, Advanced Technology Institute (BB), School
of Electronics and Physical Sciences, Guildford, Surrey GU2 7XH,
U. K.
R.Forbes@surrey.ac.uk

Prof. Dr. Roy Chantrell

Physics Department, York University, York, YO10 5DD, U. K.
Rc502@york.ac.uk

Prof. Dr. Shawqi Al-Dallal

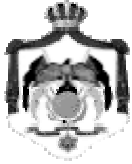
Department of Physics, Faculty of Science, University of Bahrain,
Manamah, Kingdom of Bahrain.

Prof. Dr. Susamu Taketomi

Matsumoto Yushi-Seiyaku Co. Ltd., Shibukawa-Cho, Yao City,
Osaka 581-0075, Japan.
staketomi@hotmail.com

Prof. Dr. Wolfgang Nolting

Institute of Physics / Chair: Solid State Theory, Humboldt-
University at Berlin, Newtonstr. 15 D-12489 Berlin, Germany
Wolfgang.nolting@physik.hu-berlin.de



The Hashemite Kingdom of Jordan



Yarmouk University

Jordan Journal of
PHYSICS
An International Peer-Reviewed Research Journal

Volume 2, No. 2, 2009, 1430 H

Instructions to Authors

Instructions to authors concerning manuscript organization and format apply to hardcopy submission by mail, and also to electronic online submission via the Journal homepage website (<http://jjp.yu.edu.jo>).

Manuscript Submission

1- **Hardcopy:** The original and three copies of the manuscript, together with a covering letter from the corresponding author, should be submitted to the Editor-in-Chief:

Professor Ibrahim O. Abu Al-Jarayesh
Editor-in-Chief, Jordan Journal of Physics
Deanship of Scientific Research and Graduate Studies
Yarmouk University, Irbid, Jordan.
Tel: 00962-2-7211111, Ext. 3735
Fax: 00962-2-7211121
E-mail: jjp@yu.edu.jo

2- **Online:** Follow the instructions at the journal homepage website.

Original *Research Articles*, *Communications* and *Technical Notes* are subject to critical review by minimum of two competent referees. Authors are encouraged to suggest names of competent reviewers. *Feature Articles* in active Physics research fields, in which the author's own contribution and its relationship to other work in the field constitute the main body of the article, appear as a result of an invitation from the Editorial Board, and will be so designated. The author of a *Feature Article* will be asked to provide a clear, concise and critical status report of the field as an introduction to the article. *Review Articles* on active and rapidly changing Physics research fields will also be published. Authors of *Review Articles* are encouraged to submit two-page proposals to the Editor-in-Chief for approval. Manuscripts submitted in *Arabic* should be accompanied by an Abstract and Keywords in English.

Organization of the Manuscript

Manuscripts should be typed double spaced on one side of A4 sheets (21.6 x 27.9 cm) with 3.71 cm margins, using Microsoft Word 2000 or a later version thereof. The author should adhere to the following order of presentation: Article Title, Author(s), Full Address and E-mail, Abstract, PACS and Keywords, Main Text, Acknowledgment. Only the first letters of words in the Title, Headings and Subheadings are capitalized. Headings should be in **bold** while subheadings in *italic* fonts.

Title Page: Includes the title of the article, authors' first names, middle initials and surnames and affiliations. The affiliation should comprise the department, institution (university or company), city, zip code and state and should be typed as a footnote to the author's name. The name and complete mailing address, telephone and fax numbers, and e-mail address of the author responsible for correspondence (designated with an asterisk) should also be included for official use. The title should be carefully, concisely and clearly constructed to highlight the emphasis and content of the manuscript, which is very important for information retrieval.

Abstract: A one paragraph abstract not exceeding 200 words is required, which should be arranged to highlight the purpose, methods used, results and major findings.

Keywords: A list of 4-6 keywords, which expresses the precise content of the manuscript for indexing purposes, should follow the abstract.

PACS: Authors should supply one or more relevant PACS-2006 classification codes, (available at <http://www.aip.org/pacs/pacs06/pacs06-toc.html>)

Introduction: Should present the purpose of the submitted work and its relationship to earlier work in the field, but it should not be an extensive review of the literature (e.g., should not exceed 1 ½ typed pages).

Experimental Methods: Should be sufficiently informative to allow competent reproduction of the experimental procedures presented; yet concise enough not to be repetitive of earlier published procedures.

Results: should present the results clearly and concisely.

Discussion: Should be concise and focus on the interpretation of the results.

Conclusion: Should be a brief account of the major findings of the study not exceeding one typed page.

Acknowledgments: Including those for grant and financial support if any, should be typed in one paragraph directly preceding the References.

References: References should be typed double spaced and numbered sequentially in the order in which they are cited in the text. References should be cited in the text by the appropriate Arabic numerals, enclosed in square brackets. Titles of journals are abbreviated according to list of scientific periodicals. The style and punctuation should conform to the following examples:

1. Journal Article:

- a) Heisenberg, W., *Z. Phys.* 49 (1928) 619.
- b) Bednorz, J. G. and Müller, K. A., *Z. Phys.* B64 (1986) 189
- c) Bardeen, J., Cooper, L.N. and Schrieffer, J. R., *Phys. Rev.* 106 (1957) 162.
- d) Asad, J. H., Hijjawi, R. S., Sakaji, A. and Khalifeh, J. M., *Int. J. Theor. Phys.* 44(4) (2005), 3977.

2. Books with Authors, but no Editors:

- a) Kittel, C., "Introduction to Solid State Physics", 8th Ed. (John Wiley and Sons, New York, 2005), chapter 16.
- b) Chikazumi, S., C. D. Graham, JR, "Physics of Ferromagnetism", 2nd Ed. (Oxford University Press, Oxford, 1997).

3. Books with Authors and Editors:

- a) Allen, P. B. "Dynamical Properties of Solids", Ed. (1), G. K. Horton and A. A. Maradudin (North-Holland, Amsterdam, 1980), p137.
- b) Chantrell, R. W. and O'Grady, K., "Magnetic Properties of Fine Particles" Eds. J. L. Dormann and D. Fiorani (North-Holland, Amsterdam, 1992), p103.

4. Technical Report:

Purcell, J. "The Superconducting Magnet System for the 12-Foot Bubble Chamber", report ANL/HEP6813, Argonne Natl. Lab., Argonne, III, (1968).

5. Patent:

Bigham, C. B., Schneider, H. R., US patent 3 925 676 (1975).

6. Thesis:

Mahmood, S. H., Ph.D. Thesis, Michigan State University, (1986), USA (Unpublished).

7. Conference or Symposium Proceedings:

Blandin, A. and Lederer, P. *Proc. Intern. Conf. on Magnetism, Nottingham* (1964), P.71.

8. Internet Source:

Should include authors' names (if any), title, internet website, URL, and date of access.

9. Prepublication online articles (already accepted for publication):

Should include authors' names (if any), title of digital database, database website, URL, and date of access.

For other types of referenced works, provide sufficient information to enable readers to access them.

Tables: Tables should be numbered with Arabic numerals and referred to by number in the Text (e.g., Table 1). Each table should be typed on a separate page with the legend above the table, while explanatory footnotes, which are indicated by superscript lowercase letters, should be typed below the table.

Illustrations: Figures, drawings, diagrams, charts and photographs are to be numbered in a consecutive series of Arabic numerals in the order in which they are cited in the text. Computer-generated illustrations and good-quality digital photographic prints are accepted. They should be black and white originals (not photocopies) provided on separate pages and identified with their corresponding numbers. Actual size graphics should be provided, which need no further manipulation, with lettering (Arial or Helvetica) not smaller than 8 points, lines no thinner than 0.5 point, and each of uniform density. All colors should be removed from graphics except for those graphics to be considered for publication in color. If graphics are to be submitted digitally, they should conform to the following minimum resolution requirements: 1200 dpi for black and white line art, 600 dpi for grayscale art, and 300 dpi for color art. All graphic files must be saved as TIFF images, and all illustrations must be submitted in the actual size at which they should appear in the journal. Note that good quality hardcopy original illustrations are required for both online and mail submissions of manuscripts.

Text Footnotes: The use of text footnotes is to be avoided. When their use is absolutely necessary, they should be typed at the bottom of the page to which they refer, and should be cited in the text by a superscript asterisk or multiples thereof. Place a line above the footnote, so that it is set off from the text.

Supplementary Material: Authors are encouraged to provide all supplementary materials that may facilitate the review process, including any detailed mathematical derivations that may not appear in whole in the manuscript.

Revised Manuscript and Computer Disks

Following the acceptance of a manuscript for publication and the incorporation of all required revisions, authors should submit an original and one more copy of the final disk containing the complete manuscript typed double spaced in Microsoft Word for Windows 2000 or a later version thereof. All graphic files must be saved as PDF, JPG, or TIFF images.

Allen, P.B., “.....”, in: Horton, G.K., and Muradudin, A. A., (eds.), “Dynamical.....”, (North.....), pp....

Reprints

Twenty (20) reprints free of charge are provided to the corresponding author. For orders of more reprints, a reprint order form and prices will be sent with the article proofs, which should be returned directly to the Editor for processing.

Copyright

Submission is an admission by the authors that the manuscript has neither been previously published nor is being considered for publication elsewhere. A statement transferring copyright from the authors to Yarmouk University is required before the manuscript can be accepted for publication. The necessary form for such transfer is supplied by the Editor-in-Chief. Reproduction of any part of the contents of a published work is forbidden without a written permission by the Editor-in-Chief.

Disclaimer

Opinions expressed in this Journal are those of the authors and neither necessarily reflects the opinions of the Editorial Board or the University, nor the policy of the Higher Scientific Research Committee or the Ministry of Higher Education and Scientific Research. The publisher shoulders no responsibility or liability whatsoever for the use or misuse of the information published by JJP.

Indexing

JJP is currently applying for indexing and abstracting to all related International Services.

Jordan Journal of
P H Y S I C S

An International Peer-Reviewed Research Journal

Volume 2, No. 2, 2009, 1430 H

Table of Contents:

Review Article	Pages
Reactor Pressure Vessel Steel Degradation Studied by Mössbauer and Positron Annihilation Spectroscopy Jozef Lipka	73-88
English Articles	Pages
Measurement of Radon -222 Concentration Levels in Spring Water in Iraq R. M. Yousuf, M. M. Husain and L. A. Najam	89-93
Preparation of Nanocrystalline $BaFe_{12-2x}Co_xTi_xO_{19}$ by Ball Milling Method and their Magnetic Properties Ibrahim Bsoul	95-102
Monitoring the Development of Cotton (<i>Gossypium barbadense</i> L.) using Emission Spectra of Chlorophyll Fluorescence S. T. Kafi, I. M. K. Medani, A. M. Ahmed and A. K. Sabir Ali	103-111
Multistream Instability in Two and Three-Species Plasmas M. S. Bawa'aneh, G. Assayed, M. Shatnawi, G. Alna'washi and S. Al-Awfi	113-123
Arabic Article	Pages
The Effect of the Emission Angle of the Light on Its Bending تأثير زاوية انبعاث الضوء في زاوية انحنائه M. A. AL-Obayde and S. E. Khaleel	125-130

Jordan Journal of Physics

REVIEW ARTICLE

Reactor Pressure Vessel Steel Degradation Studied by Mössbauer and Positron Annihilation Spectroscopy

Jozef Lipka

Department of Nuclear Physics and Technology, Slovak University of Technology, Ilkovičova 3, 81219 Bratislava, Slovakia. And Slovak Institute of Metrology, Bratislava, Slovakia.

Received on: 21/5/2009; Accepted on: 28/7/2009

Abstract: The work applies Mössbauer spectroscopy (MS) and positron annihilation spectroscopy (PAS) to evaluate the microstructure parameters of materials. These methods are used for collecting additional characteristics for understanding the degradation processes in reactor pressure vessel steels. Samples from the Russian 15Kh2MFA and Sv10KhMFT steels, commercially used at WWER-440 nuclear reactors, were irradiated near the core at NPP Bohunice (Slovakia) to neutron fluences in the range $7.8 \times 10^{23} \text{ m}^{-2}$ to $2.5 \times 10^{24} \text{ m}^{-2}$. Systematic changes in the MS and PAS spectra were observed mainly during the early period of irradiation. These could be due to changes caused by precipitation of elements like Cu, P or Cr, mainly in carbides, on the surface. The MS results confirm that the close environment of Fe atoms in the b.c.c. lattice of RPV steels remains almost stable after initial changes and can be correlated with the ductile-brittle transition temperature curve from mechanical tests. Positron annihilation lifetime measurements using the Pulsed Low Energy Positron System (PLEPS) were applied for investigation of defects of irradiated and thermally treated reactor pressure vessel (RPV) steels. PLEPS results showed that the changes in the microstructure of the RPV-steel properties caused by neutron irradiation and post-irradiation thermal treatment can be detected in the surface as well as the bulk region.

Keywords: Reactor pressure vessel steels; Mössbauer spectroscopy; Positron annihilation; Neutron irradiation, Neutron embrittlement.

PACS: 81.70.-q, 61.80.Hg, 78.70.Bj

1. Introduction

The degree of embrittlement in a reactor pressure vessel (RPV) is a complex function of different parameters such as temperature, neutron fluence, flux and material chemistry, ect. [1-9]. Many results on embrittlement mechanisms have been obtained on a macroscopic scale and with well proven macroscopic techniques. However, prediction and modeling of the property changes would benefit from knowledge of the evolution of the irradiation-produced microstructure. Therefore, for a good microscopic understanding of the damage caused by

radiation, microstructural investigation techniques need to be applied. In order to gain better understanding of the microscopic mechanisms of irradiation embrittlement, Mössbauer and positron annihilation spectra have been collected for a number of selected steel samples within a Slovak extended surveillance specimen program. As-received, thermally treated as well as irradiated conditions have been considered.

Many additional test methods, summarised in Ref.[10] have been developed to unravel the complex microscopic

mechanisms responsible for RPV steel embrittlement. According to our experimental possibilities and practical experiences, the Mössbauer spectroscopy (MS) results were compared mostly with positron annihilation spectroscopy (PAS) [11-26] and transmission electron microscopy (TEM) [18, 20, 24, 27, 28].

2. Application of Mössbauer Spectroscopy to RPV-steel Investigation

Mössbauer spectroscopy (MS) is a powerful analytical technique because of its speciality for one atomic species and because of its extremely high sensitivity to changes in the atomic configuration in the near vicinity of the probe isotopes (in this case ^{57}Fe). MS measures hyperfine interactions and these provide valuable and often unique information about the magnetic and electronic state of the iron species, their chemical bonding to co-ordinating ligands, the local crystal symmetry at the iron sites, structural defects, lattice-dynamical properties, elastic stresses, etc. [30, 31]. In general, a Mössbauer spectrum shows different components if the probe atoms are located at lattice positions, which are not chemically equivalent. From the parameters that characterise a particular Mössbauer sub-spectrum it can, for instance, be established whether the corresponding probe atoms reside in sites which are not affected by structural lattice defects, or whether they are located at defect-correlated positions. In this respect, however, it is imperative to combine Mössbauer measurements with other research methods, which preferably are sensitive to the nature of the defect properties. Combining the results of MS and other techniques [32] on the same samples seems to be a promising approach for such study.

Differences between Mössbauer spectra obtained from different Eastern as well as Western types of RPV steels were already discussed in detail [33, 34]. Only few studies, indicating MS to be a potentially interesting tool to investigate the microstructural aspects of irradiation embrittlement of RPV steels, have been performed so far [29, 31, 33, 34]. The results showed that the distribution analysis of the spectra makes it possible to

distinguish between the different steel types. Small differences in carbon concentrations between Western base and weld metal are reflected in the small area fraction of the cementite doublet for the weld metal. Differences between Eastern and Western type RPV steels are reflected in the overall shape of the derived H_{hf} -distribution profile. The larger fraction of the 'perturbed' area for the Eastern steel, the differences in H_{hf} and δ values and the absence of a carbide doublet sub-spectrum are all due to the fact that the overall alloy-element concentration (especially for Cr and V) for the Eastern steels is larger than for Western-type steels. This interpretation was supported also by results from transmission electron microscopy and positron-annihilation measurements [24, 27]. Vanadium carbides (V_xC_y) formation was confirmed also using small angle neutron scattering (SANS) [35, 36]. According to latest knowledge, V is known as a predominant element to enhance the tensile properties of material.

3. Application of the PAS Techniques

Since 1985, positron annihilation spectroscopy (PAS) has been repeatedly used in the study of RPV steels [5, 11-26]. The positron lifetime (PL) technique is a well-established method for studying open-volume type atomic defects and defect-impurity interactions in metals and alloys. The lifetime of positrons trapped at radiation-induced vacancies, vacancy-impurity pairs, dislocations, microvoids, etc. is longer than that of free positrons in the perfect region of the same material. As a result of the presence of open-volume defects, the average positron lifetime observed in structural materials is found to increase with radiation damage [15, 19].

According to previous work it seems to be generally accepted that in RPV steels (containing more than 0.1 wt. % of copper), the copper and phosphorus rich precipitates play a dominant role in thermal and radiation embrittlement [2, 4, 37-39]. In case of Russian-type RPV steels, the formation of carbides has been proposed as an additional micro-structural mechanism derived from comprehensive PAS [11] and transmission

electron microscopy (TEM) studies [27, 28]. Therefore, the main purpose of the present investigation was to look for differences between non-irradiated, annealed, irradiated and post-irradiation thermally treated WWER-440 base and weld RPV materials by means of the unique pulsed low energy positron system (PLEPS).

For the interpretation of results from PL measurements, the standard trapping model (STM) can be used [40], if the sample is homogenous. This premise, however, does not hold for RPV-steels completely. In inhomogeneous samples, the diffusion of positrons from the various implantation sites to the trapping centres has also to be considered [41, 42]. However, the mathematical difficulties associated with the corresponding diffusion-trapping model (DTM) [43], have so far prevented exact solutions in all but the simplest cases [44, 45]. Thus it was impossible to analyse quantitatively the very detailed experimental results obtained with the pulsed positron beam. The application of improved DTM combined with the pulsed positron beam technique is described in detail in [46].

For the first time the pulsed low-energy positron system (PLEPS) [47, 48] was used for the investigation of neutron-irradiated RPV-steels. This system enables the study of the microstructural changes in the region from 20 to 550 nm (depth profiling) with small and very thin ($< 50 \mu\text{m}$) specimens, therefore reducing the disturbing ^{60}Co radiation contribution to the lifetime spectra to a minimum [26]. Such a disturbance is the limiting factor for the investigation of highly irradiated RPV specimens with conventional positron lifetime systems.

Several approaches to tackle the problem of the ^{60}Co prompt-peak interference with the physical part of the positron lifetime spectra have been considered so far [11, 21, 49, 50]. Besides the PLEPS technique, one of the other acceptable solutions seems to be a triple-coincidence method using a ^{22}Na -source [21]. In this case three γ -rays – one with energy of 1274 keV and two with 511 keV – accompany each event of positron annihilation, while only two γ -rays result from the ^{60}Co decay. However, compared to conventional two-detector systems, the

requirement of the triple coincidence reduces drastically the rate of accumulation of positron lifetime spectra [19, 21] and in comparison, PLEPS reduces the measuring time by a factor of 500 and enables in addition the estimation of the defect concentration.

The time resolution of PLEPS was about 240 ps FWHM. All lifetime spectra of irradiated RPV specimens contained about 3×10^7 events at a peak to background ratio in the range between 30:1 and 100:1 [26].

4. Specimens and irradiation conditions

In the Extended Surveillance Specimen Program (ESSP) 24 specimens, designed especially for MS measurement, were selected and measured in the "as received" state, before their placement into the core of the operated nuclear reactor [25, 51]. The ESSP and specimen preparation are presented in detail in part I of this complex paper. For this program and measurement of high-irradiated RPV-specimens the one-dimensional angular correlation positron-annihilation spectrometer was developed at the Department of Nuclear Physics and Technology of Slovak University of Technology in Bratislava [52]. Results from this measurement are reported in detail in [53]. Beside this, the positron annihilation lifetime spectra were measured using a pulsed low energy positron system at the University of Bundeswehr in Munich (Germany). Both techniques were upgraded for measurement of irradiated specimens, where disturbing ^{60}Co contribution was a limiting factor for measurement in the past. The positron annihilation results were reported in preliminary form [26].

Room temperature Mössbauer spectroscopy measurements were carried out in transmission geometry on a standard constant acceleration spectrometer with a ^{57}Co source in Rh matrix [29]. The absorbers consisted of 25-40 μm thick foils. Due to higher neutron embrittlement and ageing sensitivity of WWER 440 (V-230) nuclear reactors, our study has been focused on the Russian 15Kh2MFA steel used in this older WWER-440 reactor type.

Specimens were measured before their placement into the irradiation chambers, near the core of the operated nuclear reactor, and after 1, 2 and 3 years stay there (neutron fluency in the range $7.8 \times 10^{23} \text{ m}^{-2}$ up to $2.5 \times 10^{24} \text{ m}^{-2}$). Taking into account the enhancement of the irradiation due to the closer position of the irradiation chambers to

the reactor core (“accelerating” factor of about 10 at the most loaded position), the radiation treatment of the specimens after 3 years is equivalent to about 30 years of real RPV-steel (projected lifetime of RPV). The chemical composition and the irradiation conditions of the studied RPV-steel specimens are shown in Table 1 and Table 2.

TABLE 1. The chemical composition of the RPV-steel specimens [14]. The possible nitrogen concentration is not given in the steel certificate. Nevertheless, we assume its presence approximately at the level of carbon.

	Chemical composition in wt. %											
	C	Si	Mn	S	P	Cr	Ni	Mo	V	As	Co	Cu
BM	0.13-0.18	0.17-0.37	0.30-0.60	max. 0.025	max. 0.025	2.50-3.00	max. 0.40	0.60-0.80	0.25-0.35	max. 0.050	max. 0.020	max. 0.150
Unit 3	0.14	0.22	0.49	0.016	0.013	2.81	0.065	0.615	0.335	0.007	0.009	0.072
Unit 4	0.15	0.24	0.41	0.015	0.015	2.86	0.085	0.7	0.322	0.007	0.007	0.075
WM	0.03-0.12	0.20-0.65	0.55-1.30	max. 0.030	max. 0.030	1.10-1.60	-	0.40-0.60	0.15-0.30	max. 0.050	max. 0.025	max. 0.120
Unit 3	0.042	0.64	1.22	0.015	0.013	1.32	-	0.44	0.24	-	0.003	0.10
Unit 4	0.031	0.60	1.13	0.015	0.010	1.31	-	0.52	0.19	-	0.006	0.06

TABLE 2. Description of the specimens irradiated at the 3rd unit of NPP Bohunice (Slovakia) during 1995-1998.

Sample	Material	Time of irradiation (eff. days)	Neutron Fluence ($E_n > 0.5 \text{ MeV}$) (m^{-2})	Total activity (kBq)	Thickness of sample (μm)
ZMNF	Base metal non-irradiated	0	0	0	60
ZM1Y	Base metal 1 year irradiated	280	7.81E23	62	50
ZM2Y	Base metal 2 year irradiated	578	1.64E24	109	40
ZM3Y	Base metal 3 year irradiated	894	2.54E24	89	30
ZMNA	Sample ZMNF annealed 1 hour in vacuum at 385°C	0	0	0	60
ZKNF	Weld non-irradiated	0	0	0	55
ZK1Y	Weld 1 year irradiated	280	7.81E23	30	45
ZK2Y	Weld 2 years irradiated	578	1.64E24	48	25
ZK3Y	Weld 3 years irradiated	894	2.54E24	110	47
ZKNA	Sample ZKNF annealed 1 hour in vacuum at 385°C	0	0	0	60

The temperature during the irradiation was measured, using melting monitors (special materials with well-defined melting temperature) placed inside special containers,

and reached values in the region of 285-298 °C. Neutron monitors measured the level of the neutron fluence.

5. Results

5.1. MS Results

Mössbauer spectra, which correspond to the basic and weld material samples, show typical behaviour of dilute iron alloys and can be described with three [23] or four sextets (this work). The reference MS spectra were compared with the irradiated state of identical specimens. These specimens were placed into operated nuclear reactor in the NPP Bohunice

unit-3 and unit-4 with the aim to perform identical thermal and radiation treatment of RPV surveillance specimens as exists in reality.

The total specific activity of the first batch of specimens (sample k716 BM-I with the weight of 25.6 mg) was 3.2×10^7 Bq/g. It is mostly due to presence of ^{60}Co and ^{54}Mn as presented in Table 3 and Fig. 1.

TABLE 3. Activities of the most detected nuclides in RPV-steel specimen k716 BM-I (25.6 mg).

Nuclide	Sb 124	Co 58	Co 60	Cr 51	Fe 59	J 131	Mn 54	Na 24
Activity [Bq]	6438	1673	160750	22622	47952	37660	544790	143
Error	$\pm 1 \times 10^2$	$\pm 1 \times 10^2$	$\pm 2 \times 10^2$	$\pm 3 \times 10^2$	$\pm 2 \times 10^2$	$\pm 2 \times 10^3$	$\pm 3 \times 10^2$	$\pm 1 \times 10^2$

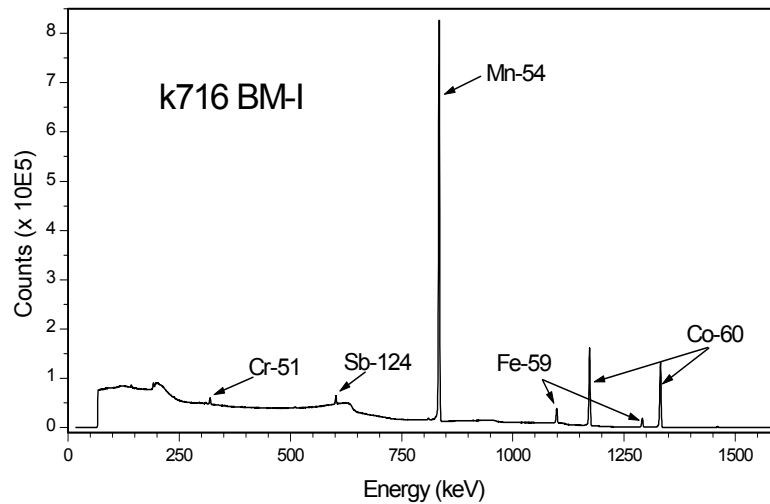


FIG. 1. Gamma spectroscopy spectrum of irradiated RPV-steel specimen 15Kh2MFA (k716-MB-I).

As the most suitable fitting model we used the four components fit with fixed sextet No.2, which corresponds to the pure α -iron with hyperfine field $H_{hf,2} = 33.0$ T. MS parameters as areas under sextets (A_x) and hyperfine fields ($H_{hf,x}$) of RPV-steel specimens are selected in Tables 4 and 5. Typical Mössbauer spectra of base metal of RPV specimens after 1-year stay in operated nuclear reactor, treated by the neutron fluency $\Phi(E_n > 0.5 \text{ MeV}) = 7.8 \times 10^{23} \text{ m}^{-2}$ are shown in Fig. 2. No doublet component (according to [23] typical for western RPV-steels, assigned to cementite contribution) was identified in spectra. This is most probably due to vanadium presence leading to VC formation in Russian steels.

The most significant change after neutron irradiation is observable in areas under first two components (see Tables 4 and 5). The degradation mechanism of RPV-steel specimens owing to fast neutron bombardment is shown as a decrease of the pure α -iron component presence (fixed in all analysis at $H_{hf,2} = 33.0$ T). The significant decrease (up to 10%) was observed in all specimens. This decrease was balanced by the increased $H_{hf,1}$ values of the first component, which can be assigned to the contribution of a complex of atoms (Cr, Ni, Cu, Mn, ...). Comparison of results from both units and between the base and weld material is shown in Fig. 3A–3D.

There were clear differences between base and weld materials, but the behaviour of MS parameters due to irradiation are similar. After relatively intensive jumps of values after the first year of irradiation, these

changes do not continue due to increased irradiation treatment and stay almost stable (base metals) or move slightly back (welds). It seems that after the first year of irradiation the effects come to saturation.

TABLE 4. Comparison of RPV-steel specimens in non-irradiated and irradiated state at 3rd unit NPP Bohunice (abbreviations BM-N stand for: base material - not irradiated, BM-I base material – irradiated – numbers of years, WM-N weld material - not irradiated, WM-I weld material – irradiated – numbers of years).

Specimen	A_1 [%]	A_2 [%]	ΔA_{1+} [%]	ΔA_{2-} [%]	A_3 [%]	A_4 [%]	H_{hf1} [T]	H_{hf2} [T]	H_{hf3} [T]	H_{hf4} [T]
k716 BM-N \equiv ZMNF	24.3	35.0			33.3	7.4	33.8	33.0	30.6	28.5
k716 BM-I-1y \equiv ZM1Y	31.6	25.1	7.3	9.9	37.3	6.0	33.7	33.0	30.7	28.6
k723 WM-N \equiv ZKNF	17.2	41.9			34.1	6.8	33.8	33.0	30.6	28.5
k723 WM-I-1y \equiv ZK1Y	23.8	34.0	6.6	7.9	35.3	6.9	33.7	33.0	30.6	28.4
2 years										
k721 BM-N	27.1	30.7			35.2	6.9	33.8	33.0	30.6	28.3
k721 BM-I-2y \equiv ZM2Y	31.1	25.4	4.0	5.3	36.9	6.6	33.7	33.0	30.6	28.1
k725 WM-N	20.5	41.4			30.8	7.3	33.8	33.0	30.7	28.6
k725 WM-I-2y \equiv ZK2Y	21.6	40.7	1.1	0.7	29.6	8.1	33.6	33.0	30.6	28.5
3 years										
k720 BM-N	26.2	32.5			33.7	7.6	33.8	33.0	30.7	28.6
K720 BM-I-3y \equiv ZM3Y	33.4	25.4	7.2	7.1	35.2	6.0	33.7	33.0	30.6	28.1
k728 WM-N	16.5	42.4			35.4	5.7	33.8	33.0	30.6	28.3
k728 WM-I-3y \equiv ZK3Y	19.0	40.1	2.5	2.3	34.6	6.3	33.7	33.0	30.6	28.1
Accuracy	± 0.8	± 0.8	± 0.8	± 0.8	± 0.8	± 0.8	± 0.1	± 0.0	± 0.1	± 0.2

TABLE 5. Comparison of RPV-steel specimens in irradiated and non-irradiated state at 4th unit NPP Bohunice.

Specimen	A_1 [%]	A_2 [%]	ΔA_{1+} [%]	ΔA_{2-} [%]	A_3 [%]	A_4 [%]	H_{hf1} [T]	H_{hf2} [T]	H_{hf3} [T]	H_{hf4} [T]
k731 BM-N	24.6	33.3			35.4	6.7	33.8	33.0	30.6	28.3
k731 BM-I-1y	28.4	28.0	3.8	5.3	36.0	7.6	33.7	33.0	30.6	28.2
k735 WM-N	18.1	44.0			31.1	6.8	33.7	33.0	30.6	28.7
k735 WM-I-1y	23.0	38.2	4.9	5.8	32.7	6.1	33.7	33.0	30.6	28.4
2 years										
k733 BM-N	27.1	33.0			34.0	5.9	33.8	33.0	30.6	28.3
k733 BM-I-2y	31.7	27.6	4.6	5.4	34.3	6.4	33.7	33.0	30.6	28.2
k739 WM-N	17.2	46.1			29.1	7.7	33.8	33.0	30.7	28.9
k739 WM-I-2y	20.4	43.0	3.2	3.1	30.2	6.3	33.6	33.0	30.6	28.4
3 years										
k734 BM-N	26.1	36.8			31.5	5.7	33.8	33.0	30.6	28.4
k734 BM-I-3y	31.1	29.7	5.0	7.1	32.2	7.0	33.7	33.0	30.6	28.4
k740 WM-N	17.8	44.9			32.1	5.2	33.8	33.0	30.6	28.6
k740 WM-N-3y	20.5	42.5	2.7	2.4	31.7	5.3	33.7	33.0	30.6	28.1
Accuracy	± 0.8	± 0.8	± 0.8	± 0.8	± 0.8	± 0.8	± 0.1	± 0.0	± 0.1	± 0.2

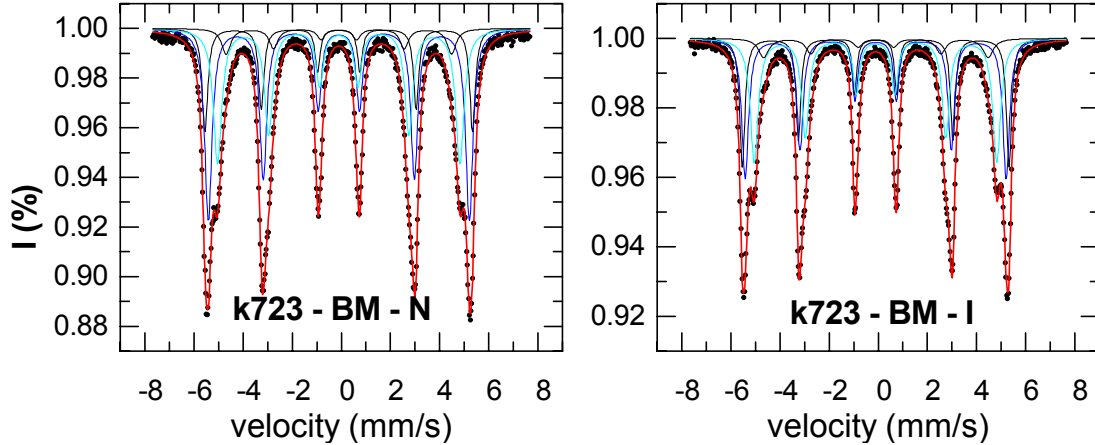


FIG. 2. Comparison of Mössbauer spectra of RPV- base material in non-irradiated and irradiated state.

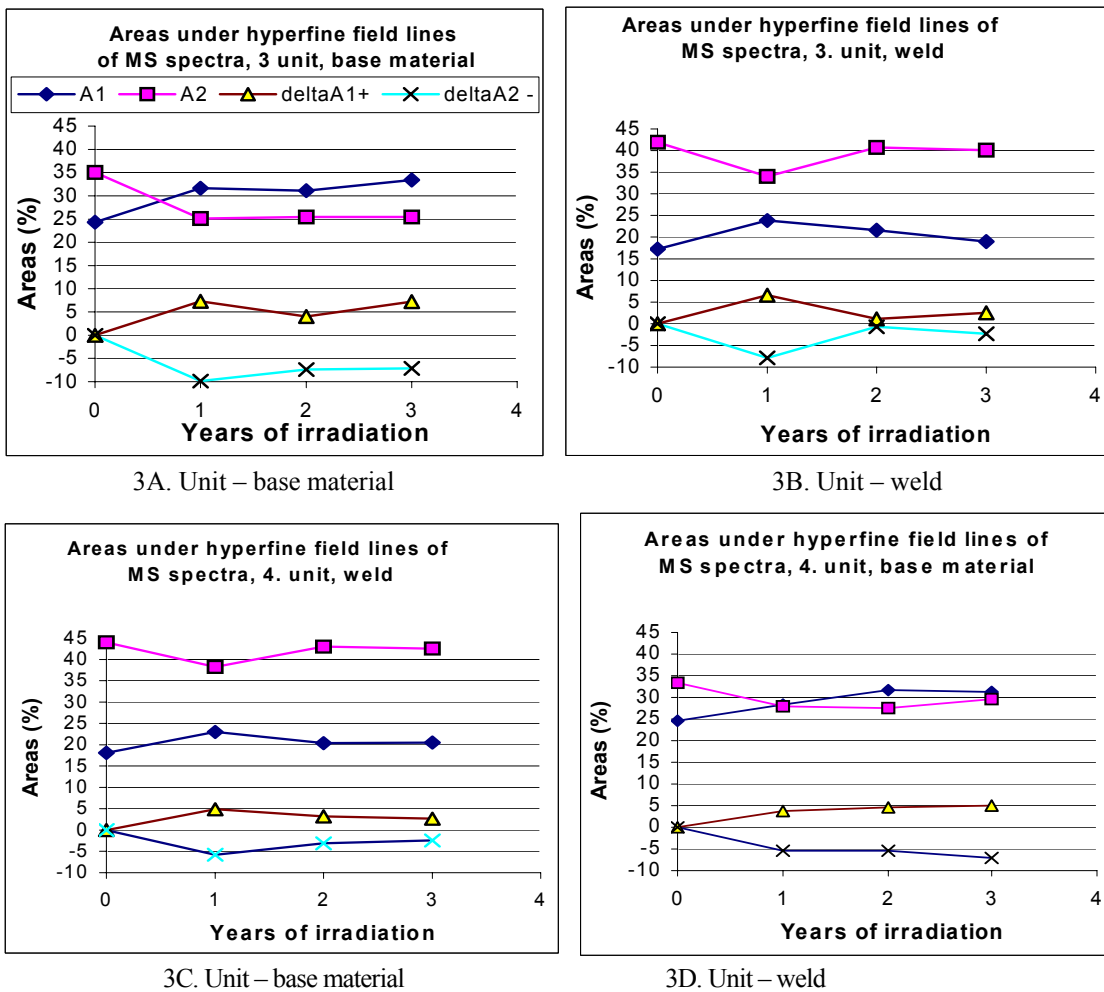


FIG. 3(A-D). Changes in areas under hyperfine field lines of first two sextets of Mössbauer spectra measured on original irradiated RPV-steels from NPP Bohunice (Slovakia) in frame of extended surveillance specimen program. Delta A1+ and delta A2- present increase of first and decrease of second component, respectively.

5.2. PAS Results

According to our previous work and experiences [13, 23-25] a suitable set of RPV steel specimens was selected and prepared for

the investigation. In the framework of the “Extended Surveillance Specimen Program” [25, 51], several specimens, prepared originally for Mössbauer spectroscopy

measurements [54], and suitable for PLEPS measurement because of their size ($10 \times 10 \times 0.05$ mm) and polished surfaces, were selected and measured before and after their irradiation, near the core of the nuclear reactor. The chemical composition and the irradiation conditions of the studied RPV-steel specimens are shown in Table 1 and Table 2. Specimens measured by MS and PAS techniques were identical.

The calculated positron lifetimes for different types of defects in pure iron and different carbides in low alloy Cr-Mo-V steel

are shown in Table 6. Experimental results for the mean positron lifetime τ_m after various irradiation treatments are shown in Fig. 4 and Fig. 5. τ_m is plotted versus the mean positron implantation depth. The characteristic decrease of τ_m with increasing positron implantation depth is typical for measurements with a low energy pulsed positron beam. It is due to the back diffusion of positrons to the surface and subsequent trapping at a surface state or in the oxide layer.

TABLE 6. Calculated positron lifetimes for different types of defects in pure iron and different carbides in low alloy Cr-Mo-V steel.

Material	Positron lifetime (ps)	Reference
Fe-bulk	110	[59]
Fe-dislocations	165	[60]
Fe-monovacancy	175	[59]
Fe-divacancy	197	[60]
Fe-3 vacancy cluster	232	[60]
Fe-4 vacancy cluster	262	[60]
Fe-6 vacancy cluster	304	[60]
VC	99	[61]
$V_{0.86}Cr_{0.09}Mo_{0.04}Fe_{0.01}C$	105	[61]
Mo_2C	112	[61]
$Mo_{1.4}Cr_{0.6}C$	116	[61]
Cr_7C_3	107	[61]
$Cr_{23}C_6$	112	[61]
$Mn_{26}C_6$	99	[61]
Fe_3C	101	[61]

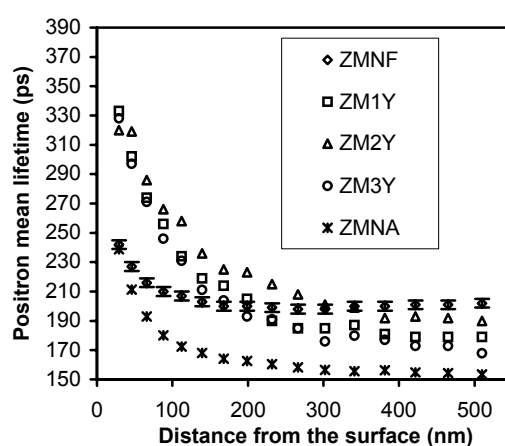


FIG. 4. Comparison of mean lifetimes τ_m of different neutron-irradiated 15Kh2MFA (base metal) steel specimens.

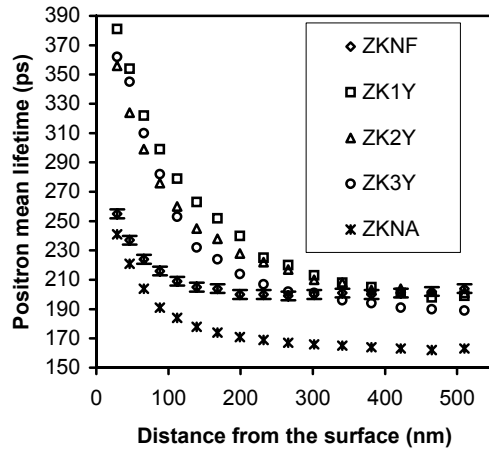


FIG. 5. Comparison of mean lifetimes τ_m of different neutron-irradiated Sv10KhMFT (weld) steel specimens.

Each lifetime spectrum can be well analysed by two lifetime components, which below a depth of about 300 nm remain fairly constant over the full depth range (see Fig. 6 and Fig. 7). The shorter lifetime τ_1 of about 170 ps is the dominant steel component (most likely iron monovacancies or dislocation lines) with an intensity of about 97% in the bulk. The longer lifetime τ_2 with intensity of about 3% or less and a value of about 400-500 ps can be assigned to the contribution of

large vacancy clusters. The intensity of this component is surprisingly much higher (up to 10-12 %) for those specimens, which were not thermally treated (reference specimens ZMNF and ZKNF), indicating that large vacancy clusters are already present in the material before irradiation. These ZMNF and ZKNF specimens were annealed for 1 hour in vacuum at 385 °C and renamed ZMNA and ZKNA (see Table 2 and Figs. 6, 7).

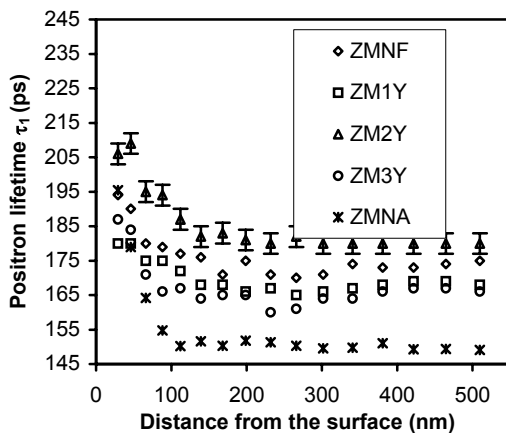


FIG. 6. Comparison of lifetimes τ_1 of RPV steel specimens (base metal) after different neutron irradiation.

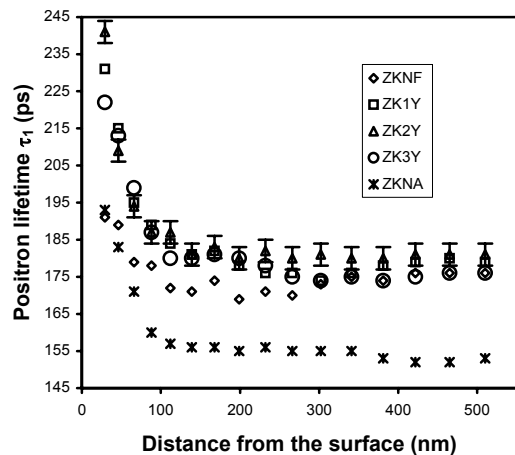


FIG. 7. Comparison of lifetimes τ_1 of RPV steel specimens (weld) after different neutron irradiation.

The interesting results for the irradiated specimens, in respect to the defect structure in the bulk, presented in Fig. 6 and Fig. 7, are the almost constant value of τ_1 for the weld alloy as well as the oscillating behaviour of τ_1 for the base alloy, where the resulting lifetime indicate that after one year and three years irradiation obviously only dislocations are present, whereas after two years of neutron irradiation a mixture of iron mono- and di-vacancies is produced. However, in both base and weld alloys, the concentration of large vacancy clusters is reduced from about 12 percent before irradiation to 3 percent after irradiation. It is very likely that in addition, small irradiation - induced precipitates (probably carbides) with sizes of about 1 to 2 nm [36] developed, which are not so effective for trapping positrons.

Decrease of the mean positron lifetime τ_m after annealing of the non-irradiated specimens (ZMNF and ZKNF) in vacuum at 385 °C for 1 hour was from 200 ± 3 ps to 161 ± 3 ps in the case of base metal (ZM) and from 201 ± 3 ps to 170 ± 3 ps for weld metal (ZK) (see Figs. 4-5).

Of particular interest is the concentration of defects as a function of irradiation dose and thermal treatment. Generally, this effect can be obtained from positron studies only if the bulk lifetime can be resolved from the

shortest lifetime, attributed to annihilation from defects. In the present case of saturation trapping this was impossible. Therefore, from the individual lifetime spectra we can only conclude a total trapping rate κ larger than about 10^{10}s^{-1} .

However, from the variation of the mean lifetime τ_{av} as a function of positron implantation energy, we can estimate κ even in the case of saturation trapping. The problem was fully analysed in [46, 55]. Based on this theory the total defect concentration can be estimated as:

$$c_d = \frac{\kappa}{\kappa_{spec}}$$

In Fig. 8 and Fig. 9 results for the evaluation of κ (trapping rate) as obtained by the procedure described, are presented. For the specific trapping rate κ_{spec} the plausible value $10^{15}(\text{s}^{-1})$ [40] has been assumed. Because of slight surface oxidation, this evaluation of κ results in a systematic underestimate. A lower limit of 10 ns^{-1} for κ may be derived within the framework of the STM since we have observed saturation trapping at defects.

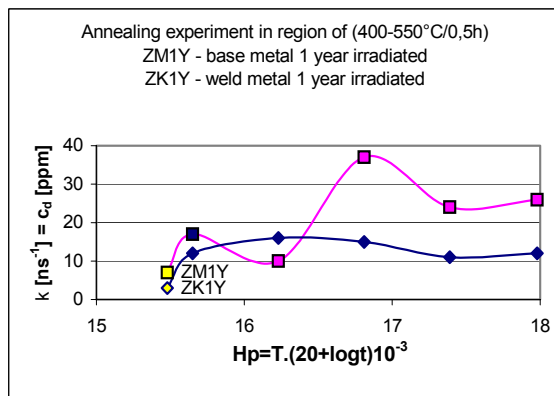


FIG. 8. The total trapping rate κ versus Hollomon-Jaffe's parameter at isochronal annealed (step 25°C) specimens of base (ZM) and weld (ZK) alloys after 1 year of irradiation in the reactor (fluency of about $7.8 \times 10^{23} \text{ m}^{-2}$). The lower limits for κ , as derived from saturation trapping according to the STM, is 10 ns^{-1} .

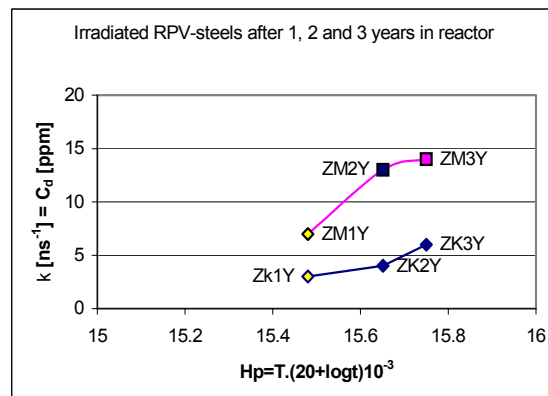


FIG. 9. The total trapping rate κ versus Hollomon-Jaffe's parameter at RPV specimens from base (ZM) and weld (ZK) alloys after 1, 2 and 3 years residence in reactor irradiation chambers (neutron fluency in the range from $7.8 \times 10^{23} \text{ m}^{-2}$ to $2.5 \times 10^{24} \text{ m}^{-2}$). The lower limits for κ , as derived from saturation trapping according to the STM, is 10 ns^{-1} .

According to the results from our measurements performed on different irradiated RPV-steels, the total trapping rate κ in ns^{-1} as well as the total defect concentration c_d (the same values but in ppm) increases slightly for both base and weld materials as a function of the irradiation dose (see Fig. 9). The weld material (Sv10KhMFT) seems to be less sensitive to the changes caused by neutron-irradiation or by post-irradiation heat treatment than the base material (15Kh2MFA) (see Fig. 8). Nevertheless, the differences in the positron trapping rate κ are not too large. It seems reasonable to relate the observed trapping rates with the ones which have been derived for trapping into precipitated carbides from electron microscopic images [20]. Accordingly, in the 15Kh2MFA the trapping rate into chromium carbides (Cr_7C_3 , Cr_{23}C_6) is predicted as $\kappa_{\text{Cr}} = 1.8 \times 10^8 \text{ s}^{-1}$ and into vanadium carbides as $\kappa_{\text{VC}} = 2.2 \times 10^{10} \text{ s}^{-1}$ [20]. Thus precipitated vanadium carbide could indeed account for the observed trapping rates. But on the other hand, as shown by calculations [35], positrons experience a repulsive potential from carbides embedded in an iron matrix. Thus only the defects at the iron-carbide interface could provide an acceptable trapping site for positrons.

The total trapping rate κ and the defect concentration c_d are stable or increase slightly for 15Kh2MFA steel as a function of Hollomon-Jaffe's parameter which determines the influence of annealing temperature $T[\text{K}]$ and time $t[\text{s}]$ together [11, 27]. Between 15.5 to 16.5 (corresponding to the temperature region 400 to 450 °C) the defect concentration increases. On the other hand (Fig. 8), in the same range, there is a marked decrease in the lifetime of defects. A simple explanation could be the dissolution of precipitates and defect clusters which would reduce the average size of the defects, and, by the same process, would increase the concentration of the defects.

The annealing effect due to the temperature of about 290 °C and due to the neutron irradiation is in competition with the creation of the new radiation-induced defects.

This finding is supported also by the results from 1D-ACAR and Mössbauer spectroscopy (MS) measurements performed on identical specimens [26, 54].

The steel specimens irradiated for one year were also isochronally annealed for 30 minutes in the temperature range of 400-550 °C in steps of 25 °C. This region was selected according to previous lifetime measurements on the same type of unirradiated material [22]. It was reasonable to start from 400 °C, because the previous isothermal treatment (one year at about 290 °C) is comparable with annealing at 400 °C for 30 minutes. The measured lifetimes of the annealed but non-irradiated specimens indicate that the small vacancy clusters are no longer present but rather a high density of dislocations remains in the sample. Via 3D presentations of PLEPS experimental results, some differences in near surface and bulk regions can be better visualized and understood. There is significant increase of the mean positron lifetime after first level of irradiation, but mostly in the surface-near region. The next long term irradiation at temperature of about 280 °C induces slight decrease of this parameter. Positron annihilation technique is highly effective for the evaluation of post irradiation heat treatment. Deep PLEPS study of WWEER base and weld metals using PLEPS on neutron fluence level of $7.8 \times 10^{23} \text{ m}^{-2}$, (specimens ZM1Y, ZK1Y). The 2 and 3D presentation of PLEPS results presenting the mean lifetime dependence on irradiation of weld is shown in Fig. 10. Similar behavior of defects creation due to increased neutron fluence was measured also for base metal (presented in other view in Fig. 11). The effectiveness of the annealing process to removing of small defects (mono/divacancies or Frenkel pairs) can be followed via significant decrease of parameter τ_1 (see Fig. 12). This figure also shows rapid increase of mentioned small defects in Russian type of RPV steels after about 500 °C.

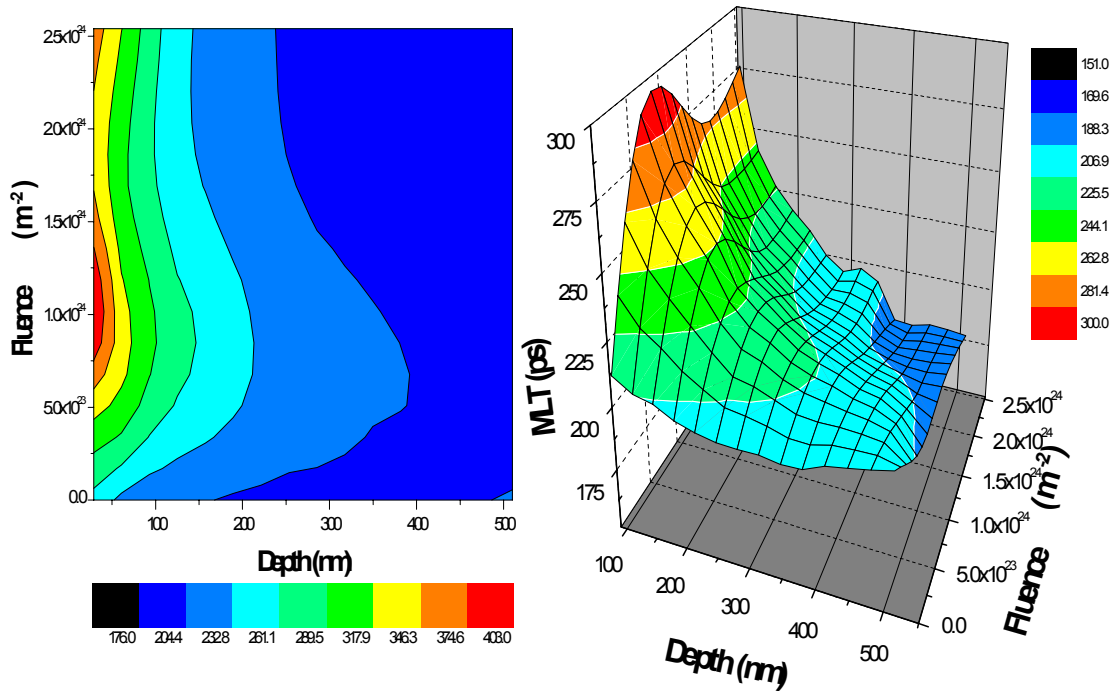


FIG. 10. The 2D and 3D presentation of PLEPS results (MLT) of irradiated Sv-10KhMFT steel (weld metal). The first D about 140 nm were neglected due to possible surface defects.

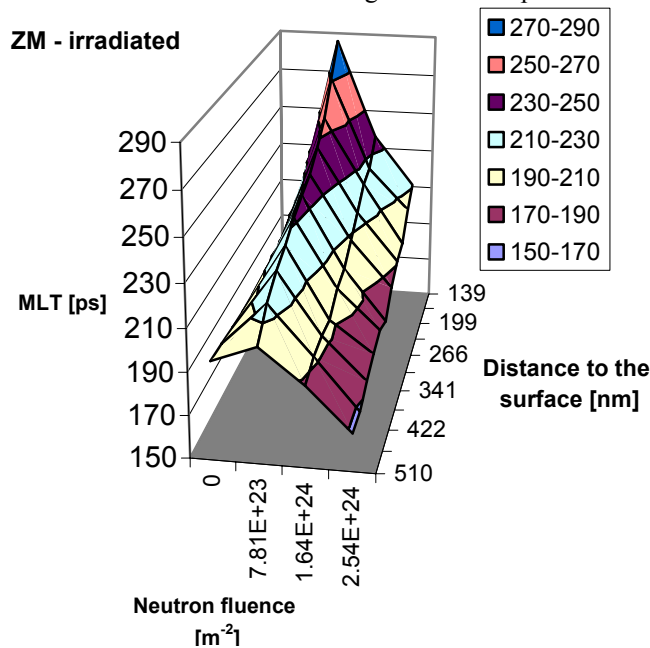


FIG. 11. The 3D presentation of PLEPS results in form of the MLT dependence on neutron fluence. The first about 140 nm were neglected due to possible surface defects.

6. Discussion and Conclusions

Conventional TEM has revealed three kinds of neutron radiation-induced matrix defects in our surveillance specimen, which consists of: black dots, small dislocation loops and fine precipitates, concentrated near dislocations and low-angle boundaries. Non irradiated microstructure of base metal is typical for annealed bainite with coarse

carbide M_3C a M_7C_3 and fine carbide MC. Weld metal microstructure is created by acicular and proeutectoid ferrite and the heat affected zone (HAZ) is created by acicular mixture martensite, self-tempered martensite and down bainite. Dislocation structure of base metal, weld metal and heat affection zone is locally markedly changed. BM dislocation structure is created by dislocation

net, but also simple dislocation configurations, which are probably anchored by MC carbide [24]. Dislocation structure is more homogeneous in WM than in BM. No micro voids were found in any surveillance specimen investigated by TEM after irradiation. The weld joint dislocation density of analyzed steel is after five-year irradiation in comparison with former exposures invariable. Dislocation substructure is evidently recovered in base metal after irradiation, the number of two-dimensional networks has increased, networks are more entire as in non-irradiation state. Locations with upper density account for specific

description of dislocations configurations too. Dislocation loops and fine precipitates density little by little decrease, relaxation, after the first year irradiation, but density increases and achieves saturation state after two, three and five years of irradiation. Their size increases and their visibility grow with increasing neutron fluence. Decoration of original dislocations with radiation-induced defects is rather general phenomenon in neutron-irradiated materials. Decoration of dislocations with a defects population probably plays a key role in irradiation induced hardening.

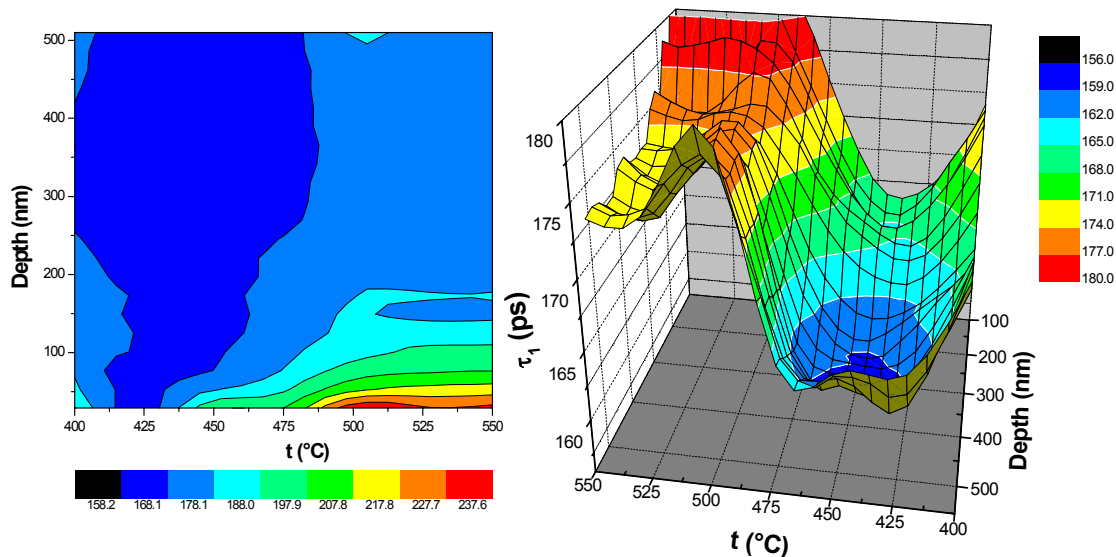


FIG. 12. The 2D and 3D presentation of PLEPS results (τ_1) of irradiated and annealed Sv-10KhMFT steel (weld metal) to level of neutron fluence $1.25 \times 10^{24} \text{ m}^{-2}$. The first about 140 nm were neglected due to possible surface defects.

Both vacancy and interstitial point defects are expected to be mobile in the temperature range of most operating pressure vessels. However, they are also expected to interact with solute atoms. The key interstitial impurity in Russian RPV steel is Carbon [11, 27]. The partial or complete trapping of self-interstitial by C solutes will cause heterogeneous cluster nucleation and a fine cluster distribution. Further, in steels containing residual levels of elements such as copper, which are in super-saturated solution, radiation-enhanced diffusion will occur at these temperatures, which leads to the formation of small clusters, which can again harden the matrix. Generally, the thermal treatment together with neutron irradiation lead to a microstructure consisting of small clusters ($< 5 \text{ nm}$ in diameter) which create

obstacles to the free movement of dislocations thereby producing an increase in the yield stress, hardness and the ductile-brittle transition temperature of the material [8, 36].

Mössbauer spectroscopy precisely identifies the close environment of Mössbauer nucleus (Fe). Although, this method is very suitable for materials containing Fe, an interpretation of results is very difficult in complex steels. Using MS, it is possible to observe changes in hyperfine fields of atoms in the lattice and according to these to evaluate the precipitation of some elements (mainly in the form of carbides [31]). Their relative areas are close to the theoretical values calculated from a random distribution model of impurities in a b.c.c. structure (5% of 12 elements in total). Results

confirmed MS sensitivity to detect also small differences in chemical composition or preparation technology of RPV steel samples. In comparison with Western types of RPV steels such as A533 C1.1 and A508 C1.3, the doublet fraction ascribed as Mn and/or Cr-substituted cementite is completely absent in 15Kh2MFA. Here probably mainly Cr₂₃C₆, Cr₇C₃ and VC carbides are formed. [34].

Significant differences in MS parameters between the RPV base and weld materials can be explained by different chemical compositions and/or different preparation technology and were observed also in the past [29, 31, 34]. The trend in the changes due to irradiation is almost the same in both materials. It seems that the expected changes in material microstructure (precipitation of elements like Cu or Cr mainly in carbides to the surface) were performed mainly during the initial period (1-year stay in irradiation containers in operating conditions by “speed factor” of about 10). These results confirm that the close environment of Fe atoms in the b.c.c. lattice of RPV steels remains after initial changes, almost stable and perhaps could be correlated with the trend of ductile-brittle transition temperature (DBTT) curve obtained from mechanical tests or with the defect density curve obtained from the transmission electron microscopy studies. With increased neutron fluence (up to $\Phi(E_n > 0.5 \text{ MeV}) = 1 \times 10^{25} \text{ m}^{-2}$) the dislocation density number as well as the average defect diameter remain stable after an initial increase of about 20-30% [28].

On the other hand, the isochronal annealing of 2 selected irradiated specimens performed at 400, 475 and 520 °C did not cause return of the MS parameters to the starting positions. It means that the radiation-induced changes observable in MS spectra were not re-annealed in such a complete way as the re-annealing of point defects observed by TEM [18, 28].

The PLEPS technique enables the depth profiling from the surface to a specimen depth of about 500 nm. Therefore, the micro structural changes in very small and thin specimens could be studied. Thanks to this technique and very small volume of specimens, the disturbing contribution of ⁶⁰Co radiation in the PAS lifetime spectra were

reduced to a minimum. In our case, identical specimens were used for PAS and MS study. Such approach seems to be optimal due to possible inhomogenities in different specimens from the same steels. Nevertheless, there exist many open questions and there is a need for further investigation. Interpretation of PAS and MS results is neither easy nor straightforward. Both techniques are very sensitive to sample preparation and handling.

It was shown that MS as well PLEPS can see the formation of solute clusters during irradiation of RPV steels, resulted in depletion of Cu and P in the matrix in the first period of irradiation. Some alloying elements (for example Ni) can slightly retard this depletion [56]. After this first period, both techniques registered no significant changes connected to increased neutron treatment. In the contrary, the positron lifetimes decreased probably due to long-term thermal treatment on the level of 280 °C. Using PLEPS, the most effective region (450-470 °C) of thermal treatment was clearly shown at base as well as weld metals. Positron annihilation techniques can be applied for the development of new types of steels with well-defined parameters (materials for fusion reactors, etc.) or by the evaluation of the effectiveness of post-irradiation thermal treatments [57]. Application of a scanning positron microscope in the RPV-steel investigation would be surely one of the ways in the future [58].

The results from the present extensive study of RPV surveillance specimens indicate that MS and PAS could be useable techniques for the evaluation of some microstructural changes in RPV-steels and, in combination with other spectroscopic methods can contribute to an increase of NPPs operational safety and lifetime prediction. However, neither this method is a magic wand solving all substantial questions in neutron embrittlement and material ageing. This investigation will continue also in the next period and specimens treated in reactor up to 10 years will be studied. Such loaded specimens will be equivalent to real RPV steel after more than 50 years of operation and will be interesting for the RPV lifetime management.

Acknowledgement

We would like to thank IAEA (Research contracts SLR10994, SLR11120), VEGA 1/3188/06 and VEGA 1/0129/09 as well as to SE-EBO Bohunice, plc. for support. For the

possibility to use PLEPS technique and for valuable scientific discussions we acknowledge Prof. W. Triftshäuser, Dr. W. Egger, Dr. G. Kögel and Dr. P. Sperr from Universität der Bundeswehr in Neubiberg (Germany).

References

- [1] Davies, L.M., *Int. J. Press. Ves. & Piping*, 76 (1999) 163.
- [2] Nikolaev, Y.A., Nikolaeva, A.V., Kryukov, A.M., Shtrombakh, Y.I. and Platonov, P.A., *Proc. of the TACIS Workshop on the RPV Life Predictions, PCP3-ENUCRA-D4* (2000).
- [3] Ghoniem, M.M. and Hammad, F.H., *Int. J. Press. Vess. & Piping*, 74 (1997) 189.
- [4] Kohopaa, J. and Ahlstrand, R., *Int. J. Press. Vess. & Piping*, 76 (2000) 575.
- [5] Debarberis, L., von Estorff, U., Crutzen, S., Beers, M., Stamm, H., de Vries, M.I. and Tjoa, G.L., *Nucl. Eng. Des.* 195 (2000) 217.
- [6] U.S. NRC Regulatory Guide 1.99, Rev.1, (1977).
- [7] Suzuki, K., IAEA report, IWG-LMNPP-98/3, (1998).
- [8] Grosse, M., Denner, V., Böhmert, J. and Mathon, M.H., *J. Nucl. Mater.* 277 (2000) 280.
- [9] Koutsky, J. and Kocik, J., "Radiation damage of structural materials", ed. Academia Prague, (1994).
- [10] Phythian, W.J. and English, C.A., *J. Nucl. Mater.* 205 (1993) 162.
- [11] Brauer, G., Liskay, L., Molnar, B. and Krause, R., *Nucl. Eng. & Desg.* 127 (1991) 47.
- [12] Pareja, R., De Diego, N., De La Cruz, R.M. and Del Rio, J., *Nucl. Technol.* 104 (1993) 52.
- [13] Lopes Gil, C., De Lima, A.P., Ayres De Campos, N., Fernandez, J.V., Kögel, G., Sperr, P., Triftshäuser, W. and Pachur, D., *J. Nucl. Mater.* 161 (1989) 1.
- [14] Slugen, V., Zeman, A., Petriska, M. and Krsjak, V., *Applied surface science*, 252 (2006) 3309.
- [15] Valo, M., Krause, R., Saarinen, K., Hautojärvi, P. and Hawthorne, R., *ASTM STP 1125*, Stoller, Philadelphia, (1992).
- [16] Hartley, J.H., Howell, R.H., Asoka-Kumar, P., Sterne, P.A., Akers, D. and Denison, A., *Appl. Surf. Sci.* 149 (199) 204.
- [17] Becvar, F., Cizek, J., Lestak, L., Novotny, I., Prochazka, I. and Sebesta, F., *Nucl. Instr. Meth. A* 443 (2000) 557.
- [18] Miller, M.K., Russel, K.F., Kocik, J. and Keilova, E., *J. Nucl. Mater.* 282 (2000) 83.
- [19] Cizek, J., Becvar, F. and Prochazka, I., *Nucl. Instr. Meth. A* 450 (2000) 325.
- [20] Cizek, J., Prochazka, I., Kocik, J. and Keilova, E., *phys. stat. sol. (a)* 178 (2000) 651.
- [21] Van Hoorebeke, L., Fabry, A., van Walle, E., Van de Velde, J., Segers, D. and Dorikens-Vanpraet, L., *Nucl. Instr. Meth. A* 371 (1996) 566.
- [22] Ghazi-Wakili, K., Zimmermann, U., Brunner, J., Tipping, P., Waeber, W.B. and Heinrich, F., *Phys. Stat. Sol. (a)* 102 (1987) 153.
- [23] Slugen, V., Segers, D., De Bakker, P.M.A., DeGrave, E., Magula, V., Van Hoecke, T. and Van Waeyenberge, B., *J. Nucl. Mater.* 274 (1999) 273.
- [24] Slugen, V. and Magula, V., *Nucl. Eng. Desg.* 186(3) (1998) 323.
- [25] Slugen, V., De Grave, E. and Segers, D., *Int. J. Nuclear Energy Science and Technology*, 1(1) (2004) 20.
- [26] Slugen, V., Hascik, J., Gröne, R., Bartik, P., Zeman, A., Kögel, G., Sperr, P. and Triftshäuser, W., *Material Science Forum*, 47 (2001) 363.
- [27] Magula, V. and Janovec, J., *Ironmaking and Steelmaking*, 21 (1994) 64.
- [28] Kocik, J., Keilova, E., Cizek, J. and Prochazka, I., *Proc. of 9th Int. Conf. on Metallurgy METAL 2000*, (CD-ROM), Ostrava, Czech Republic, Tanger Ltd., (2000), paper No.719.

- [29]Lipka, J., Hascik, J., Slugen, V., Kupca, L., Miglierini, M., Gröne, R., Toth, I., Vitazek, K. and Sitek, J., Proc. Int. Conf. ICAME'95, Vol. 50, I. Ortalli (ed.), SIF, Bologna, (1996), 161.
- [30]Cohen, L., "Application of Mössbauer spectroscopy". Volume II. (Academic Press, New York, 1980).
- [31]Brauer, G., Matz, W. and Fetzer, Cs., Hyperfine Interaction, 56 (1990) 1563.
- [32]Amaev, A.D., Dragunov, Yu.G., Kryukov, A.M., Lebedev, L.M. and Sokolov, M.A., Proc. of IAEA specialists meeting of RPV embrittlement, Plzeň, (1986).
- [33]Slugen, V., "Mössbauer spectroscopy in material science", In: M. Miglierini and D. Petridis (eds.), 119-130, (Kluwer Academic Publishers, Netherlands, 1999).
- [34]De Bakker, P., Slugen, V., De Grave, E., Van Walle, E. and Fabry, A., Hyperfine Interaction. 110 (1997) 11.
- [35]Puska, M.J., Sob, M., Brauer, G. and Korhonen, T., Phys. Rev. B, 49 (1994) 10947.
- [36]Böhmert, J. and Grosse, M., Proc. of Jahrestagung Kerntechnik 1998, ed. Inforum Verlag, Bonn, (1998), 741.
- [37]Davies, M., Kryukov, A., English, C., Nikolaev, Y. and Server, W., ASTM STP 1366 (2000).
- [38]Nagai, Y., Tang, Z., Hasegawa, M., Kanai, T. and Saneyasu, M., Phys. Rev. B, 63 (2001) 131110.
- [39]Mukouda, I. and Shimomura, Y., Mat. Sci & Eng. 190 (2001) A309.
- [40]Brandt, W., "Positron Annihilation", A.T. Stewart and L.O. Roelling (eds.), (Academic Press, New York, 1967), p.155.
- [41]Frank, W. and Seeger, A., Appl. Phys. 3 (1974) 61.
- [42]Seeger, A., Appl. Phys. 4 (1974) 183.
- [43]Nieminen, R.N., Laakkonen, J., Hautojärvi, P. and Vehanen, A., Phys. Rev. B, 19 (1979) 1397.
- [44]Frieze, W.E., Lynn, K.G. and Welch, D.O., Phys. Rev. B, 31 (1985) 15.
- [45]Britton, D.T., J. Phys.: Condens. Matter, 3 (1991) 681.
- [46]Kögel, G., Appl. Phys. A, 63 (1996) 227.
- [47]Sperr, P., Kögel, G., Willutzki, P. and Triftshäuser, W., Applied Surface Science, 116 (1997) 78.
- [48]Bauer-Kugelmann, W., Sperr, P., Kögel, G. and Triftshäuser, W., Mater. Sci. Forum, 529 (2001) 363.
- [49]Dai, G.H., Moser, P. and Van Duysen, J.C., Mater. Sci. Forum, 941 (1992) 105.
- [50]Prochazka, I., Novotny, I. and Becvar, F., Mater. Sci. Forum, 772 (1997) 255.
- [51]Kupca, L. and Beno, P., Nucl. Eng. & Desg. 196 (2000) 81.
- [52]Gröne, R., Hascik, J., Slugen, V., Lipka, R., Pietryzk, P. and Vitazek, K., Nucl. Instr. & Meth. in Phys. Res. B, 129 (1997) 284.
- [53]Slugen, V., Hascik, J. and Gröne, R., International J. of Applied Electromagnetics and Mechanics, 11 (2000) 39.
- [54]Slugen, V., Lipka, J., Toth, I. and Hascik, J., NTD&E Int. 35(8) (2002) 511.
- [55]Slugen, V., Kögel, G., Sperr, P. and Triftshäuser, W., Appl. Surf. Sci. 194 (1-4) (2002) 150.
- [56]Zeman, A., Debarberis, L., Kocik, J., Slugen, V. and Keilova, E., J. of Nuclear Materials, 362 (2007) 259.
- [57]Slugen, V., Kuriplach, J. and Ballo, P., Nuclear Fusion, 44 (2004) 93.
- [58]David, A., Kögel, G., Sperr, P. and Triftshäuser, W., Phys. Rev. Lett. 87 (2001) 067402.
- [59]Hautojärvi, P., Pöllönen, L., Vehanen, A. and Yli-Kauppila, J., J. Nucl. Mater. 114 (1983) 250.
- [60]Vehanen, A., Hautojärvi, P., Johansson, J., Yli-Kauppila, J. and Moser, P., Phys. Rev. B, 25 (1982) 762.
- [61]Brauer, G., Sob, M. and Kocik, J., Report ZfK-647, (1990).
- [62]Slugen, V., Nuclear engineering and design, 235 (2005) 1961.
- [63]Zeman, A., Debarberis, L., Slugen, V. and Acosta, B., Applied surface science 252(9) (2006) 3290.

Jordan Journal of Physics

ARTICLE

Measurement of Radon -222 Concentration Levels in Spring Water in Iraq

R. M. Yousuf^a, M. M. Husain^b and L. A. Najam^b

^a*Environmental Technology Department, College of Environmental Science and Technology, Mosul University, Mosul, Iraq.*

^b*Department of Physics, College of Science, Mosul University, Mosul, Iraq.*

Received on: 6/10/2008; Accepted on: 16/7/2009

Abstract: This work describes the results of measurements on the concentrations of radon (²²²Rn) found in seven mineral water samples collected from some natural mineral springs at seven sites in Nenevah governorate of north region in Iraq. Heat drying method was used to concentrate the radioactive nuclides in measured samples. Test tubes technique employed to measure (²²²Rn) using (CR – 39) plastic nuclear track detectors. The activity density of (²²²Rn) ranges from (3.82 PCi / L) to (9.999 PCi / L); while the average value was (5.8054 PCi / L). All results were below the maximum contaminant level (MCL) for (²²²Rn) in drinking water as reported by Environmental Protection Agency (EPA).

Keywords: CR-39 plastic nuclear track detectors; Radon -222 concentration levels; MCL.

Introduction

Radiation is a natural part of the environment in which we live. All people receive exposure from naturally occurring radioactivity in soil, water, air and food. The largest fraction of the natural radiation exposure we receive comes from a radioactive gas, radon. Radon (²²²Rn) is emitted from uranium, a naturally occurring mineral in rocks and soil; thus, radon is present virtually everywhere in the air over the earth, but particularly over land, relative to that over water surface. Thus, low levels of radon are present in all the air we breathe [1].

Radon concentrations can be measured either in terms of a volume of air (Bq/m³) or a volume of water (Bq/L). As well as the amount of radon in air or water commonly is reported in terms of activity with units of (PCi/L) of air or water. An activity of (1 PCi/L) is about equal to the decay of two atoms of radon per minute in each liter of air or water [2].

Underground water often moves through rock containing natural uranium that releases radon to the water. Water from wells normally has much higher concentrations of radon than surface water such as lakes and streams.

Radon has also been identified as a public-health concern when present in drinking water. The World Health Organization (WHO) suggest that radon causes up to 15% of lung cancers worldwide [3].

In 1991, Environmental protection Agency (EPA) proposed a Maximum Contaminant Level (MCL) for radon of 11 Bq/L (about 300 PCi/L) for radon in drinking water. In 2000, the law of IAEA is required to set a new MCL based in part on this report. The law also directed EPA to set an alternative MCL (AMCL); an AMCL is the concentration of radon in water that would cause an increase of radon in indoor air that is no greater than the level of radon naturally present in outdoor air. Limiting public risk

from radon by treating the water alone is not feasible because radon is also naturally present in the air. Thus, the AMCL is the tool that allows (EPA) to limit exposure to radon in water to a practical level, that is, allowing no more risk from the radon in water than is posed by the level of radon naturally present in outdoor air [1].

Since radon is acknowledged as a cancer-causing substance, the law directs (EPA) to set a maximum contaminant level (MCL) for

radon to restrict the exposure of the public to the extent that is possible, that is, as close to zero as is feasible.

Experimental Procedure

Water samples (each of two liters) were collected from seven sites in Nenevah governorate of north region in Iraq, as shown in Fig. 1.

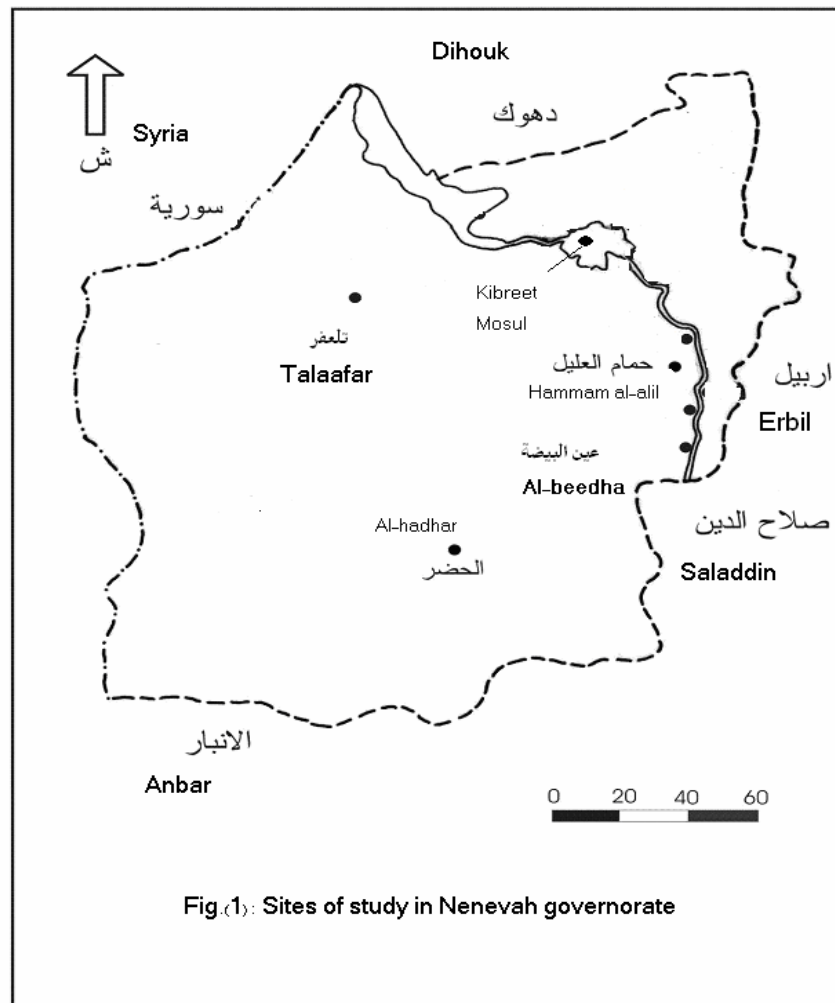


FIG. 1. Sites of study in Nenevah governorate

Test tube technique used to determine (^{222}Rn) levels in water samples, the calibration of such technique was discussed by Barillon *et al* [4].

Heat drying method employed to concentrate the radioactive nuclides in water samples. The powder (residual precipitate)

after drying each water sample was transferred to a test tube of diameter (2.1 cm), in order to measure (^{222}Rn) content using (CR-39) plastic solid state nuclear track detectors. The area of each detector was one cm^2 , see Fig. 2.

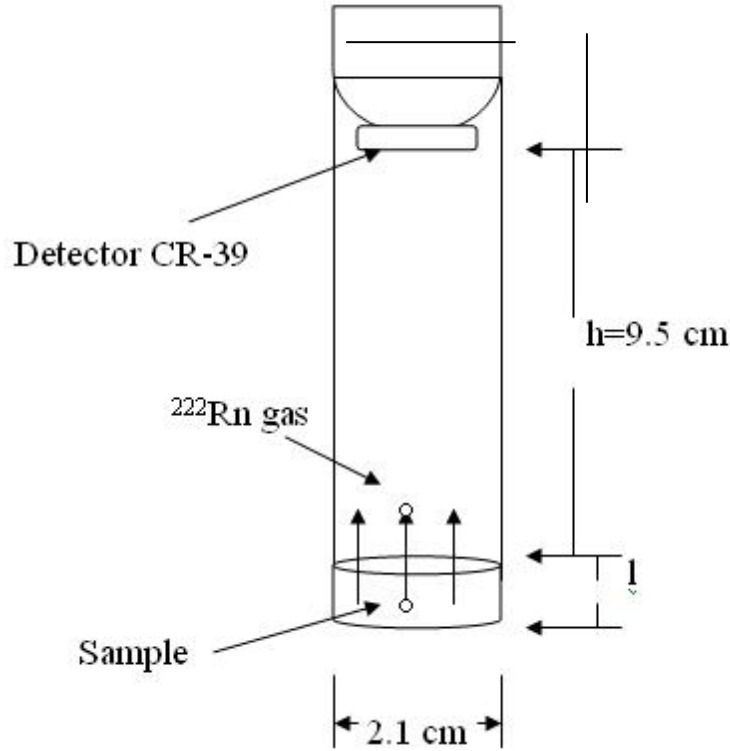


FIG. 2. Test tube technique used in the study.

After an exposure time of 60 days, the detectors were removed and chemically etched using a NaOH solution of normality (6.25 N) at temperature of 70°C with etching time of 5.5 hr. The alpha tracks per cm² in each detector were determined using an optical microscope.

Results and Discussion

In order to measure (²²²Rn) concentration levels in natural mineral spring water, the surface density of tracks on the employed detectors (ρ) measured in (Tr/cm²) unit used in the following equation [5]:

$$\rho = K . C . T \quad (1)$$

where,

C = ²²²Rn concentration within the test tube air, above the sample measured in (Bq/m³).

T = exposure time.

K = ²²²Rn gas diffusion constant [4]. Such that:

$$K = \frac{1}{4} r \left[2 \cos \theta_c - \frac{r}{R} \right]$$

$$= 1.31 \times 10^{-3} \left(\frac{Tr / \text{cm}^2 . \text{hr}}{\text{Bq} / \text{m}^3} \right)$$

where,

r = test tube radius = 0.0105 m.

θ_c = critical angle for CR-39 = 35 degree.

R = range of ²²²Rn alpha particle in air = 0.0415 m.

The ²²²Rn activity density (C_{Rn}) in the powder due to water sample in the test tube was determined according to the following relation [6]:

$$C_{Rn} = \frac{C . \lambda . h T}{l} \quad (2)$$

where,

λ = decay constant for (²²²Rn) = 7.554x10⁻³ (hr⁻¹).

h = distance from the powder surface to the detector = 0.095 m.

T = exposure time = 60 day = 1440 hr

l = depth of the powder. (m)

The activity of (^{222}Rn) in the water samples will be calculated in (Bq/L) unit from the following relation:

$$A_{Rn} = Q \cdot C_{Rn} \cdot V \quad (3)$$

where,

Q = Correction factor due to original volume of water sample (two liter) = 0.5.

V = Volume of the sample in the test tube
 $= \pi r^2 l (m^3)$.

Table 1 shows the results of radon levels in mineral water samples obtained in this work. The ρ refers to the net value of surface density for tracks on the detector (CR-39), which is equal to the difference between the surface density of tracks due to sample and the surface density of tracks due to background (131 Tr/cm²).

TABLE 1. Results of (^{222}Rn) activity in mineral spring water.

Spring name	$l (m)$	$\rho (Tr/cm^2)$	$A_{Rn} (Bq / L)$	$A_{Rn} (PCi / L)$
Kibreet(Mosul)	0.018	3900	0.3699	9.9992
Talaafar	0.008	2110	0.2002	5.4098
Al-shoura	0.015	1710	0.1622	4.3843
Al-beedha	0.018	1490	0.1414	3.8202
Al-gorn	0.016	3010	0.2855	7.7173
Hammam al-alil	0.018	1840	0.1746	4.7176
Al-hadhar	0.042	1790	0.1698	4.5894
Mean value			0.2148	5.8054

Because of the relatively small volume of water used in homes, the large volume of air into which the radon is emitted, and the exchange of indoor air with the ambient atmosphere, radon in water typically adds only a small increment to the indoor air concentration. Specifically, radon at a given concentration in water adds only about 1/10,000 as much to the air concentration; that is, typical use of water containing radon at 10,000 Bq/m³ will on average increase the air radon concentration by only 1Bq/m³. There is always radon in indoor air from the penetration of soil gas into homes, so only very high concentrations of radon in water will make an important contribution to the airborne concentration.

It has been difficult to set a standard for radon, in the same manner as for to other radionuclides in drinking water, because of the absence of authoritative dosimetric information for radon dissolved in water. Furthermore, radon presents a unique

regulatory problem in that its efficient transfer from water into indoor air produces a risk from the inhalation of its decay products. Thus, it is regulated as a radionuclide in water, but a major portion of the associated risk occurs because of its contribution to the airborne radon concentration [1].

The (EPA) has not established a (MCL) for radon in drinking water; however, the proposed (MCL) is (300 PCi/L) [3].

It is clear from Table 1 that all results were below the maximum contaminant level (MCL) for radon (^{222}Rn) gas in drinking water. As well as, the mean value of (^{222}Rn) activity in water samples is about ten times lower than the value of (MCL).

A comparison of the results obtained in this work is done with reported values for (^{222}Rn) levels in water spring samples of other workers as shown in Table 2.

TABLE 2. Comparison of (^{222}Rn) levels in spring water with results from other workers.

Sample type	Country (site)	Range (PCi/L)	Mean (PCi/L)	References
Cold spring	Jordan (Al-Karak)	3.568 – 14.43	7.32	[7]
Cold spring	Jordan (Irbid)	89.19 - 289.2	145.9	[6]
Cold spring	Mexico (Mexico)	3.16 – 63.84	25.3	[8]
	Iraq (Nenevah)	3.820 – 9.999	5.805	This work

Radon is a naturally-occurring radioactive gas that may cause cancer, and may be found in drinking water and indoor air. Some people who are exposed to radon in drinking water may have increased risk of getting cancer over the course of their lifetime, especially lung cancer. Radon in soil under homes is the biggest source of radon in indoor air, and presents a greater risk of lung cancer than radon in drinking water. As required by the Safe Drinking Water Act, EPA has developed a proposed regulation to reduce radon in drinking water that has a multimedia mitigation option to reduce radon in indoor [3].

Because radon is easily released by agitation in water, many uses of water release

radon into the indoor air, which contributes to the total indoor airborne radon concentration.

Since (10,000 PCi/L) in water translates to about (1 PCi/L) in air, relatively there is no need to worry about the health risks due to water- borne radon [1].

Conclusion

All results of this work shows that the water from the examined sources generally make only a small contribution to the indoor airborne radon concentration, so that the risk posed by radon released from water, is estimated to be lower than the risks posed by the other drinking water contaminants that have been subjected to regulation.

References

- [1]Nat' Academies Press., "Risk Assessment of Radon in Drinking Water", <http://www.nap.edu/openbook/>, (1999).
- [2]Otton, J.K., "The geology of radon: U.S. Geological Survey", (General Interest Publications of the U.S. Geological Survey, 1992) p28.
- [3]EPA, <http://www.epa.gov/>, (2005).
- [4]Barillon, R., Klein, D., Chambaudet, A. and Devillarde, C., Nucl. Tracks Radiat. Meas. 22(1-4) (1993) 281.
- [5]Azam, A., Naqvi, A. and Srivastava, D., Nucl. Geophys. 9(6) (1995) 653.
- [6]Al-Bataina, B., Ismail, A., Kullab, M., Abumurad, K. and Mustafa, H., Radiation Measurement, 28(1) (1997) 591.
- [7]Al-Bataina, B., Tarawneh, S. and Lataifeh, M., Abhath Al-yarmouk, Basic Sci. & Eng. 12(1) (2003) 221.
- [8]Segovia, N. and Bulbulian, S., *Revista Mexicana de Fisica*, 38 (1992) 242.

Preparation of Nanocrystalline $\text{BaFe}_{12-2x}\text{Co}_x\text{Ti}_x\text{O}_{19}$ by Ball Milling Method and their Magnetic Properties

Ibrahim Bsoul

Department of Physics, Al al-Bayt University, Mafraq, Jordan.

Received on: 29/1/2009; Accepted on: 12/4/2009

Abstract: Nanocrystalline $\text{BaFe}_{12-2x}\text{Co}_x\text{Ti}_x\text{O}_{19}$ with $0 \leq x \leq 1$ were prepared by a simple method of ball milling. Magnetic and SEM measurements show that the coercive field and average grain size is decreasing with the increase of Co-Ti substitution. IRM and DCD curves were measured in order to investigate the role of doping with Co-Ti on the interactions between particles in $\text{BaFe}_{12-2x}\text{Co}_x\text{Ti}_x\text{O}_{19}$ samples using the δm technique. Interaction investigation shows that δm for all samples examined is negative, which means interparticle interactions that assists the reversal mechanisms (demagnetizing like effect).

Keywords: Ball milling, Barium ferrite, Coercive field, Magnetization.

Introduction

Barium hexaferrite with a chemical formula $\text{BaFe}_{12}\text{O}_{19}$ is one of the most important compositions for perpendicular magnetic recording. Barium hexaferrite is suitable for magnetic recording due to its large saturation magnetization, good chemical stability, and low switching field distribution. On the other hand, barium hexaferrite can be used for high density magnetic recording if its particle size and its large anisotropy field were decreased. Because large particle size and high anisotropy field causes a poor overwrite modulation [1]. In order to reduce the anisotropy field and to satisfy the desired applications, many studies were taken out to modify the magnetic properties of barium hexaferrite by the substitution of the Fe^{3+} ions with cations such as ($\text{Sn}^{4+}, \text{Ni}^{2+}, \text{Ni}^{3+}, \text{Co}^{2+}, \text{Co}^{3+}, \text{Ti}^{4+}, \dots$) [2-4] or cations combinations such as (Zn-Sn, Co-Sn [5, 6], Zn-Ti [7], Co-Ti [2], etc.).

Several techniques can be used to prepare barium ferrite powders such as the sol-gel method [8-10], the glass crystallization

method [11], hydrothermal technique [12], and coprecipitation method [13]. In the present work ball milling method was used to synthesize single-phase substituted nanocrystalline barium hexaferrite powder ($\text{BaFe}_{12-2x}\text{Co}_x\text{Ti}_x\text{O}_{19}$). The advantage of the above method is its operation simplicity and handy experimental apparatus. The preparation and investigation of barium ferrite doped with Co-Ti was reported in many works [14-17], but none of these works -to the knowledge of author- used the ball milling method. So in this work we have investigated the possibility of doping hexaferrites with ions such as Co-Ti by the ball milling route.

The structure of $\text{BaFe}_{12}\text{O}_{19}$ is of the form RSR^*S^* , Where R^* and S^* are obtained from the blocks R and S, by rotation of 180° around the hexagonal c axis. The ferric ions are distributed among five crystallographic sites. Three are octahedral sites ($12k, 4f_{IV}$, and $2a$); one is tetrahedral

site ($4f_{VI}$) and one trigonal bipyramid (2b)[18, 19].

Experimental procedures

The starting materials for synthesis of $BaFe_{12-2x}Co_xTi_xO_{19}$ ($x = 0, 0.2, 0.4, 0.6, 0.8$ and 1.0) were $BaCO_3$ (Aldrich-make), Fe_2O_3 (Aldrich-make), TiO_2 (Aldrich-make) and CoO (Aldrich-make). $BaFe_{12-2x}Co_xTi_xO_{19}$ compound was prepared in a planetary ball-mill (Fritsch Pulverisette 7) with balls and vial of hardened steel. The milling experiment was carried out at 250 rpm for 16 h and the ball to powder ratio was 8:1. The as-milled powders were annealed in air atmosphere at $1100^\circ C$ for 10 h. It should be noted that XRD analyses of more than 6 samples subjected to different annealing temperatures from $700^\circ C$ to $1200^\circ C$ revealed that the optimum annealing temperature for obtaining barium ferrite doped with Co-Ti was $1100^\circ C$. X-ray diffraction (XRD) analysis was carried out in Philips X'Pert PRO X-ray diffractometer (PW3040/60) with CuK_α radiation (45 kV, 40 mA). The obtained XRD data was compared with standard patterns of JCPDS-ICDD (International Center for Diffraction Data). The micrographs of the prepared samples were examined by the direct observation via

scanning electron microscopy (SEM) with EDX facilities (model FEI Quanta 600). The magnetic measurements were carried out using vibrating sample magnetometer (VSM) (MicroMag 3900, Princeton Measurements Corporation), with a maximum applied field of 795 kA/m. All magnetic measurements were performed at room temperature.

Results and discussion

Fig. 1 shows XRD patterns of Co and Ti doped barium ferrites ($BaFe_{12-2x}Co_xTi_xO_{19}$) with different doping concentration together with the standard pattern for $BaFe_{12}O_{19}$. The main diffraction peaks appearing in all XRD patterns can be indexed with the standard pattern for M-type hexagonal barium ferrite ($BaFe_{12}O_{19}$) with space group $P63/mmc$ (JCPDS file no: 043-0002), except a small peak at $2\theta = 33^\circ$ which belongs to Fe_2O_3 . In Table 1 we summarize the composition dependence of lattice parameters determined by X-ray diffraction and average crystallite size deduced from full width of half maximum using Scherrer's equation [20]. From these data we may propose that doping of barium ferrite with Co and Ti leads to an increase in lattice parameters and a decrease in average crystallite size.

TABLE 1. Lattice parameters and average crystallite size of $BaFe_{12-2x}Co_xTi_xO_{19}$, measured by XRD.

x	$a = b$ (Å)	c (Å)	Average crystallite size (D) nm
0	5.892	23.198	76
0.2	5.892	23.183	70
0.4	5.892	23.198	68
0.6	5.892	23.183	70
0.8	5.892	23.198	67
1.0	5.894	23.215	60

Fig. 2 shows the SEM photographs of Co and Ti doped barium ferrite powder with doping concentration of 0.0, 0.4 and 0.8. The grain size for the pure sample ($x = 0.0$) ranges from $0.2 \mu m$ to $1 \mu m$, while for $x = 0.8$ ranges from $0.2 \mu m$ to $0.6 \mu m$. So the average grain size tends to decrease with the increase of Co and Ti concentration i.e. Co and Ti doping results in inhibition of grain growth which

agrees with previous works [17, 19]. It is interesting that the particles stick to each other due to their magnetic attraction. So the particle sizes observed from SEM measurements seem to be larger than those measured by XRD. Also, the sample seems to form clusters rather than columns of stacked platelets, which indicates presence of negative interactions between particles.

Fig. 3 shows the measured hysteresis loops for some of the $\text{BaFe}_{12-2x}\text{Co}_x\text{Ti}_x\text{O}_{19}$ samples as a function of applied magnetic field. The magnetization curve for the non-substituted sample belongs to hard magnetic material with high coercive field strength of 334 kA/m. This value of the coercivity is in a good agreement with the previous reports such as sol-gel method [18], mechanical

alloying method [1] and ball milling method [21] of preparing barium ferrite. The effect of Co-Ti ions on the saturation magnetization and coercivity of $\text{BaFe}_{12-2x}\text{Co}_x\text{Ti}_x\text{O}_{19}$ are shown in Fig. 4. The saturation value of magnetization was obtained by extrapolating the magnetization versus $1/H$ to $1/H = 0$.

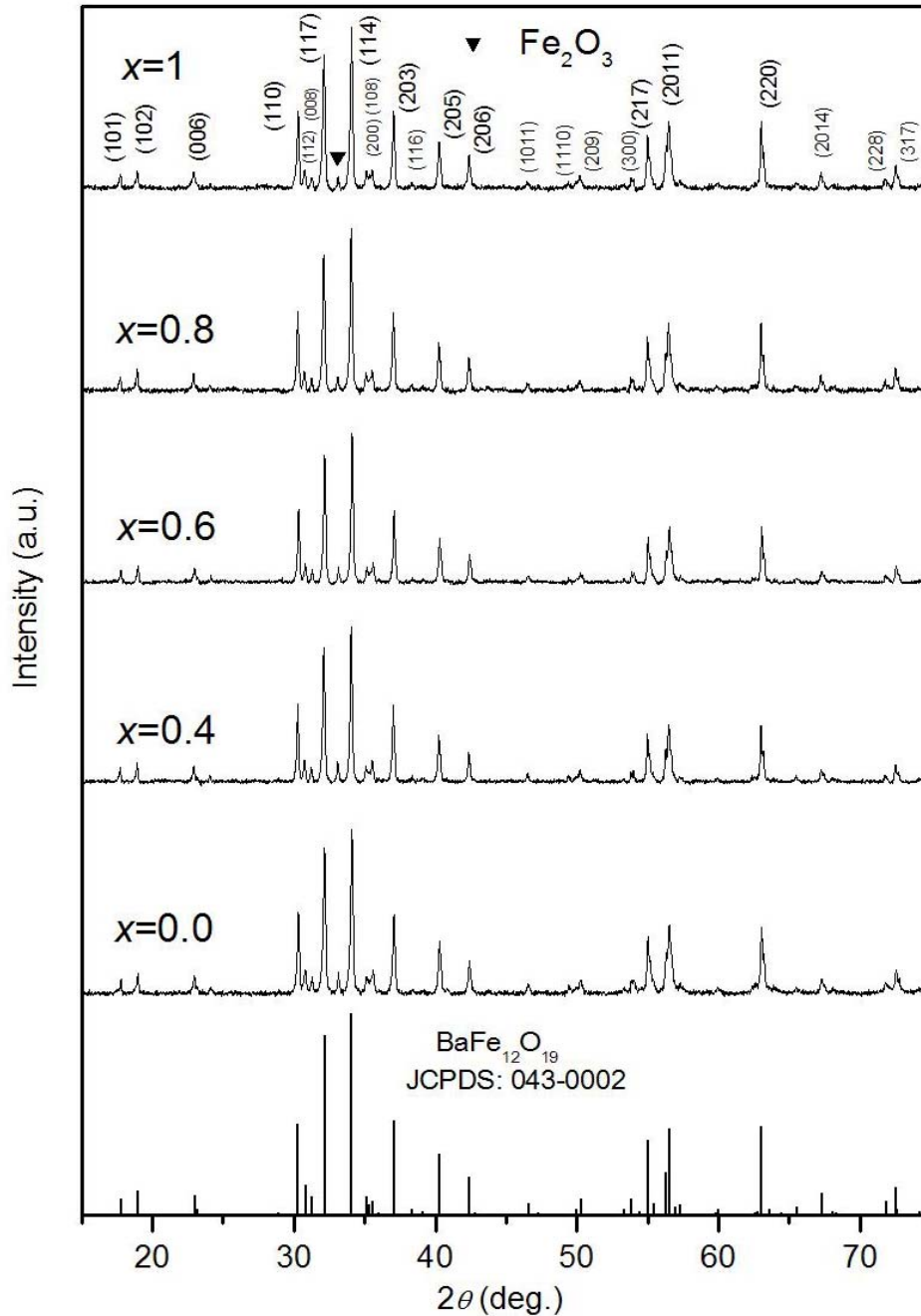


FIG. 1. Standard JCPDS pattern for M-type hexagonal barium ferrite (file no: 043-0002) and XRD patterns of $\text{BaFe}_{12-2x}\text{Co}_x\text{Ti}_x\text{O}_{19}$ with different doping concentration.

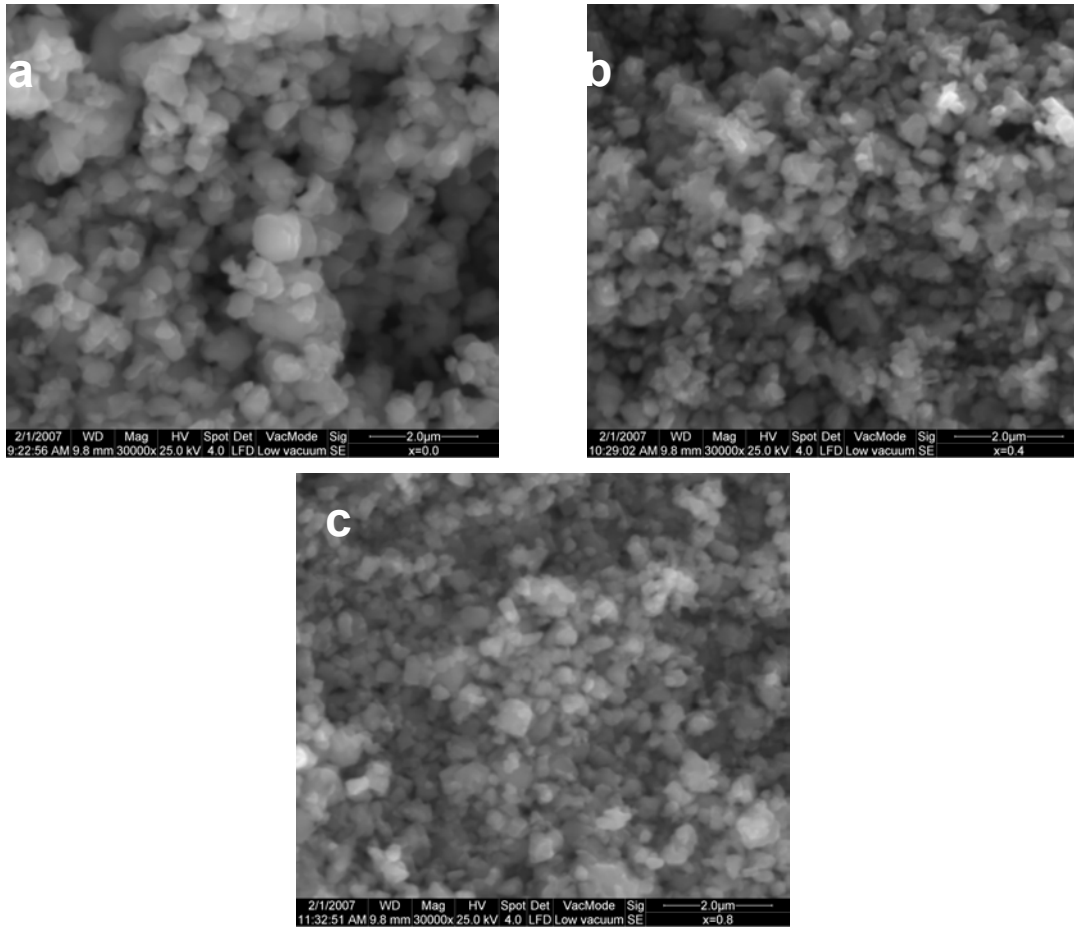


FIG. 2. SEM photograph of BaFe_{12-2x}Co_xTi_xO₁₉, a) $x = 0.0$, b) $x = 0.4$ and c) $x = 0.8$.

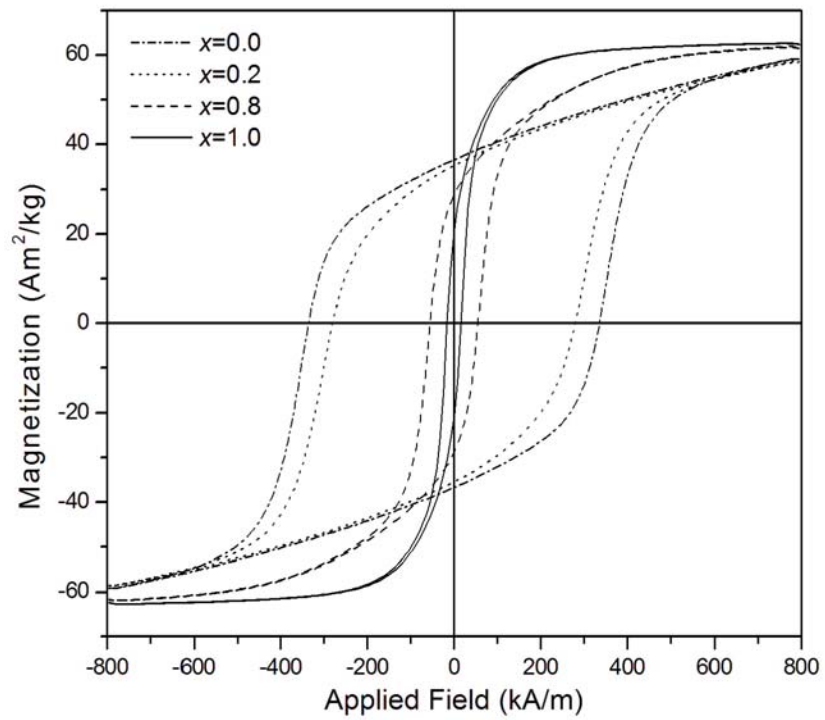


FIG. 3. Hysteresis loops for some of the BaFe_{12-2x}Co_xTi_xO₁₉ samples as a function of applied magnetic field.

The saturation magnetization for the samples examined in this work ranges from 64 Am²/kg to 72 Am²/kg, which is higher than 50 Am²/kg reported by Radwan *et al.* [22], where they used chemical co-precipitation method for synthesis of barium ferrite powder. With increasing x the magnetization slightly decreases for all samples examined, which is suitable for applications such as perpendicular magnetic recording, microwave devices and material for permanent magnets where a high saturation magnetization is desired. While the coercivity drops dramatically from about 334 kA/m to 16

kA/m with the increasing of x from 0.0 to 1.0, which enables us to control the coercivity for various types of applications. As it was reported in literature [18, 23-25,] the iron ions at each of the five sites make a special contribution to the magnetic properties of BaFe₁₂O₁₉. A summary of these contributions is shown in Table 2. As one might see the major contribution to the coercivity comes from iron ions at 4f_{V1} and 2b. Therefore the dramatic drop of the coercivity (Fig. 4) can be referred to the replacement of Fe ions by Co and Ti ions at 4f_{V1} and 2b sites.

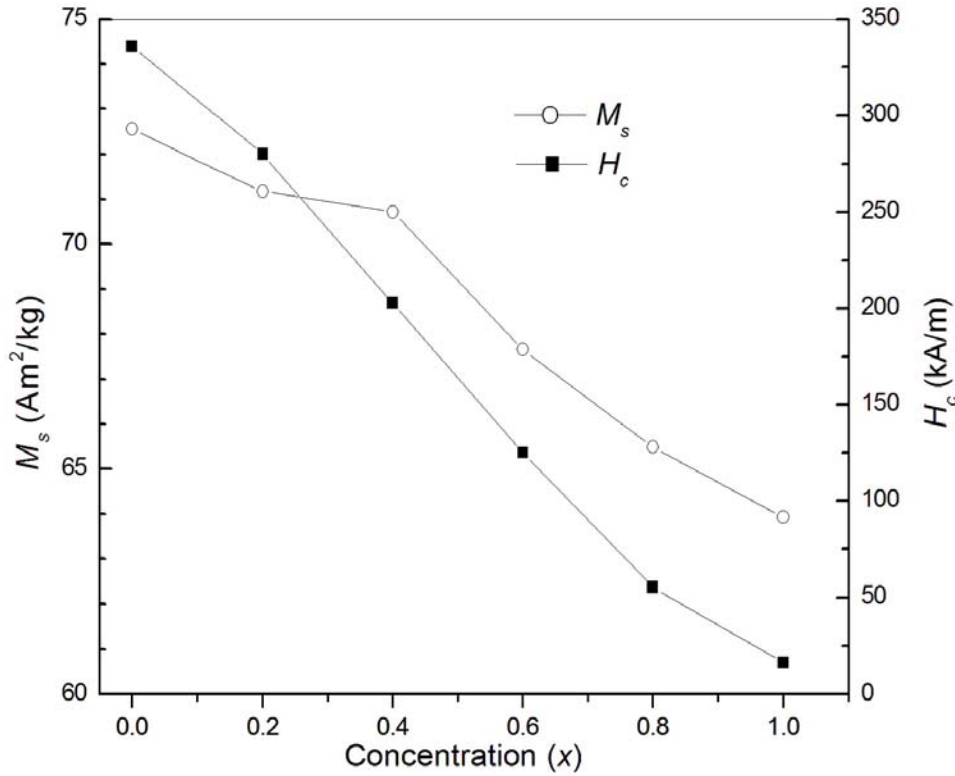


FIG. 4. Saturation magnetization and coercivity of BaFe_{12-2x}Co_xTi_xO₁₉ as a function of the concentration (x).

TABLE 2. Magnetic properties of crystallographic sites in barium ferrite (BaFe₁₂O₁₉).

Sites	Coordination	Spin direction	Contribution
4f _{V1}	octahedral	down	coercivity
2b	bipyramid	up	coercivity
4f _{IV}	tetrahedral	down	magnetization
12k	octahedral	up	temperature dependence of magnetization
2a	octahedral	up	

In order to investigate the role of doping with Co-Ti on the interaction effects we use δM relationship given by Kelly [26]:

$$\delta m(H) = m_d(H) - [1 - 2m_r(H)] \quad (1)$$

where $m_r(H) = M_r(H)/M_r(\infty)$ is the reduced isothermal remnant magnetization (IRM) and $m_d(H) = M_d(H)/M_r(\infty)$ is the reduced dc demagnetization (DCD). The IRM curve was obtained by the following

procedure: first the sample was demagnetized, second applying positive field, third measuring the remanence magnetization after removing the applied field. The procedure was repeated with increasing the positive field to reach positive saturation remanence. The DCD curve was obtained by, first, the sample was saturated with a positive field of 795 kA/m, second a negative field was applied to the sample, third, the remanence magnetization was recorded after removing the negative field and at last this procedure was repeated with increasing the negative field until negative saturation remanence was reached. The IRM and DCD curves for all samples examined in this work are shown in Fig. 5. By substituting these curves in eq. 1, we can obtain δm curves, which give the strength and the sign of the interaction in the prepared samples. For non interacting systems δm plots will show a horizontal line, any deviation from linearity in δm is a sign for the existence of

interparticle interactions. Positive δm values indicate the existence of interparticle interactions that contribute constructively to the magnetization (magnetizing like effect), i.e. particles tend to stack in column, while negative δm values suggest that the existing interactions are demagnetizing (demagnetizing like effect), i.e. particles tend to form clusters. Fig. 6 shows the δm curves as a function of the applied field for samples with different doping concentration of Co-Ti. As one can observe δm for all samples are negative for all fields, which agree with SEM observation of cluster formation. Also δm exhibit a maximum negative values at a field around coercivity. As one might observe the maximum negative value of δm exhibits minimum at $x = 0.4$ and 0.6 . This behavior needs a further investigation to clarify the influence of doping on the strength of interparticle interactions.

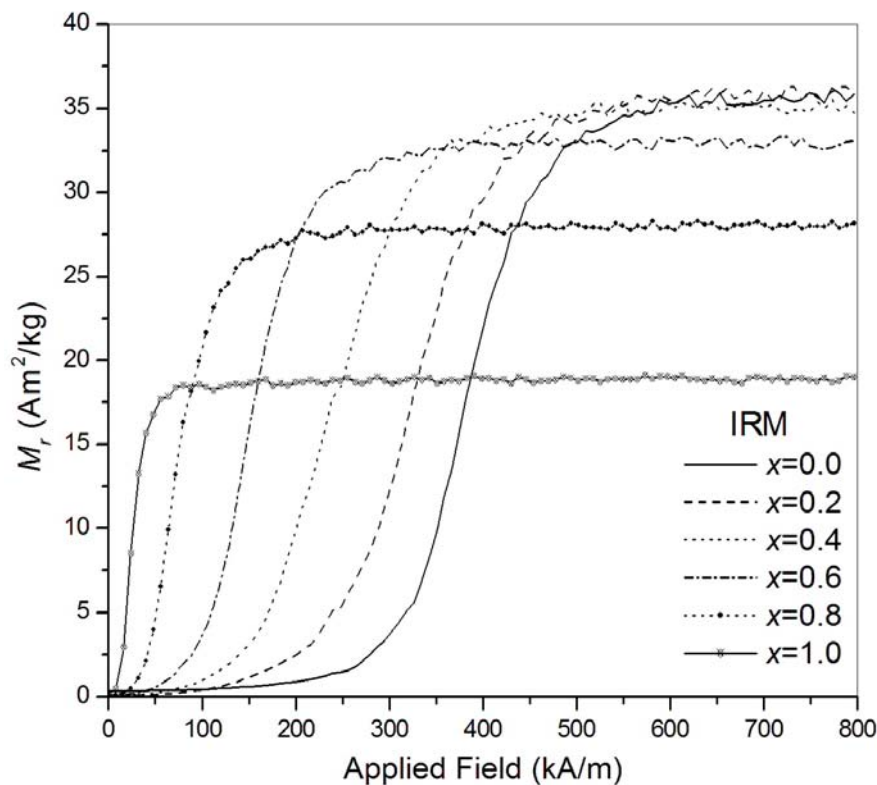


FIG. 5A. IRM curves of $\text{BaFe}_{12-2x}\text{Co}_x\text{Ti}_x\text{O}_{19}$.

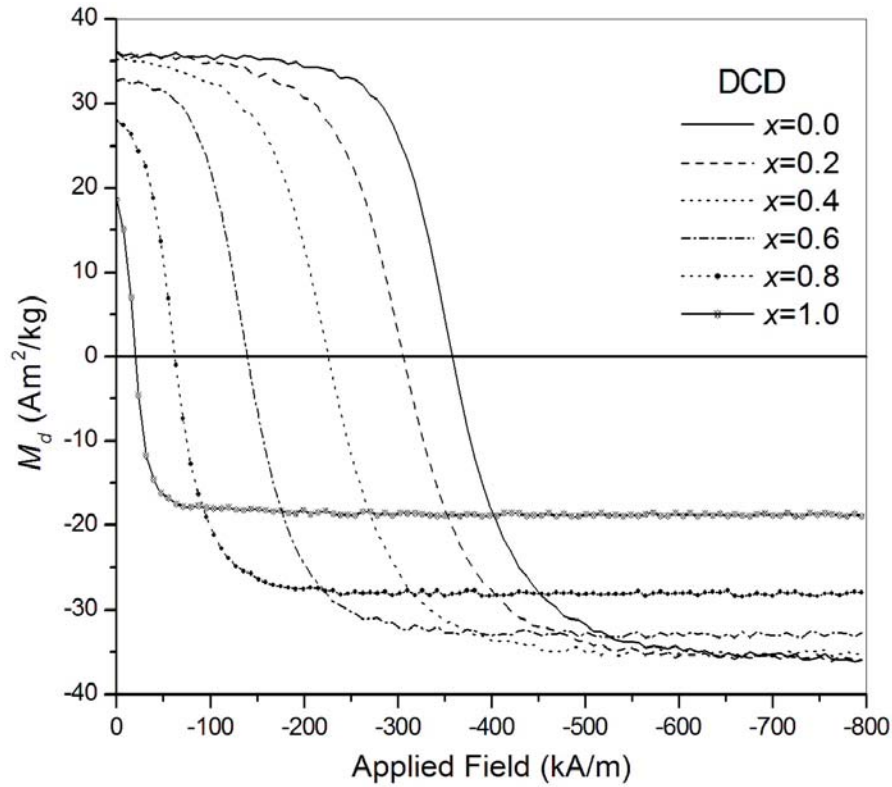


FIG. 5B. DCD curves of $\text{BaFe}_{12-2x}\text{Co}_x\text{Ti}_x\text{O}_{19}$.

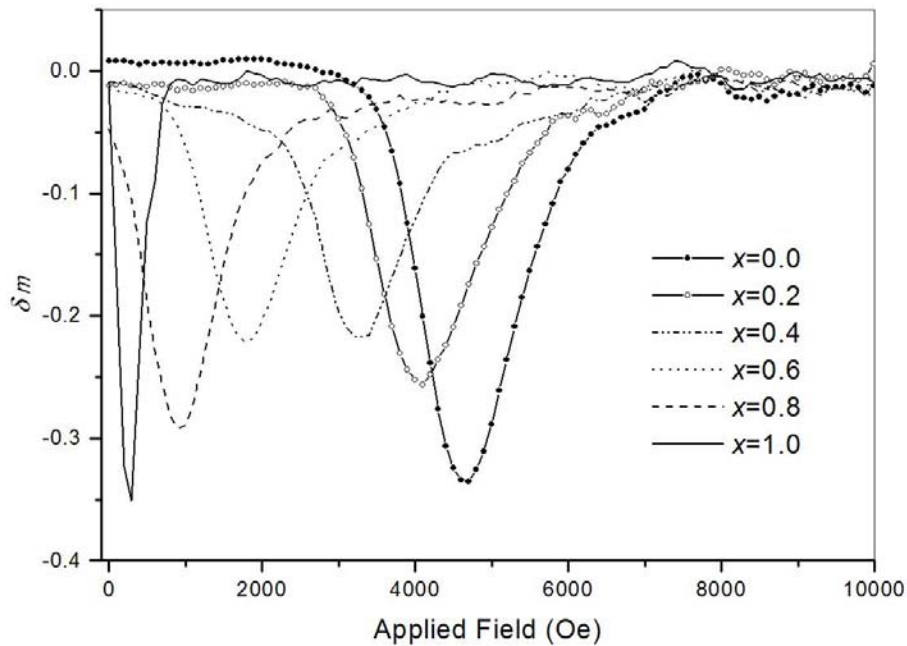


FIG. 6. δm curves of $\text{BaFe}_{12-2x}\text{Co}_x\text{Ti}_x\text{O}_{19}$ for some of the concentration examined

Conclusion

Nanocrystalline barium ferrite doped with Co-Ti ($\text{BaFe}_{12-2x}\text{Co}_x\text{Ti}_x\text{O}_{19}$) have been prepared using a very simple method of ball milling. It was found that doping of barium ferrite with Co-Ti leads to a significant decrease in the coercive field and inhibition of grain growth. Interaction investigation

show that δm for all samples examined is negative, which means interparticle interactions that assists the reversal mechanisms (demagnetizing like effect).

Acknowledgment

This work was supported by Deanship of Academic Research at Al al-Bayt University (Grant No. 213/2004/2005).

References

- [1] Sharma, P., Rocha, R.A., de Medeiros, S.N. and Paesano Jr, A., *Journal of Alloys and Compounds*, 443(1-2) (2007) 42.
- [2] Gruskova, A., Slama, J., Dosoudil, R., Kevicka, D., Jancarik, V. and Toth, I., *J. Magn. Magn. Mater.* 242–245 (2002) 423.
- [3] An, S.Y., Shim, I.B. and Kim, C.S., *J. Appl. Phys.* 91 (2002) 8465.
- [4] Marino-Castellanos, P.A., Somarriba-Jarque, J.C. and Anglada-Rivera, J., *Physica B: Cond. Mat.* 362 (2005) 95.
- [5] Yang, Z., Zeng, H.X., Han, D.H., Liu, J.Z. and Geng, S.L., *J. Magn. Magn. Mater.* 115 (1992) 77.
- [6] Han, D.H., Yang, Z., Zheng, H.X., Zhou, X.Z. and Morrish, A.H., *J. Magn. Magn. Mater.* 137 (1994) 191.
- [7] Wartewig, P., Krause, M.K., Esquinazi, P., Rosler, S., Sonntag, R., *J. Magn. Magn. Mater.* 192 (1999) 83.
- [8] Surig, C., Hempel, K.A. and Sauer, Ch., *J. Magn. Magn. Mater.* 157–158 (1996) 268.
- [9] Zhong, W., Ding, W., Zhang, N., Hong, J., Yan, Q. and Du, Y., *J. Magn. Magn. Mater.* 168 (1997) 196.
- [10] Garcia, R.M., Ruiz, E.R., Rams, E.E. and Sanchez, R.M., *J. Magn. Magn. Mater.* 223 (2001) 133.
- [11] El-Hilo, M., Pfeiffer, H., O'Grady, K., Schuppel, W., Sinn, E., Gornert, P., Rosler, M., Dickson, D.P.E. and Chantrell, R.W., *J. Magn. Magn. Mater.* 129 (1994) 339.
- [12] Liu, X., Wang, J., Gan, L.M. and Ng, S.C., *J. Magn. Magn. Mater.* 195 (1999) 452.
- [13] Zhao, W.Y., Zhang, Q.J., Li, L.C. and Guan, J.G., *J. Magn. Magn. Mater.* 295 (2005) 21.
- [14] Koga, N. and Tsutaoka, T., *J. Magn. Magn. Mater.* 313 (1) (2007) 168.
- [15] The, G.B., Saravanan, N. and Jefferson, D.A., *Materials Chemistry and Physics*, 105(2-3) (2007) 253.
- [16] Kakizaki, K., Hiratsuka, N. and Namikawa, T., *J. Magn. Magn. Mater.* 176 (1997) 36.
- [17] Yang, Z., Zeng, H.X., Han, D.H., Liu, J.Z., Geng, S.L., *J. Magn. Magn. Mater.* 115 (1992) 77.
- [18] An, S.Y., Shim, I.B. and Kima, C.S., *J. Appl. Phys.* 91(10) (2002).
- [19] Zhou, X.Z., Morrish, A.H., Li, Z.W. and Hong, Y.K., *IEEE Transactions on Magnetism*, 27(6) (1991).
- [20] Warren, B.E. "X-Ray Diffraction", (Addison-Wesley, Reading Massachusetts, 1969) p.253.
- [21] Babu, V., Padaikathan, P., *J. Magn. Magn. Mater.* 241 (2002) 85.
- [22] Radwan, M., Rashad, M.M. and Hessien, M.M., *Journal of Materials Processing Technology*, 181 (2007) 106.
- [23] Kim C.S., An, S.Y., Son, J.H., Lee, J.G. and Oak, H.N., *IEEE Transactions on Magnetism*, 35(5) (1999) 3160.
- [24] Zhou, X.Z., Morrish, A.H., Li, Z.W. and Hong, Y.K., *IEEE Transactions on Magnetism*, 27(6) (1991) 4654.
- [25] Turilli, G., Licci, F., Rinaldi, S. and Deriu, A., *J. Magn. Magn. Mater.* 59(1-2) (1986) 127.
- [26] Kelly, P.E., O'Grady, K., Mayo, P.I. and Chantrell, R.W., *IEEE Transactions on Magnetism*, 25(5) (1989) 3881.

Monitoring the Development of Cotton (*Gossypium barbadense* L.) using Emission Spectra of Chlorophyll Fluorescence

S. T. Kafi^a, I. M. K. Medani^b, A. M. Ahmed^a and A. K. Sabir Ali^c

^a*School of Applied Physics, Faculty of Science and Technology, Al Neelain University, Khartoum, Sudan.*

^b*Physics Department, Faculty of Science and Applied Sciences, International University of Africa, Khartoum, Sudan.*

^c*School of Life Sciences, Faculty of Science and Technology, Al Neelain University, Khartoum, Sudan.*

Received on: 18/2/2009; Accepted on: 16/7/2009

Abstract: This work was proposed to monitor the growth and development of cotton (*Gossypium barbadense* L.) under different environmental conditions using emission spectra of chlorophyll a fluorescence from the intact leaves. The emitted fluorescence signal by cotton plants was measured using spectrometer/graphic and data analysis software. Cotton was grown in the summer season under sunlight exposure i.e. summer conditions, whereas in winter conditions the plants were grown in a shaded area. Both groups of plants were irrigated by tap water. Winter conditions exhibit environmental stress of temperature and light intensity. Monochromatic blue light of 450 nm was used as an excitation source to induce the chlorophyll fluorescence emission at 685 nm and 733 nm. The peak intensity ratio (P.I.R.), which is the ratio between maximum emitted light intensities at 685 nm and 733 nm respectively (I_{F685}/I_{F733}), and the area ratio (A.R.) which is the ratio between the areas under the curves of the two emission lines were used for monitoring the development of cotton, from the germination until the flowering. The results revealed that the summer conditions gave a faster seed germination rate and the best growth and development of cotton, while the stressing winter conditions expressed in delayed seed germination, poor growth that led to failure of flowering and immaturity. The peak intensity ratio and area ratio for the summer and winter conditions were found to follow linear relationships. The line slopes of the peak intensity ratio and area ratios were 1.36 and 0.46 and the intercepts were 0.04 and 0.04 respectively.

Keywords: Cotton; Summer and winter conditions; Fluorescence; Chlorophyll a; I_{F685}/I_{F733} .

Introduction

Monitoring of plant development by spectroscopic detection of electromagnetic radiation is a powerful, noncontact and nondestructive method. Plant tissues absorb the energy of the electromagnetic radiation in the visible region by the photosynthetic pigments (chlorophyll a, b, and carotenoids). This energy is used for the photosynthetic processes [1, 2]. Chlorophyll a (*Chl a*) molecules are arranged into two groups of

pigments known as photosystem I (PSI) and photosystem II (PSII). Each photosystem has antennae chlorophyll molecules embedding a reaction center (RC). When an antennae chlorophyll molecule absorbs photons, it transfers this energy to another nearby one until reaching the reaction center chlorophyll molecules [2, 3]. Part of the absorbed energy is lost during the migration from the pigment antennae to the reaction centers and can be dissipated by a variety of non-photochemical

processes. Such processes include the dissipation of heat and emission of small but diagnostically significant amount of the absorbed radiation. This emission which occurs in the red and far-red regions is termed as chlorophyll fluorescence i.e. $I_F 685$ and $I_F 733$ respectively. This fluorescence signal (I_F), is therefore, determined by the rate of constants of these competing reactions and by the fraction of open reaction center as only those which can contribute to the photochemical de-excitation. Any exciting light (laser or laser emitting diode) capable of inducing Chlorophyll a fluorescence can be used for plant development monitoring in agricultural and plant science applications.

The shape of the fluorescence emission spectrum of leaves depends on the wavelength of the excitation light [4] and the environmental conditions of the measurements. Incident ultra violet or blue light is absorbed by carotenoids and by the chlorophyll of the chloroplast already at the upper part of the leaf mesophyll i.e. palisade and spongy tissues which are responsible of the photosynthetic activity in plants. The major part of the blue excited chlorophyll has to cover a short distance before it finally leaves the leaf at the epidermis and the chlorophyll fluorescence is only slightly reabsorbed by *in situ* chlorophylls. However, in the case of red light, which is only absorbed by Chlorophyll a, a substantial part of the excitation light penetrates deeper into the leaf mesophyll. This will generate more reabsorption of the red light chlorophyll fluorescence [5]. It has been observed in recent studies [6, 7] that Chlorophyll a fluorescence obtained by ultra violet, violet and blue light excitation sources is a good method for plant monitoring. The absolute emission signal of leaves can vary from sample to sample due to leaves' heterogeneity [8, 9] and other small differences such as the excitation and sensing angles of the fluorescence, and the roughness and scattering properties of the leaf surface. Thus, the absolute fluorescence $I_F 685/$ or $I_F 733$ usually varies to a large degree than the fluorescence ratio $I_F 685/ I_F 733$ [1]. The fluorescence ratio, therefore, represents a more accurate tool for measuring the different changes in quantities of the fluorescence characteristics of leaves.

In the present work, the use of the blue or laser emitting diode (LED) to excite intact leaves Chlorophyll a from cotton crop during its development is reported. The analysis of the fluorescence spectra using peak intensity ratio and area ratio of $I_F 685$ and $I_F 733$ from the Gaussian curves fitting were performed to distinguish between cotton growing in summer conditions with equal exposure to sunlight, and cotton growing in winter in a shaded area. This technique has been established to discriminate between normal and stressing conditions in vegetation [10, 11]. The importance of such investigations is that, cotton is an important economical crop in the Sudan; a good portion of cooking oil is extracted from its seeds, and its flowers are used in weaving, textile and for various medical purposes.

Materials and method

Cotton is a warm weather fiber plant, which is grown normally from dry seeds, that is planted either in rows or scattered. Seeds are known to grow in different types of soils (sand or clay) but for optimum seed yield, heavy clay soils are preferred. Crops grow better under regular watering, but they don't suffer much otherwise.

Cotton seeds, brought from Gezira Scheme, were divided into two groups; one was grown in the summer conditions, directly exposed to sunlight, while the other was grown in the winter conditions, in a shaded place. Seasonality in this study is based on the sowing time of cotton seeds. Generally, agricultural activities in the Sudan are performed in two rotations which begin during late summer and early winter. In the Gezira Scheme, Sudan, sowing of cotton begins in June-July to mature in December. It should be noted that germination is considered as the most important stage in the life of cotton plants. The experiments were carried out at the Botanical Garden of the Faculty of Science, Al Neelain University, Khartoum, Sudan (altitude: $15^{\circ} 29'$ and $15^{\circ} 37'$ N and longitude: $32^{\circ} 33'$ and $32^{\circ} 34'$ E). Temperature in Khartoum has a very wide range, between 46° - 20° C in summer and 40° - 7° C in winter. The maximum temperature is reached in May-June and the minimum in January. The light intensity, measured as average sunshine/day, varies

between 8.1-9.6 hrs/day in summer season and between 9.7-10.3 hrs/day in winter. The area received 194 mm during 2006 in the form of erratic and inconsistent rains that occurred during late summer (July-September) [12]. The first seed group was grown during the 2006 rainy season (June), flowered in September and became fully matured in December of the same year. The second group was grown during December, 2006 (winter conditions). However, the plants of this group showed a poor growth rate and did not mature or flower.

Seeds were grown in eight pots that were filled with heavy clay soil to about 10 cm from the top. The average diameter of the pots is about 26 cm. The soil was collected from the bank of the Blue Nile near Khartoum. Sixteen plants were used for the measurements, two in each of the eight pots. Eight plants were grown and measured during the summer season. They were placed in four pots in an open space for equal exposure to sunlight. The other eight plants were placed in a shaded place and were similarly grown and measured during the winter season. To ensure successful germination, four seeds were put in each pot and after the seedling emergence; they were thinned to leave the two best plants. The pots in the summer and winter conditions were irrigated daily with tap water till the end of the experiments.

For the summer group, germination began five days after sowing and by the twelfth day, it was completed. But for the winter group, germination began four weeks after sowing due to low temperatures and was completed by the fifth week. The measurements of the fluorescence for the summer group started at the beginning of the third week after sowing, and are taken from different leaves on each plant in each pot. For the winter group, the measurements started at the beginning of the fifth week after sowing due to the slow rate of development of the plants. The measurements were taken in the same way as for the summer group i.e. from different points of the lower most and the upper most fully developed leaves and were then averaged.

A laser emitting diode (LED) emitting at 450 nm wavelength and output power of 60 μ W was used as an excitation source. A compact software controlled spectrometer

(USB2000/Origin 6.1, Ocean Optics/Origin Lab, Dunedin, USA/Northampton, USA) was used for recording the fluorescence signal emitted by the plants' intact leaf. The resolution of the spectrometer was 1.34 nm FWHM [13], and its detector covers the wavelength range from 350-1100 nm. The whole setup was coupled to a laptop computer for mobile use, to record field measurements. Recorded data were analyzed using MICROCAL ORIGIN 6.1 computer program. The software uses an algorithm curve fitting with a combination of Gaussian spectral functions to analyze the spectra.

Results and analysis:

The results of the measured chlorophyll a fluorescence intensity as a function of the wavelength for the summer group of cotton during the third to the eighth week after sowing are shown in Fig. 1A and Table 1 (A and B). For the winter group, the results were recorded during the fifth to the eighth weeks after sowing are shown in Fig. 1B and Table 2 (A and B). Each spectrum is the average of seven days, and each day spectrum is the average of 10 different leaves obtained from different plants of the same group.

The Gaussian fitting was performed as shown in Fig. 2, where the smoothing and the averaging of the randomness on the profile of the curve were done in addition to decomposing the peak into two overlapping peaks for area ratio evaluation. In addition, the full width at half maximum (FWHM), denoted as $\Delta\lambda$, was determined as shown in Tables 1 and 2.

The Chlorophyll a fluorescence spectra for the summer season cotton of the fifth measuring week with Gaussian curve fitting for I_F685 and I_F733 bands are shown in Fig. 2. The constituent bands were found to center around 685 nm and 732 nm. The evaluation of the standard errors for the wavelength at maximum peak (λ_{max}), fluorescence intensity peak amplitude (I_F) and the band area (A) indicated that the determination of the peaks is acceptable with minimum standard error. The parameters obtained for the two sets of plants, during the period of monitoring the development are listed in Table 1 for the summer conditions and in Table 2 for the winter conditions.

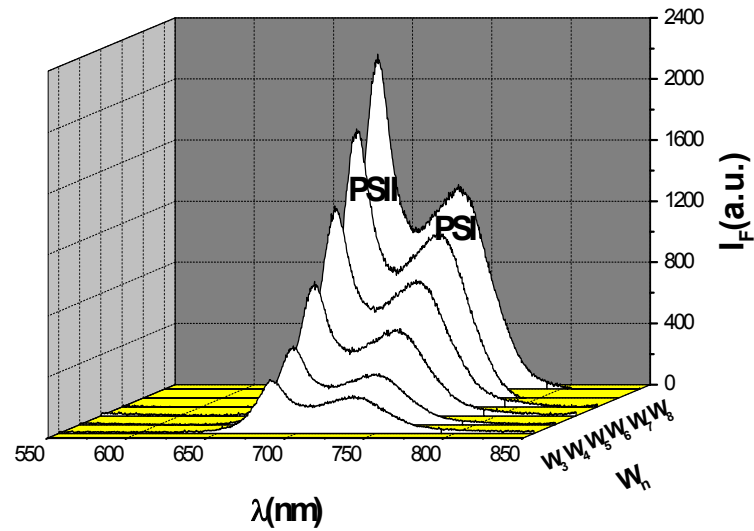


FIG. 1A

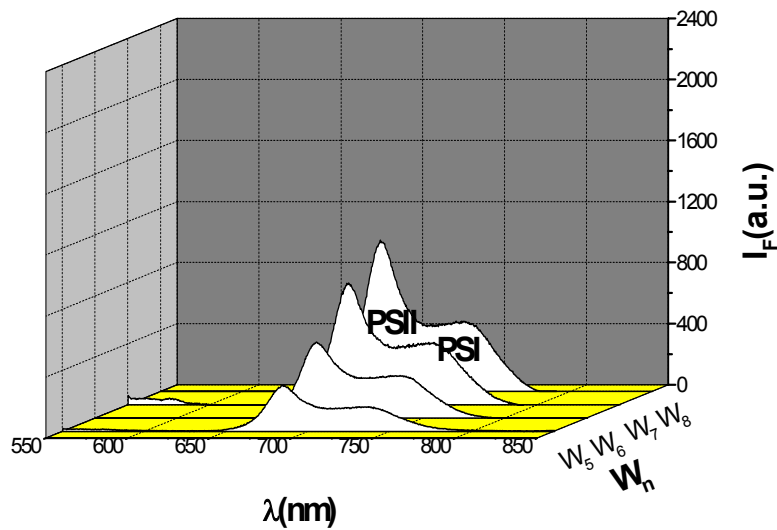


FIG. 1B

FIG. 1. Fluorescence spectra for the two groups of cotton: (A) under summer conditions; (B) under winter conditions; (W_n : Number of weeks)

TABLE 1A. Summer conditions. Parameters for I_F 685 band.

W_n	λ_{\max} (nm)	$\Delta\lambda$ (nm)	A (m^2)	I_F (a. u.)
W_3	685.2 ± 0.5	23.1 ± 0.3	0.90 ± 3.2	353.4 ± 0.5
W_4	685.3 ± 0.2	22.7 ± 0.4	1.34 ± 2.4	497.8 ± 0.3
W_5	685.1 ± 0.1	22.5 ± 0.3	2.10 ± 5.4	849.1 ± 0.6
W_6	685.1 ± 0.8	21.7 ± 0.6	3.43 ± 4.3	1307.6 ± 0.5
W_7	684.3 ± 0.7	21.4 ± 0.5	4.82 ± 3.3	1735.1 ± 0.3
W_8	684.1 ± 0.6	21.1 ± 0.3	6.15 ± 4.6	2209.2 ± 0.2

TABLE 1B. Summer conditions. Parameters for I_F 733 band.

W_n	λ_{\max} (nm)	$\Delta\lambda$ (nm)	A (m^2)	I_F (a. u)
W_3	734.3 ± 0.9	47.6 ± 0.7	1.4 ± 7.3	240.2 ± 0.7
W_4	734.4 ± 0.8	46.3 ± 0.6	1.9 ± 9.3	331.0 ± 0.5
W_5	733.0 ± 0.9	43.6 ± 0.5	2.9 ± 3.2	552.1 ± 0.4
W_6	733.8 ± 0.7	42.4 ± 0.1	4.4 ± 2.4	828.1 ± 0.3
W_7	733.8 ± 0.8	42.9 ± 0.4	5.8 ± 4.3	1075.0 ± 0.2
W_8	733.6 ± 0.6	42.2 ± 0.4	7.0 ± 5.3	1343.8 ± 0.1

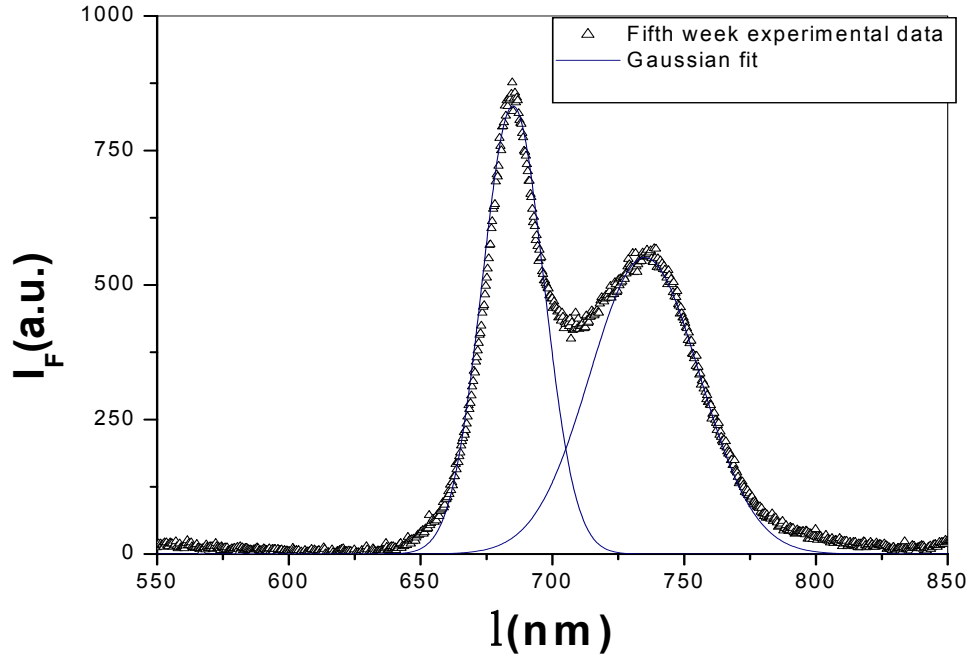


FIG. 2. Chlorophyll a fluorescence spectra for the summer condition cotton at the fifth measuring week with Gaussian curve fitting for $I_F 685/I_F 733$ bands.

TABLE 2A. Winter condition. Parameters for $I_F 685$ band.

W_n	λ_{\max} (nm)	$\Delta\lambda$ (nm)	A (m^2)	I_F (a. u.)
W_5	685.5 ± 0.4	22.8 ± 0.3	0.58 ± 5.0	245.4 ± 0.4
W_6	685.5 ± 0.2	22.5 ± 0.5	1.2 ± 5.5	459.3 ± 0.4
W_7	685.3 ± 0.7	22.1 ± 0.5	1.8 ± 4.0	638.5 ± 0.3
W_8	684.8 ± 0.4	21.6 ± 0.7	2.3 ± 4.4	813.3 ± 0.2

TABLE 2B. Winter condition. Parameters for $I_F 733$ band.

W_n	λ_{\max} (nm)	$\Delta\lambda$ (nm)	A (m^2)	I_F (a. u.)
W_5	732.2 ± 0.8	44.1 ± 0.1	0.87 ± 8.8	166.6 ± 0.5
W_6	731.4 ± 0.5	44.0 ± 0.4	1.58 ± 4.7	298.4 ± 0.6
W_7	731.4 ± 0.4	42.8 ± 0.9	2.33 ± 7.4	403.4 ± 0.2
W_8	730.7 ± 0.2	41.7 ± 0.8	2.81 ± 4.3	508.0 ± 0.2

λ_{\max} : Peak center; $\Delta\lambda$: FWHM; A: Gaussian area; I_F : Fluorescence maximum intensity.

From Table 1 (A and B) for cotton growing in summer conditions, the shifts of λ_{\max} for $I_F 685$ and $I_F 733$ bands as the weeks progressed were 1 nm towards shorter wavelengths and the values of $\Delta\lambda$ decreased with 2 nm and 5 nm, respectively. However, the Gaussian area and the fluorescence intensity increased as the weeks progressed. From Table 2 (A and B) for cotton in winter condition, the shift of λ_{\max} of the $I_F 685$ and $I_F 733$ bands as the weeks progressed, were 1 nm and 2 nm towards the shorter wavelength, and the values of $\Delta\lambda$ decreased with approximately 1 nm and 3 nm, respectively. However, the Gaussian area and the

fluorescence intensity increased. The $I_F 685$ and $I_F 733$ fluorescence intensities are known to be due to Chlorophyll a emission [14, 15]. The peak intensity ratio and the area ratio which are centered about 685 nm and 732 nm, respectively give information about the chlorophyll pigment and are related to plant growth with regard to photosynthesis [16, 17]. Photosystem II emits at a wavelength where the chlorophyll pigments still absorb light. This means that when the chlorophyll content in the leaf increases, photosystem II can not increase at the same rate as photosystem I. Thus the peak intensity ratio and the area ratio of photosystem II are

related to the chlorophyll content and can be used for evaluating the chlorophyll concentration [9]. The peak intensity ratio and also the area ratio against the measuring period for each spectrum of the two groups were calculated from the Gaussian fitting curves and are shown in Table 3 for all the period of measuring.

TABLE 3. Peak intensity ratio (P.I.R.) and area ratio (A.R.) (values are the mean of 10 determinations).

TABLE 3A. Summer conditions

W_n	P. I. R. (± 0.09)	A.R. (± 0.07)
W_3	1.47	0.64
W_4	1.50	0.69
W_5	1.54	0.73
W_6	1.58	0.78
W_7	1.61	0.83
W_8	1.64	0.88

TABLE 3B. Winter conditions

W_n	P.I.R. (± 0.04)	A.R. (± 0.04)
W_5	1.47	0.67
W_6	1.54	0.73
W_7	1.58	0.77
W_8	1.60	0.80

The changes or differences in the values during the measuring period in the two groups depend on Chlorophyll a concentration, thickness of the sample, light scattering properties, geometrical and other factors such as photochemical quenching which causes fluorescence decline by reduction-oxidation state of the first e^- acceptor molecules of PSII [4, 14]. Also it can be due to non-photochemical quenching which include environmental stress, known to induce a strong fluorescence quenching caused by the thylakoid damage [2]. The areas of integrated Gaussians are proportional to their heights such that the intensity of the Chlorophyll a fluorescence could be deduced using the area ratio [6]. Thus, the peak intensity ratio data and that of the area ratio give additional information for monitoring the plant's growth. The changes in the peak intensity ratio and the area ratio versus the measuring period are shown in Fig. 3.

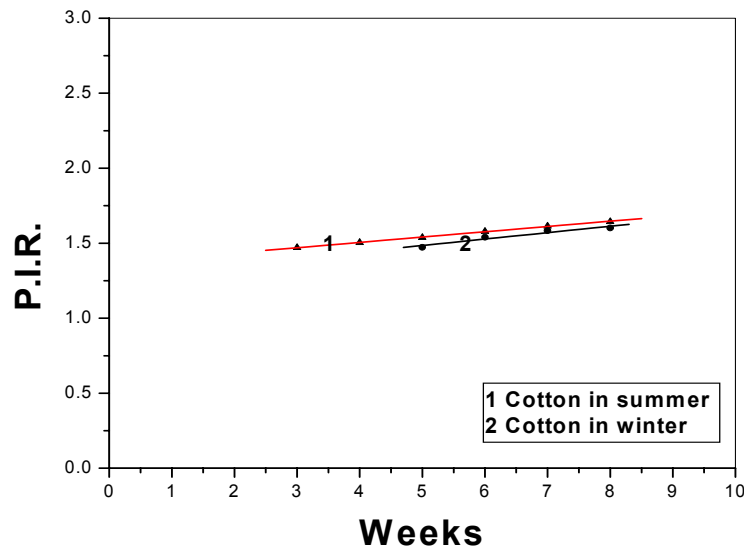


FIG. 3A. For summer conditions; the slope of the line (A) = 1.36 and the intercept of the lines (B) = 0.04; and for winter conditions A = 1.27; B = 0.04

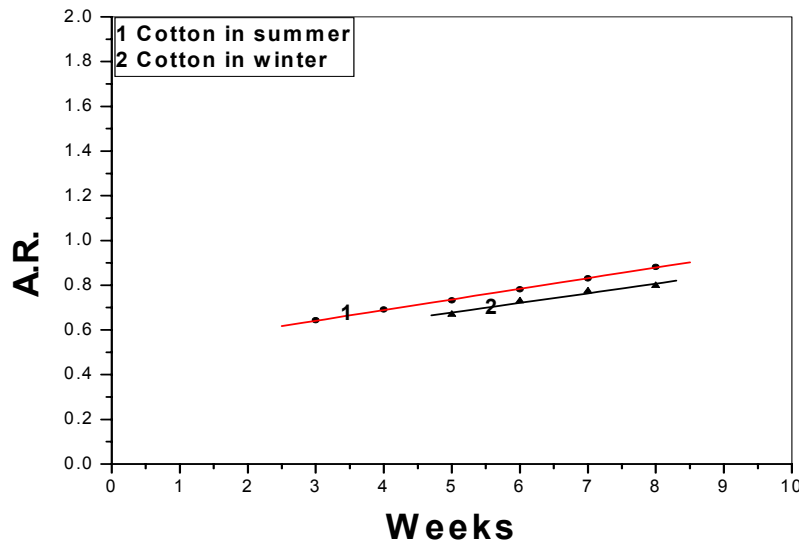


FIG. 3B. For summer conditions: $A = 0.50$; $B = 0.05$; and for winter conditions $A = 0.46$; $B = 0.04$

Discussion

Seed germination, flowering, fruiting and development of cotton is positively influenced by temperature, light intensity and soil moisture [18 - 20]. The results of the present study showed that cotton grown under sunlight summer conditions gave higher and faster germination rates and better growth performance and development compared to those grown under shaded winter conditions. Signs of stress were expressed on the latter cotton group by low growth rates, stunted plants, immaturity and failure of plants to form any flowers. Such results are in agreement with many authors for cotton [21 - 23] and other plants [24 - 26]. The adverse effects of environmental stress on the different plants have been demonstrated by those authors as a reduction in plants' heights, number of primary branches/plant, number of leaves/plant and dry matter production. Superiority of summer group over winter group is also related to the suitable conditions of temperature, light intensity and soil moisture that prevail during summer season. It is worth mentioning that the summer plants receive extra irrigation in the form of rain. As the weeks advanced from germination, summer and winter conditions as well as the peak intensity ratio and the area ratio showed a linear increase rate with time, but differ in slopes and intercepts. The slope of the summer group (1.36) is higher than the winter group (1.27), which shows that the 1st group expressed a better growth relative to

the 2nd group. The lower slope could be an indication for the immaturity and failure of flowering in winter conditions. These results are in an agreement with [9] observations, which showed that the increase of Chlorophyll a concentrations increased the red and far-red fluorescence, however, at high chlorophyll a concentration, only the far-red fluorescence is increased. This can be explained by the fact that plants exhibit two peaks spectra: at 680 and 730 nm corresponding to photosystem II and photosystem I, respectively. The former pigment is known to contain roughly equal amounts of chlorophyll a and b whereas the latter pigment contains a higher ratio of chlorophyll a compared to be [27]. However, our results contradicts with the findings of [28] which showed that fluorescence ratio of I_{F685} and I_{F733} decreased with increasing chlorophyll content of developing leaves. In addition, Ref.[29] and Ref.[16] demonstrated that the Chlorophyll a fluorescence intensity does not usually depend on the Chlorophyll a concentration; but rather on the amount of the light energy absorbed by the leaves. The decrease of Chlorophyll a fluorescence intensity at the early stage of germination is attributed to the small amount of the light energy absorbed because of the small amount of the molecules. The constant increase in the Chlorophyll a fluorescence intensity signal in summer compared to that in winter suggests that Chlorophyll a concentration in summer plants is higher than in winter plants and may be attributed to the environmental stress that

causes thylakoid damage of the winter plants which usually reduces the fluorescence intensity [6]. Such situation may be explained as due to the relatively low temperatures and light intensity in the winter season for shaded plants.

The shift of λ_{\max} towards the shorter wavelength and the decrease of $\Delta\lambda$ value as the weeks advanced; together with the increase of the peak intensity ratio or the area ratio confirm the fact that there was an increase in the Chlorophyll a concentration.

Conclusions

The development of cotton was monitored under summer and winter conditions using I_F685 and I_F733 spectra. All growth parameters of cotton grown under summer condition were higher than in winter conditions due to environmental stress. The peak intensity ratio and the area ratio of

cotton were found to follow a linear relation for the two groups in the two seasons. The curve fitting of the spectra indicated similarities between the peak intensity ratio and the area ratio which reflects the exactness of the Gaussian curves. The ratio I_F685/I_F733 can be used to monitor the development of cotton and probably other plants. Future studies must put into account another way for the determination of Chlorophyll a content using SPAD chlorophyll meter or acetone extract and the chlorophyll activity with chlorophyll fluorescence induction kinetics or CO_2 fixation measurements.

Acknowledgments

The authors extend their gratitude to the Ministry of Higher Education and Research of Sudan for the financial support of this work.

References

- [1] Ndao, A.S., Konte, A., Biaye, M., Faye, M.E., Faye, N.A.B. and Wague, A., J. Fluorescence, 5(2) (2005) 123.
- [2] Blankenship, R.E. "Molecular Mechanisms of Photosynthesis". (Blackwell Science, Arizona, USA, 2002).
- [3] Schreiber, U., Photosynth. Res. 4 (1983) 361.
- [4] Agati, G., Pure Appl. Opt. 7 (1998) 797.
- [5] Buschmann, C., Photosynth. Res. 92 (2007) 261.
- [6] Anderson, B., Buah-Bassuah, P.K. and Tetteh, J.P., Meas. Sci. Technol. 15 (2004) 1255.
- [7] Johnson, G.A. and Day, T.A., Physiologia Plantarum. 116 (2002) 554.
- [8] Wise R.R., Ortiz-Lopez, A. and Ort, D.R., Plant Physiology, 100 (1992) 26.
- [9] Massacci, A., Nabiev, S.M., Pietosani, L., Chernikova, T.N. and Liepner, J., Plant Physiology and Biochemistry, 46 (2008) 189.
- [10] Chappelle, E.W., Wood, Jr.F.M., McMurtrey III, J.E. and Newcomb, W.W., Appl. Opt. 23(1) (1984) 134.
- [11] Gitelson, A.A., Buschmann, C. and Lichtenthaler, H.K., Remote Sens. Environ. 69 (1999) 296.
- [12] Khartoum Meteorological Department, Ministry of Science and Technology, Sudan, (2006).
- [13] Oceanoptics, Inc. USB2000 Manual, (2005). Doc. No. 170-00000-000-02-0305.
- [14] Krause, G.H. and Weis, E., Ann. Rev. Plant Physiol. Plant Mol. Biol. 42 (1991) 313.
- [15] Lichtenthaler, H.K. and Miede, J.A., Trends in Plant Science, 2(8) (1997) 316.
- [16] Lichtenthaler, H.K., Buschmann, C., Rinderle, U. and Schmuck, G., Radiat Environ Biophys. 25 (1986) 297.
- [17] Chappelle, E.W., McMurtrey III, J.E., Wood, Jr.F.M. and Newcomb, W.W., Appl. Opt. 23(1) (1984) 139.
- [18] Ready, V.R., Ready, K.R. and Baker, D.N., Agron. J. 88 (1991) 211.
- [19] Sonza De, F.S., Oosterhuis, D.M., Rosolem, C.A., Gonias, E.D. and Bibi, A.C., AAES Res. 54 (1991) 51.
- [20] Hamza, N.B. and Ahmed, M.F., U. of K. J. Agric. Sci. 16(3) (2008) 352.

- [21] Roussopoulos, D., Liakatus, A. and Whittington, W.J., J. Agron. Sci. 130 (1998) 451.
- [22] Smith, W. and Varvil, J.J., Agron. J. 77 (1985) 9.
- [23] Somoro, A., Mirjat, M.S., Oad, F.C., Somoro, H., Samo, M.A. and Oad, N.L., Online J. Bio. Sci. 1(6) (2001) 472.
- [24] Buttery, B.R. and Stone, J.A., Plant and Soil, 106(2) (1988) 291.
- [25] Pearson, C.J. and Shah, S.G., J. Appl. Ecol. 18 (1991) 897.
- [26] Begna, S.H., Dewyer, D., Cloutier, D., Assemat, L.D., De Tommaso, A., Zahou, X., Prithiviraj, B. and Smith, D.L., J. Exp. Bot. 53(376) (2002) 1935.
- [27] Nelson, D.L. and Cox, M.M., "Lihninger Principles of Biochemistry", 3rd Ed. (Worth Publishers, New York, 2000) p703.
- [28] Hak, R., Lichtenthaler, H.K. and Rinderle, U., Radiat Environ Biophys. 29 (1990) 329.
- [29] Gopal, R., Mishra, K.B., Zeeshan, M., Prasad, S.M. and Joshi, M.M., Current Science, 83(7) (2002) 880.

Multistream Instability in Two and Three–Species Plasmas

M. S. Bawa'aneh^a, G. Assayed^a, M. Shatnawi^a, G. Alna'washi^a and S. Al–Awfi^b

^a*Department of Physics, The Hashemite University, Zarka, Jordan.*

^b*Department of Physics, Faculty of Science, Taibah University, Madina, Saudi Arabia.*

Received on: 3/12/2008; Accepted on: 16/4/2009

Abstract: A detailed parametric investigation of the linear dispersion relation of electron–ion (e–i) and electron–electron–ion (e–e–i) in the hydrogen plasma fluid is carried out in order to determine the different current driven instabilities that can exist in each case. Equations governing the two–stream (e–i) and three–stream (e–e–i) instabilities in cold plasmas are solved numerically and solutions are thoroughly investigated. For the two–stream instability, numerical solutions of the corresponding dispersion relation show the appearance of an unstable mode for $kv_e > 0$, where k is the wave number and v_e is the electron drift speed. Results reported in some references in literature on the peak value of the instability growth rate, when compared with the numerical result, have been found to overestimate the instability maximum growth rate by 17%, while others' estimates coincide with our numerically obtained value. A three–stream instability regime, with two oppositely drifting electron streams with respect to a static ion stream, is also studied; the presence of the third stream has been found to modify the mode spectra by giving rise to a highly unstable mode compared to that observed in the two–stream case. By increasing the number of electrons in the third stream (and keeping a zero net current in the plasma), a red shift in the instability peak value of the growth rate has been observed with an insignificant change in its peak value.

Keywords: Multistream instabilities; Three-species plasma; Kinetic theory.

Introduction

Instabilities which are dependent on the shape of the velocity distribution function are called velocity–space instabilities or micro-instabilities [1, 2]. One example of velocity space instabilities that occur in plasmas is the two–stream instability [3-7], where two interpenetrating streams of a charged particle fluid with different parallel or antiparallel velocities are in many situations unstable.

Heating of plasma with a high–current relativistic electron beam makes essential use of the plasma return current induced by the beam [8]. From overall energy conservation it is concluded that a large fraction of the beam energy is converted into plasma thermal

energy. For reasonable parameters the heating occurs through ion sound turbulence generated by the plasma return current.

Stabilization of the two–stream instability in weakly ionized plasma (equatorial electrojet) has been studied by Sato [9] using fluid equations. It is shown that a macroscopic quasi-linear process acts to reduce the electron flow to a threshold level (ion sound speed), thereby stabilizing the plasma. This result gives an explanation for constant Doppler shifts of radar echoes in the electrojet. It is further shown that the saturation level of the fluctuations agrees with that of observations.

A source of growth of the plasma micro-instability is the change in the free energy density W_0 associated with the relative drifts of the plasma components. Current in plasma is a common source of free energy that leads to an increase in instabilities [10]. It has been pointed out by Hirose [11] that the linear growth of the instability breaks down when the field energy is of the order of $(m_e/m_i)^{2/3}W_0$ and concluded that the anomalous resistivity associated with the instability scales as $(m_e/m_i)^{2/3}$, rather than $(m_e/m_i)^{1/3}$, where m_e and m_i are the electron and ion masses, respectively.

Instabilities that are driven by electron-ion relative drift in two-species Maxwellian plasmas are classified as acoustic instabilities. Such instabilities are most appropriately called two-stream instabilities in case of very high relative drifts (above some characteristic thermal speed) where modes become fluid-like [10]. Also, instabilities are two-stream for zero temperature limits of Maxwellian plasmas where zero-order distribution functions of different species become similar to those shown in Eqs. 3 and 4. S. P. Gary [10] showed instabilities for the two-stream Maxwellian plasma. His results are very similar to dispersion curves obtained for cold plasma especially for plasmas with relative drift velocities larger than thermal velocities. Such extreme situations occur in some regimes (for example in space plasmas [5, 10]). In such regimes, some waves and instabilities have properties that are essentially independent of axial magnetic fields and are charge neutral and bear no steady-state electric fields. So, it is appropriate to investigate the instability of such regimes in non-magnetized quasi-neutral plasmas. Such modes, called ion acoustic-like fluctuations which are essentially electrostatic, are observed in many space plasma contexts such as the solar wind [12, 13, 14] and the earth's bow shock [15].

Ion-electron two-stream instability has been observed experimentally in high intensity accelerators and storage rings [16, 17]. Theoretical studies suggest that the relative streaming motion of the high-intensity particle beam through a background

of charged particles provides the free energy to drive the two-stream instability [18, 19]. A background population of electrons can result by secondary emission when energetic beam particles strike the beam-pipe wall. At low energies and for high charge states the beam can very effectively ionize the residual gas. These secondary electrons can be trapped in the beam electrostatic potential in which electrons can accumulate up to a certain saturation level. Above a certain threshold the accumulated electrons induce two-stream-like instabilities in long bunches [18, 22].

V. Lapuerta and E. Ahedo have done extensive work on two-stream instability (see for example [23, 24, 25]) and on multi-stream instability (see for example [26]). The parametric regions where different types of such instabilities dominate as well as relationship between different instabilities are not very well understood and are being studied. For example, the evolution of the ion-acoustic to Buneman instabilities was studied in ref [24].

The study of multi-stream instabilities is, also, of great interest in beam physics [27, 31]. Ronald C. Davidson and Hong Qin investigated the wall-impedance driven collective instability in intense bunched particle beams using the linearized Vlasov equation [27]. The study included a wide variety of applications ranging from the Harris-like instability driven by large temperature anisotropy to the dipole mode two-stream instability of an intense ion beam propagating through an electron background. Detailed stability properties were determined for dipole-mode perturbations for small axial momentum spread of the beam and for cold beam distribution function in the axial direction, a case that corresponds to the largest instability growth rate. R. Bosch investigated the suppression of two-stream hose instabilities at wavelengths shorter than the transverse length of the beam [28]. Calculations showed stabilization of the two-stream instability when the instability wavelength becomes smaller than the transverse beam length. The same suppression has been observed when a proton beam propagates through a channel that consists of electrons and positive ions.

In recent years, quantum effects have been proven to play an important rule in multi-stream instabilities [32, 37]. Haas *et al.* [32] derived a dispersion relation for the one and two-stream instability by using nonlinear Schrödinger-Poisson system to describe the dynamics of the cold plasma. Anderson *et al.* [33] considered a statistical multi-stream description to prove that a Landau-like damping suppresses the two-stream instability. Ali *et al.* [34, 35] derived a general dielectric constant for a magnetized dusty plasma and finally Haijun *et al.* [36, 37] used quantum hydrodynamic equations to derive a general dispersion relation for one and two-stream plasma.

The main objective of this work is to fill a gap in the detailed investigation of the general dispersion relation of the case of the three-stream instability. Numerical calculations presented in this paper for streaming instability in a cold, collision-less plasma account for two and three particle species. In case of three species we have one ion and two electron species. The ratio of the electrons of the second species to the total number of electrons is given by the ratio number r . The first electron species drifts with a velocity of v_{1e} with respect to the ion species, while the second electron species has a drift velocity of v_{2e} with respect to ions. The magnitude of v_{2e} is estimated such that the plasma is quasi-neutral, i.e. the net current is zero, which yields a second electron species drifting opposite to the first one. In section 2, model equations will be presented and applied to the case of two streams. In section 3, the nonlinear dispersion relation for the case of three-stream systems will be derived and solved numerically. In section 4, results and conclusions are given.

Two – Stream Instability

A stream of energetic electrons passing through cold plasma can excite ion waves which will grow rapidly in magnitude at the expense of the kinetic energy of the electrons. In cold, uniform and un-magnetized plasmas, where ions are stationary, electrons have a constant drift velocity v in a reference frame moving with the ion stream. In collision-less non-magnetized plasmas in which the electrostatic approximation is valid so that the

fluctuating fields are described by Poisson's equation, the longitudinal dielectric function ($\varepsilon(k, \omega)$) for multi-species plasmas is given by [10, 31, 32]

$$\varepsilon(k, \omega) = 1 + \sum_j \chi_j(k, \omega), \quad (1)$$

$$\chi_j(k, \omega) = \frac{q_j^2}{m_j \varepsilon_0} \int_{-\infty}^{\infty} \frac{f_{0j}(v)}{(\omega - kv)^2} dv \quad (2)$$

where ε_0 is the electric permittivity for vacuum, χ_j is the electric susceptibility of the j^{th} species of the plasma, ω and k are the frequency and wave number of a specified plasma mode, q_j , m_j are the single particle charge and mass, respectively and the function $f_{0j}(v)$ is the equilibrium velocity distribution function of the j^{th} plasma species.

Consider a static ion species, where ions are taken as an immobile neutralizing background of positive charges, and an electron species that drifts with a relative velocity of v_e with respect to the ions. The equilibrium distribution function for the cold ions is given by

$$f_{0i}(v) = n_{0i} \delta(v), \quad (3)$$

where n_{0i} is the equilibrium ion density. Equilibrium distribution function for the electron species drifting with v_e with respect to ions is given by

$$f_{0e}(v) = n_{0e} \delta(v - v_e), \quad (4)$$

where n_{0e} is the equilibrium electron density. The equilibrium distribution functions considered here are obtained from the zero temperature limit of the Maxwellian distribution function that best describes the individual plasma components with no inhomogeneity or anisotropy in the distribution, namely,

$$\left. \begin{aligned} f(v) &= \frac{n_{0j}}{(2\pi)^{3/2} V_j^3} \exp\left(\frac{-v_j^2}{2V_j^2}\right), \\ V_j^2 &= \frac{k_B T_j}{m_j} \end{aligned} \right\} \quad (5)$$

Substituting for the distribution functions from Eqs. 3 and 4 and using Eq. 2, the plasma dielectric function of Eq.1 becomes

$$\varepsilon(k, \omega) = 1 - \omega_{pe}^2 \left[\frac{Zm_e / m_i}{\omega^2} + \frac{1}{(\omega - kv_e)^2} \right] \quad (6)$$

where $n_{0e} = Zn_{0i}$ is used, Z is the single ion charge state and ω_{pe} is the electron plasma frequency. Eq.6 is solved numerically for ω as a function of the wave number k for $\varepsilon(k, \omega) = 0$ that yields the dispersion properties of the plasma. The number of roots of $\varepsilon(k, \omega)$ for given plasma is determined by the choice of the equilibrium distribution function as well as the number of species considered. For a Maxwellian plasma, $\varepsilon(k, \omega)$ has, in general, an infinite number of roots. Most of such modes are acoustic-like ($\omega_r / k \sim const.$), where ω_r is the real part of the frequency [10]. Usually, the instability (the imaginary part of the frequency) of different modes is of most interest.

In this section we obtain a numerical solution for the fourth order dispersion relation of the two stream instability in

hydrogen plasma with an emphasis on the unstable modes. All figures shown represent the real and/or imaginary parts of the mode frequency ω normalized to ω_{pe} , versus the wave number k normalized to ω_{pe} / v_e , where v_e represents the electron drift velocity with respect to ions.

Eq. 6 has four roots; the full solution for this equation is shown in Fig. 1, where it is obvious from the equation that ignoring the electron drift would leave us with the two real roots $\omega = \pm\omega_{pe}$, which are the two roots starting in Fig. 1 with ± 1 at $kv_e = 0$. This can be verified analytically using Eq.6. Since ω_{pi} is much smaller than ω_{pe} , the solutions of Eq. 6 in the limit of vanishing ion plasma frequency are $\omega = \pm\omega_{pe} + kv_e$. At $k=0$, both solutions starts at +1 and -1. With increasing k both are shifted upward. This confirms qualitatively the numerical results.

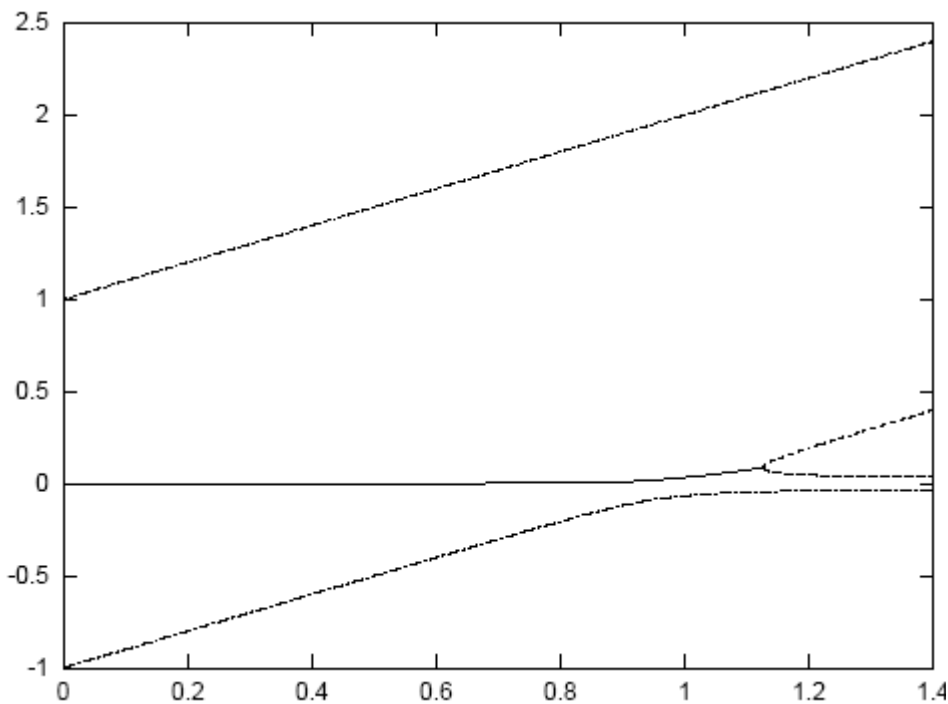


FIG. 1. Real part of the four root solution of Eq.6. Solid line represents two unstable complex conjugate roots. Other lines correspond to real roots.

The presence of the electron drift results in the deviation these two roots as shown in the figure. Also, the presence of the electron drift has given rise to a complex root and its complex conjugate presented in Fig. 1 with the solid line. These unstable roots appear for $kv_e \in (0, 1.12)$, beyond which these complex roots disappear and two new real roots appear maintaining a four-root solution for Eq. 6. The unstable root of Fig. 1 (solid line) is plotted in more detail in Fig. 2 together with its imaginary part shown in dashed line. The instability peaks at $kv_e = \omega_{pe}$ as expected, with $\gamma \approx 0.055\omega_{pe}$, dropping after that to a cut-off wavelength, at $kv_e = 1.12\omega_{pe}$. Here, we can compare the value of the growth rate at $kv_e = \omega_{pe}$, where the instability is maximum, with that known

in literature; In ref. [31, 32], the maximum value is given by

$$\frac{\gamma}{\omega_{pe}} \approx \left(0.5 \frac{m_e}{m_i}\right)^{1/3} \Leftrightarrow \gamma \approx 0.065\omega_{pe}, \quad (7)$$

while that in ref. [27] is given by

$$\frac{\gamma}{\omega_{pe}} \approx \left(\frac{3\sqrt{3}}{16} \frac{m_e}{m_i}\right)^{1/3} \Leftrightarrow \gamma \approx 0.056\omega_{pe} \quad (8)$$

From Fig. 2, the numerical value of the maximum growth rate is about $0.055\omega_{pe}$, which agrees with that maximum value shown in ref. [23] and shows an error of 17% in the formulae obtained in ref. [38, 39]. A similar mode was observed in ref. [10] for hot plasmas.

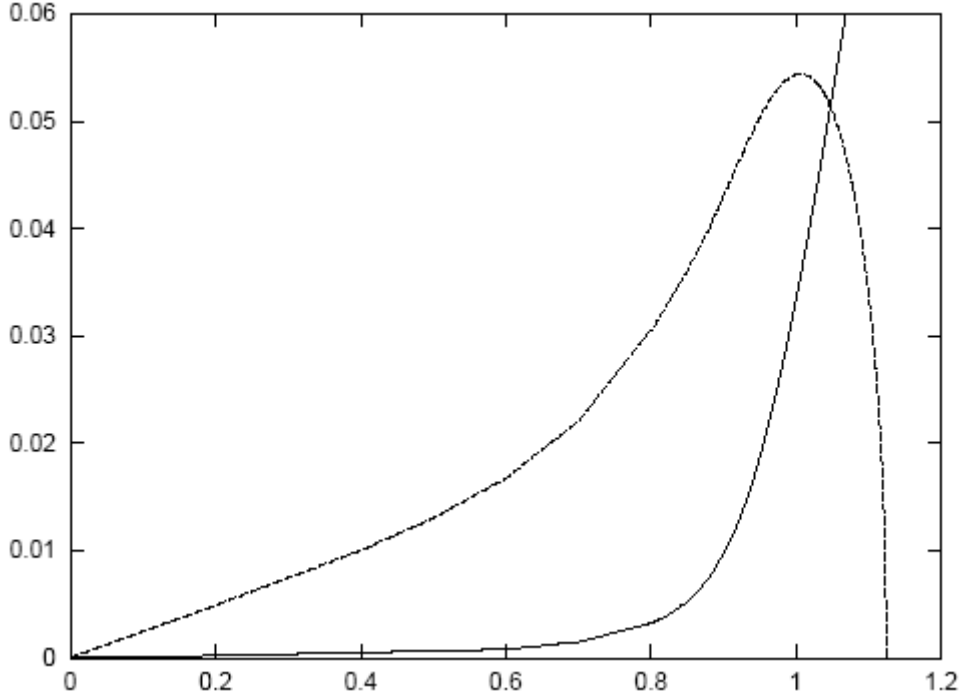


FIG. 2. Real (solid line) and imaginary (dashed line) parts of the frequency versus wave number of the unstable mode for two stream instability.

Three-Stream Instability

In case of three-streams, we consider a system of one ion species and two electron species that drift, relative to ions, with two different speeds given by v_{1e} and v_{2e} in opposite directions. In this case the ion distribution function is still given by Eq.3, while the electron distribution function is given by

$$f_{0e}(v) = n_{0e} \left[\begin{array}{l} (1-r)\delta(v-v_{1e}) \\ + r\delta(v+v_{2e}) \end{array} \right] \quad (9)$$

where r is the ratio of the number of electrons drifting with speed v_{2e} to the total number of electrons. Substituting the values of the distribution functions for the three species from Eqs. 3 and 9 in Eqs. 1 and 2, the dielectric function of the three-stream plasma becomes,

$$\varepsilon(k, \omega) = 1 - \omega_{pe}^2 \left[\frac{Zm_e / m_i + \frac{1-r}{(\omega - kv_{1e})^2}}{\omega^2} + \frac{r}{(\omega + kv_{2e})^2} \right] \quad (10)$$

Note that Eq. 6 for the two-stream case can be obtained from Eq. 10 simply by setting the ratio number r to zero. For $\varepsilon(k, \omega) = 0$, Eq. 10 is solved numerically for ω as a function of the wave number k using different values of ratio r . The speed v_{2e} is estimated relative to v_{1e} such that the net electric current is zero just to keep the quasi-neutrality of the plasma [10].

The configuration of the electron drifts shows two opposite Doppler shifts in the mode frequencies, namely, $\omega_{1,2} = \omega \pm kv_{e1,2}$. To investigate the instability of the three-stream system, we investigate the roots of the sixth order dispersion relation. Four of the six roots are those obtained in the two-stream case, namely roots shown in Fig.

1, and 2 new complex conjugate roots are, also, obtained. Fig. 3 shows the real part of the two additional complex conjugate roots for the three r values 0.1, 0.2, 0.3, where in the case of $r=0$ this mode vanishes. Considering the $r=0.1$ case (solid line), one can see that two complex conjugate roots appear in the kv_{1e} / ω_{pe} interval (0, 0.18), then these two roots disappear and two new real roots appear for $kv_{1e} > 0.18\omega_{pe}$. The corresponding imaginary parts for the modes appearing in Fig. 3 are shown in Fig. 4, where the solid line curve corresponds to the root that is presented in solid line in Fig. 3. The instability is about five times higher than that shown in Fig. 2 for the other unstable mode, and appears for values of k much lower (higher wavelength) than those for the other unstable mode. Increasing the r -value enhances the instability and blue shifts the maximum value.

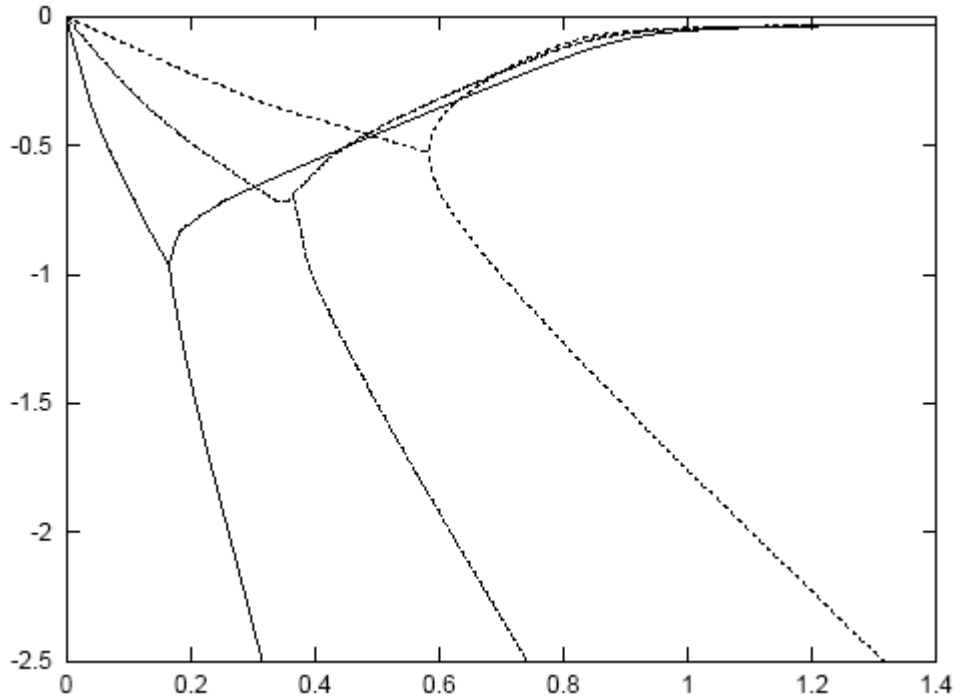


FIG. 3. Real part of the two new roots resulting from the solution of Eq.10. Unstable complex conjugate roots split into two real roots beyond some kv_{1e} / ω_{pe} value. Roots from left to right correspond to $r = 0.1, 0.2, 0.3$, respectively, where solid line corresponds to $r = 0.1$.

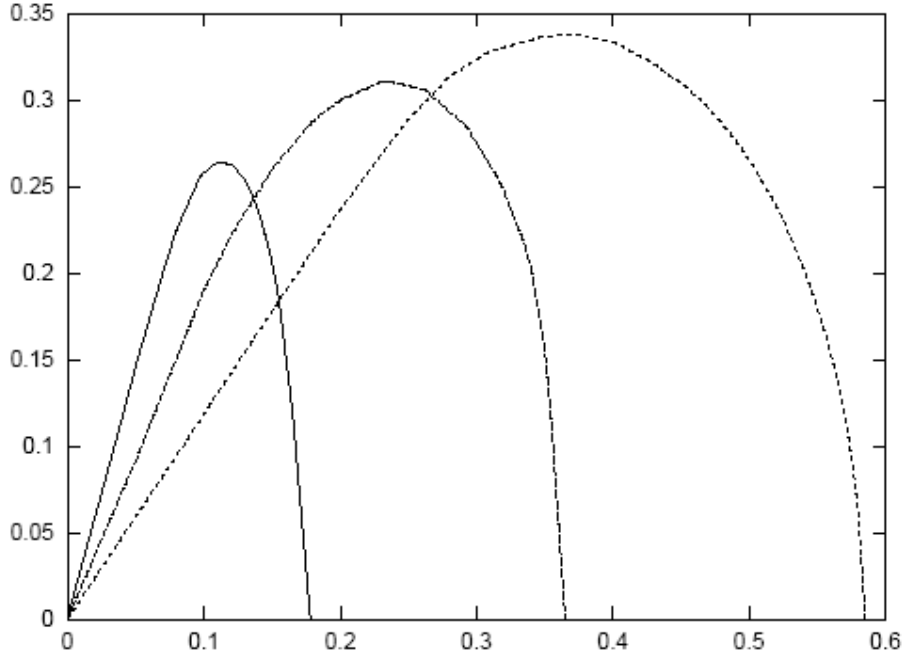


FIG. 4. Imaginary part of the unstable complex roots shown in Fig. 3, where complex roots have a cut-off at some kv_{1e} / ω_{pe} value. Peaks from left to right correspond to $r=0.1, 0.2, 0.3$, respectively.

In the rest of this section we will again consider hydrogen plasma and track the other modes of Eq. 10 shown in Fig. 1 and see the effect of introducing the new electron stream on this mode; the two real modes that start in Fig. 1 with ± 1 values are shown in Figs. 5 and 6 for values of $r = 0, 0.1, 0.2, 0.3$, where the solid line represents the case $r = 0$, i.e. the two-stream system. As can be seen, nothing much happens to the root starting with

$\omega \approx +\omega_{pe}$ at $kv_{1e} = 0$, while the root that starts with $\omega \approx -\omega_{pe}$ at $kv_{1e} = 0$ changes from convergence to zero for higher kv_{1e} values in case of $r = 0$ to divergence as r increases. This shift down in the curves of Figs. 5 and 6 as r increases may be explained as a result of larger negative v_{2e} leading to this down shift.

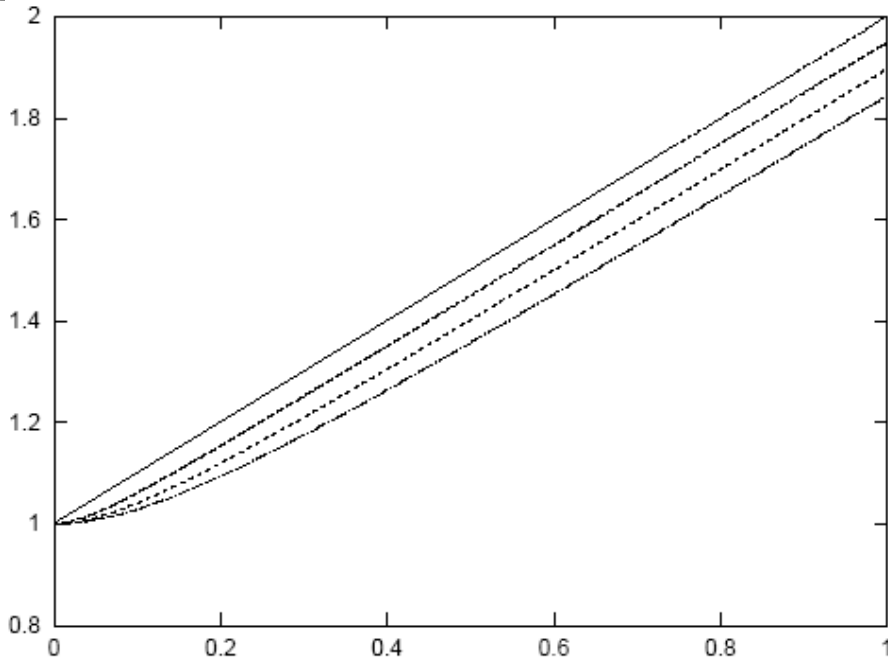


FIG. 5. Stable mode appearing in Fig. 1 for two-stream case (solid line with $r=0$), but here for three-stream case with r -values given by 0, 0.1, 0.2, 0.3, respectively.

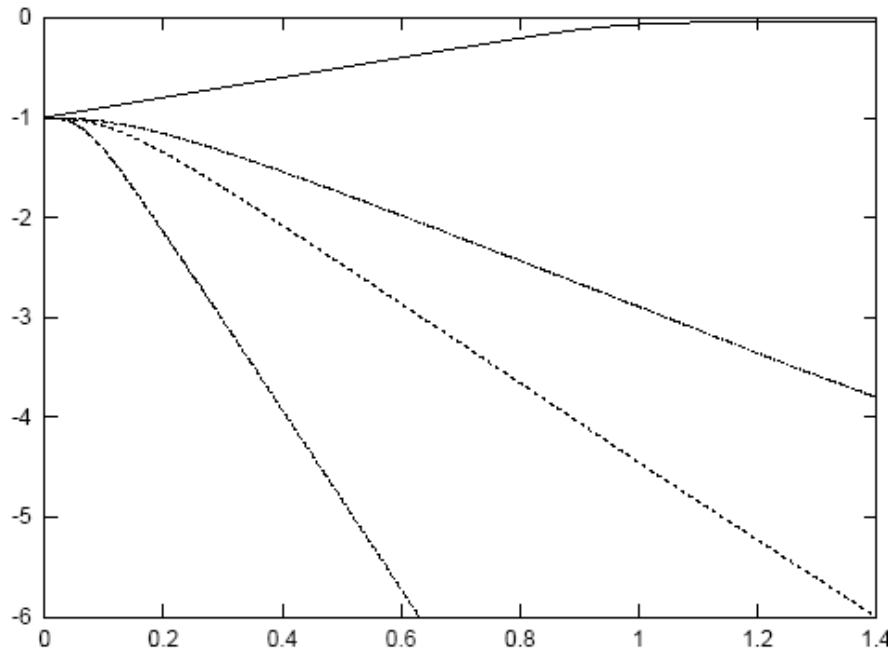


FIG. 6. Stable mode appearing in Fig. 1 for two-stream case (solid line with $r = 0$), but here for three-stream case with r -values given by 0, 0.1, 0.2, 0.3, respectively.

Fig. 7 shows the two complex conjugate roots that disappear at around $kv_{1e} \approx \omega_{pe}$, beyond which two new real roots appear instead (recall Fig. 1). The solid line represents the $r = 0$ case, i.e. the two-stream case, while the other curves represent the cases of $r = 0.1, 0.2, 0.3$, respectively. The

instabilities of these roots are shown in Fig. 8, where, as in Fig. 7, the solid line corresponds to $r = 0$. Other curves correspond to $r = 0.1, 0.2, 0.3$, respectively. Different values of r don't affect the peak value of the growth rate but this peak does red shift as r increases.

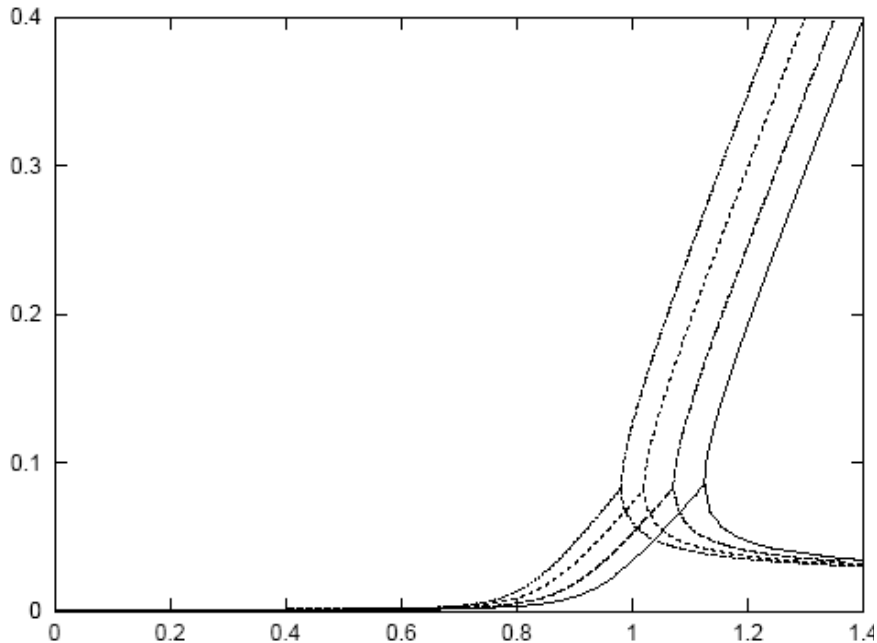


FIG. 7. Two roots appearing in Fig. 1 for two-stream case (solid line with $r = 0$), but here for the three-stream case with r -values given by 0, 0.1, 0.2, 0.3, respectively. Two unstable, complex conjugate roots split into two real roots beyond some kv_{1e} / ω_{pe} value.

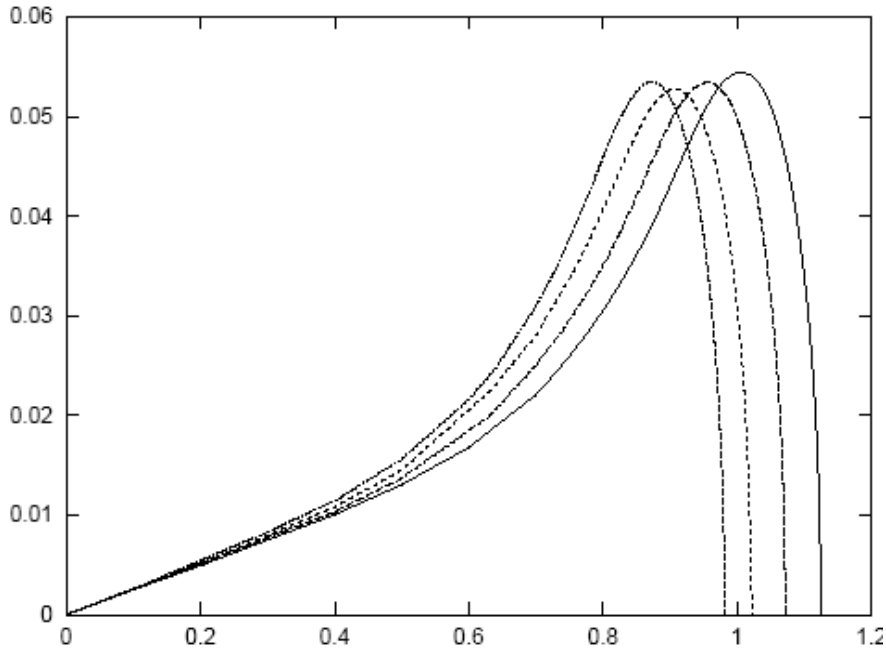


FIG. 8.. Imaginary part of the complex conjugate root of Fig. 7, where solid line represents the two-stream case, i.e. $r = 0$ and the rest of curves represent the $r = 0.1, 0.2, 0.3$ values, respectively.

For diagnostic purposes one can have a look at the “red-shift” of the peak of instability for the two unstable modes ($\Delta\gamma_m$) versus the r -value, where $\Delta\gamma_m$ is the difference in position of the peak value for some r -value and the position of the peak value for $r=0$. Fig. 9 shows the result, where the solid line represents the red shift

for the high instability mode. The relationship is not linear. For the first unstable mode appearing in both two and three stream cases, the red shift tends to a plateau as the r -value increases. For the highly unstable mode, appearing only in $r \neq 0$, the red shift decreases as the r -value increases.

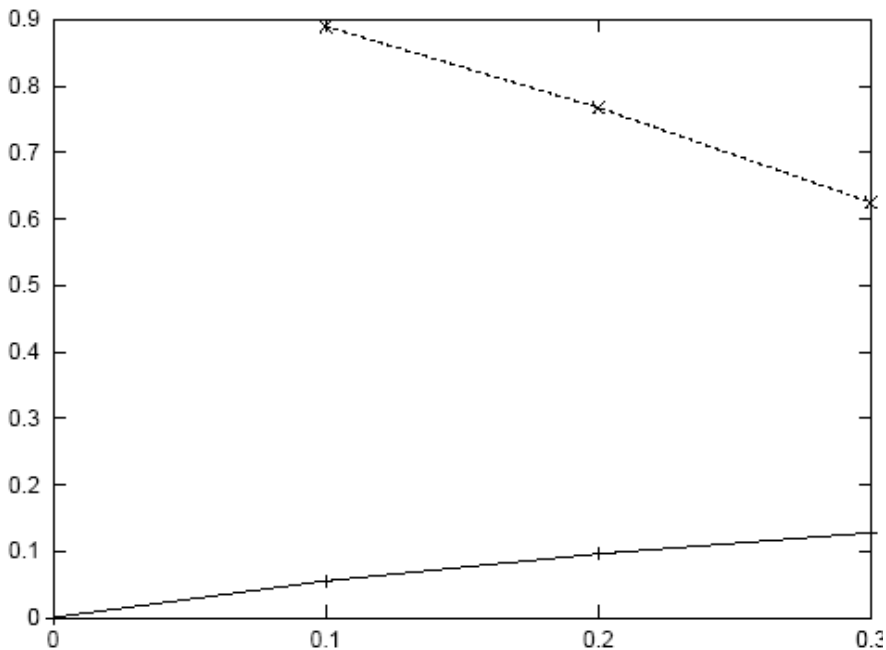


FIG. 9. Shift in position of maximum growth rate $\Delta\gamma_m$ versus r -value. Solid line represents unstable root appearing in two and three stream case. Dotted line represents the other, highly unstable mode appearing in the three-stream case, i.e. $r \neq 0$.

Conclusions

This paper summarizes our investigation on streaming plasma systems, namely e–i two–stream system and e–e–i three–stream system, where numerical solutions for the dispersion relations of the instabilities is considered. For $\varepsilon(k, \omega) = 0$, Eqs. 6 and 10 represent the dispersion relations for the two cases, respectively. In this work the two dispersion relations are solved numerically, where the unstable modes are looked at in detail.

For the two–stream case, two complex conjugate roots corresponding to unstable modes were found. The peak value of the growth rate for this mode obtained from the numerical solution appears at $kv_{1e} = \omega_{pe}$ as expected from Eq.6. It is compared with those approximate values reported in literature, namely Eqs. 7 and 8. The numerical estimates of Fig. 2 show a maximum growth rate of $\gamma = 0.055\omega_{pe}$, coinciding with that maximum of ref. [23] and showing an error of about 17% in the estimates of refs. [38, 39]. This is a good test for the validity of different approximate formulas widely used in literature.

Introducing a third species of electrons, drifting opposite to the first electron species, the ratio r , that represents the percentage of electrons in the second species with respect to the total number of electrons, is found to modify the instability and to give rise to a much more unstable new mode. The drift velocity of the second electron stream with respect to that of the first stream has been estimated such that the net current is zero, i.e.

the relative velocity of the second electron species depends on the percentage number r .

The four modes, observed in the two–stream case, continue to appear in the three–stream case. For the unstable mode, seen in Fig. 2 of the two–stream case, the instability red shifts the peak slightly as the r –value increases, while its maximum doesn't change significantly. The most important result here is the appearance of a new unstable mode with a maximum growth rate of about five times that for the first unstable mode. This instability appears at much lower wavelengths compared to the unstable mode appearing in the two–stream case.

The appearance of this mode can be understood by comparing its frequency appearing in Fig. 3 with that of the other unstable mode shown in the solid line of Fig. 2 and in Fig. 7, where figures show a frequency of this mode close to the plasma frequency in the ion frame of reference. Such a high frequency/high phase speed wave can't interact easily with the heavy ions. In this case, neglecting the first term on the right hand side of Eq. 10, that represents ion contribution, leaves the system closely similar to a two–electron species system that gives a high frequency mode, like this one obtained in this work, with a maximum instability superior to that of the other mode appearing in the two stream and three–stream regime. The instability of such a two, counter streaming, electron gas can be referred to as the electron bi–stream instability.

References

- [1] Krall, N.A. and Liewer, P.C., Phys. Rev. A, 4 (1971) 2094.
- [2] Demchenko, V.V., Nucl. Fusion, 11 (1971) 245.
- [3] Rosenbluth, M.N. and Rostocker, N., Phys. Fluids, 5 (1962) 776.
- [4] Ishihara, O. and Hirose, A., Phys. Rev. Lett. 44 (1980) 1404.
- [5] Gary, S.P., Phys. Fluids, 30 (1987) 2745.
- [6] O'Neil, T.M. and Malmberg, J.H., Phys. Fluids, 11 (1968) 1754.
- [7] Cairns, I.H., Phys. Fluids B, 1 (1989) 204.
- [8] Lovelace, R.V. and Sudan, R.N., Phys. Rev. Lett. 27 (1971) 1256.
- [9] Sato, T., Phys. Rev. Lett. 28 (1972) 732.
- [10] Gary, S.P., "Theory of Space Plasma, Microinstabilities", (Cambridge Uni. Press, 1993).
- [11] Hirose, A., Plasma Phys. 20 (1978) 481.

- [12]Gurnett, D.A., "Waves and instabilities in Physics of the Inner Heliosphere II", (Springer-Verlag, Berlin, 1991).
- [13]Marsch, E., "Kinetic physics of the solar wind plasma, in Physics of the Inner Heliosphere II", (Springer-Verlag, Berlin, 1991).
- [14]Marsch, E., J. Geophys. Res. 90 (1985) 6327.
- [15]Gurnett, D.A., "Plasma waves and instabilities, in Collisionless Shocks in the Heliosphere": Review of Current Research, Geophysical Monograph 35, (American Geophysical Union, Washington DC, 1985).
- [16]Neuffer, D. *et al.*, Nucl. Instr. Methods Phys. Res. A, 321, (1992) 1.
- [17]Giovannozzi, M., Metral, E., Metral, G., Rumolo, G. and Zimmermann, F., Phys. Rev. ST Accel. Beams, 6 (2003) 010101.
- [18]Keil, E. and Zotter, B., CERN-ISH-TH/71-58, Technical report, (CERN, 1971).
- [19]Laslett, L.J., Sessler, A.M. and Moehl, D., Nucl. Instr. Methods Phys. Res. 121 (1974) 517.
- [20]Rumolo, G., Bellodi, G., Ohmi, K. and Zimmermann, F., "Proc. of EPAC 2004", (Published by the European Physical Society Accelerator Group EPS-AG 1963-65).
- [21]Zenkevich, P., Mustafin, N. and Boine-Frankenheim, O., "Proc. of ELOUD 2002", (Yellow Report CERN, 2002-001).
- [22]Zhang, S.Y. *et al.*, Phys. Rev. ST, 8 (2005) 123201.
- [23]Lapuerta, V. and Ahedo, E., Phys. Plas. 9 (2002) 1513.
- [24]Ahedo, E. and Lapuerta, V., Phys. Plas. 8 (2001) 3873.
- [25]Lapuerta, V. and Ahedo, E., Phys. Plas. 7 (2000) 2693.
- [26]Lapuerta, V. and Ahedo, E., Phys. Plas. 9 (2002) 3236.
- [27]Davidson, R.C. and Qin, H., Phys. Rev. ST Accel. Beams, 6 (2003) 104402.
- [28]Bosch, R.A., Phys. Rev. ST Accel. Beams, 6 (2003) 074201.
- [29]Blaskiewicz, M. *et al.*, Phys. Rev. ST Accel. Beams, 6 (2003) 014203.
- [30]Anderson, D. *et al.*, Phys. Rev. E, 65 (2002) 046417.
- [31]Channell, P.J., Phys. Rev. ST Accel. Beams, 5 (2002) 114401.
- [32]Haas, F., Manfredi, G. and Fexi, M., Phys. Rev. E, 62 (2000) 2763.
- [33]Anderson, D. *et al.*, Phys. Rev. E, 65 (2002) 046417.
- [34]Ali, S. and Shukla, P.K., Eur. Phys. J. D, 41 (2007) 319.
- [35] Ali, S. and Shukla, P.K., Phys. Plasmas, 15 (2008) 044503.
- [36]Ren, H., Wu, Z.W., Cao, J. and Chu, P.K., J. Phys. A: Math. Theo., 41 (2008) 115501.
- [37]Ren, H., Wu, Z.W., Cao, J. and Chu, P.K., Phys. Plasmas, 15 (2008) 082103.
- [38]Chen, F.F., "Introduction to Plasma Physics and Controlled Fusion", Vol. I, (Plenum Press, New York and London, 1985).
- [39]Nicholson, D.R., "Introduction to Plasma Theory", (John Wiley and Sons, NY, 1983).

References

- [1]Einstein, A. *Annalen der Physik*, 49 (1916) 160.
- [2]Newton, I. "Opticks", (Dover, New York, 1979).
- [3]Silverman, M.P. *Am. J. Phys.* 48(1) (1981) 72.
- [4]Gine, J. *Chaos Solitons Fractals*, 35(1) (2008) 1.
- [5]Anderson, M.G. *Phys. Lett. A*, 122, 6-7 (2004) 299.
- [6]Finelli, F., Galaverni, M. and Gruppuso, A. *Phys. Rev. D*, 75 (2007) 043003.
- [7]Rindler, W. and Ishak, M. *Phys. Rev.* 76 (2007) 043006.
- [8]Ishak, M. *Phys. Rev. D*, 78 (2008) 103006.
- [9]Dodelson, S. "Modern Cosmology". (Amsterdam, The Netherlands Academic, 2003).
- [10]Lewis, A. and Challinor, A. *Phys. Rep.* 492 (2006) 1.
- [11]Dodelson, S. and Vale, C., *J. Phys. A: Math. Theor.* 40 (2007) 6621.
- [12]Beloborodov, A.M., *Astrophys. J.* 556 (2002) L85.
- [13]Poutanen, J. and Gierlinski, M., *Mon. Not. Astron. Soc.* 343 (2003) 1301.
- [14]Viironen, K. and Poutanen, J. *Astronomy & Astrophysics*, 426 (2004) 985.
- [15]Weinberg, S. "Gravitation and Cosmology". (John Wiley and Sons. Ince., 1972).

حيث $r_g = 2GM/c^2$ ويمثل نصف قطر شوارزجايلد، وبذلك تكون المعادلة (24):-

$$1 - \cos \alpha = (1 - \cos \psi) \left(1 - \frac{r_g}{R}\right) \quad (25)$$

التي تمثل معادلة مسار الضوء بوصفه دالة لزاوية الهروب. واستنادا إلى المعادلة (25) نحصل على العلاقات:-

$$1 - \cos \psi = \frac{(1 - \cos \alpha)}{(1 - r_g / R)} \quad (26.a)$$

وبعمليات حسابية نحصل على:-

$$1 + \cos \psi = 2 - \frac{1 - \cos \alpha}{1 - r_g / R} \quad (26.b)$$

واستنادا إلى العلاقة:-

$$\sin^2 \psi = 1 - \cos^2 \psi, \text{ there for,}$$

$$\sin^2 \psi = (1 - \cos \psi)(1 + \cos \psi) \quad (26.c)$$

وباستخدام العلاقات (26.a), (26.b), (26.c) في المعادلة (23) نحصل على:-

واستنادا إلى المعادلتين (13) و(15) نحصل على:-

$$\psi = \int_R^\infty -\frac{b}{r^2} \left[1 - \frac{b^2}{r^2} B(r)\right]^{-1/2} dr \quad (22)$$

وهذه تتطابق تماما مع ما توصل إليه [12] باستخدام تعريف الخط الضوئي

$$U^\mu U_\mu = 0$$

ومن المعادلة (20) و(21) نحصل على معادلة مسار الضوء:-

$$r(\psi) = \left[\frac{r_g^2}{4} \frac{(1 - \cos \psi)^2}{(1 + \cos \psi)^2} + \frac{b^2}{\sin^2 \psi} \right]^{1/2} - \frac{r_g}{2} \frac{(1 - \cos \psi)}{(1 + \cos \psi)} \quad (23)$$

بدلالة زاوية الهروب، وأيضا على علاقة تربط زاويتي الهروب والانبعاث:

$$1 - \cos \alpha = (1 - \cos \psi) B(r) \quad (24)$$

فإذا ما استخدمنا حل شوارزجايلد المتمثلة عناصره في:-

$$B(r) = A^{-1}(r) = 1 - \frac{2GM}{Rc^2} = 1 - \frac{r_g}{R}$$

$$r(\alpha) = \left[\frac{r_g^2}{4} \left(\frac{(1 - \cos \alpha)/(1 - r_g / R)}{2 - ((1 - \cos \alpha)/(1 - r_g / R))} \right)^2 + \frac{b^2}{((1 - \cos \alpha)/(1 - r_g / R))(2 - (1 - \cos \alpha)/(1 - r_g / R))} \right]^{1/2} - \frac{r_g}{2} \frac{(1 - \cos \alpha)/(1 - r_g / R)}{2 - ((1 - \cos \alpha)/(1 - r_g / R))} \quad (27)$$

معناه ارتداد الإشعاع إلى الخلف ونلاحظ أيضا أن مقدار زاوية الارتداد يعتمد على موقع الانبعاث فحسب. ويتصرف الضوء بنفس الطريقة في حالة الانبعاث بزاوية أكبر من القائمة.

من كل ما سلف يتضح أن شدة الضوء الذي يصلنا من مناطق ذات مجال جذبي شديد النجوم النيوترونية مثلا هو أقل من المنبعث عن المصدر وهي مسالة بالغة الأهمية في الدراسات الكونية والفلكية التي تعتمد على شدة الضوء الواصل إلى المراقب.

التي تمثل مسار الضوء بدلالة زاوية الانبعاث.

المناقشة

تشير معادلة (26.a) إلى أن الضوء المنبعث بزاوية صفر من أية نقطة في المجال الشديد- يهرب بالزاوية نفسها، وهذا معناه بحسب المعادلة (1) انه لا ينحني بتأثير المجال الجذبي. كما تشير إلى ان الضوء المنبعث بزاوية قائمة يهرب بزاوية سالبة بالنسبة لاتجاه المراقب بغض النظر عن موقع نقطة الانبعاث. وهذا

$$U^1 = \left(1 - \frac{b^2}{r^2} B(r)\right)^{1/2} \quad (15)$$

وباستخدام عملية خفض الرموز (Lowering of index) - $(U_\mu = g_{\mu\nu} U^\nu)$ - ومن $U^0 = 1$ و $g_{00} = 1$ ومن المعادلة (15) و $g_{11} = A(r)$ والمعادلة (13) و $g_{33} = r^2$ نحصل على المركبات التغيرية (Covariant) :-

$$U_0 = B(r) \quad (16)$$

$$U_3 = b$$

$$U_1 = \left(A^2(r) - \frac{b^2}{r^2} A(r)\right)^{1/2}$$

ومنها نحصل على :-

$$U^1 U_1 = A(r) - \frac{b^2}{r^2} \quad (17)$$

$$U^3 U_3 = \frac{b^2}{r^2} \quad (18)$$

واستنادا إلى الشكل (1) نحدد زاوية انبعاث الضوء :-

$$\sin \alpha = \sqrt{\frac{U^3 U_3}{U^3 U_3 + U^1 U_1}} \quad (19)$$

وباستخدام المعادلتين (17) و (18) في المعادلة (19) نحصل على :-

$$\sin \alpha = \frac{b/r}{\sqrt{A(r)}} \quad (20)$$

$$\sin \alpha = \frac{b}{r} B^{1/2}(r)$$

أما زاوية الهروب فإنها تنتج عن تغير مركبات السرعة المماسية والقطرية. وهذا يعني ان زاوية هروب الضوء تتشكل من مجموعة التغيرات باتجاهي 1 و 3 لشعاع الضوء من نقطة انبعاثه بزاوية α عند $r = R$ إلى أن يصل إلى $(r = \infty)$ والتي نعبر عنها بالتكامل على طول المسار من نقطة الانبعاث إلى نقطة الهروب.

$$\psi = \int_R^\infty -\frac{U^3}{U^1} dr \quad (21)$$

المعادلتان (10) و (11) تعينان ان الكميات بين الأقواس تمثل ثوابت بالنسبة للمتغير p . والتي يمكن ان نحصل منها على المركبات اللاتغيرية (Contravariant) للسرعة باتجاه الإحداثيات (t, r, ϕ) :-

$$\frac{dt}{dp} = \frac{1}{B(r)} = U^t \quad (12)$$

U^t تمثل مركبة سرعة الضوء باتجاه الإحداثي الزمني، والتي تكتب عادة بالصيغة (U^0) .

$$r^2 \frac{d\phi}{dp} = \text{constan } t = b$$

$$\frac{d\phi}{dp} = \frac{b}{r^2} = U^\phi = U^3 \quad (13)$$

حيث إن U^ϕ أو U^3 تمثل مركبة سرعة الضوء باتجاه الاحداثي ϕ . و b ثابت الحركة - الذي يمثل الزخم الزاوي لوحدة الكتلة إذا كانت معادلة الحركة لجسم كتلوي، ويمثل عرض الحزمة (Impact parameter) في حالة الأشعة الكهرومغناطيسية.

و للحصول على مركبة سرعة الضوء النصف قطرية U^r نستخدم المعادلتين (12) و (13) في المعادلة (6) فنحصل على :-

$$A(r) \left(\frac{dr}{dp}\right)^2 + \frac{b^2}{r^2} - \frac{1}{B(r)} = 0 \quad (14)$$

نضرب المعادلة (14) ب $[A(r)]^{-1}$ فنحصل على :-

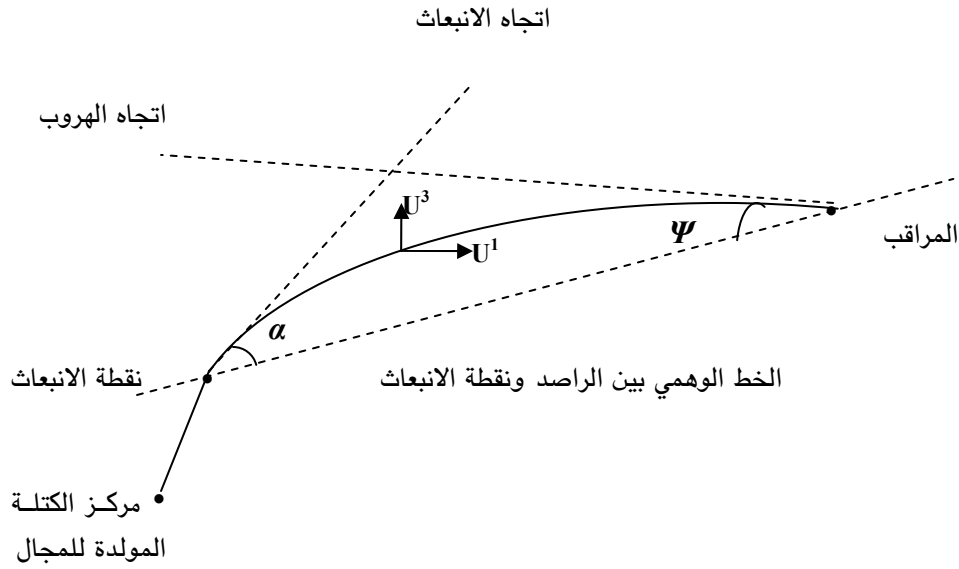
$$\left(\frac{dr}{dp}\right)^2 + \frac{b^2}{r^2 A(r)} - \frac{1}{B(r)A(r)} = 0$$

$$\left(\frac{dr}{dp}\right)^2 + \frac{b^2}{r^2 A(r)} - 1 = 0$$

$$\left(\frac{dr}{dp}\right)^2 = 1 - \frac{b^2}{r^2 A(r)} = (U^r)^2 = (U^1)^2$$

ومن $(U^1)^2 = (dr/dp)^2$ التي تمثل مربع مركبة سرعة الضوء نصف القطرية اللاتغيرية نحصل على :-

$$U^1 = \left(1 - \frac{b^2}{r^2 A(r)}\right)^{1/2}$$



الشكل (1). مسار الضوء المنبعث بزاوية انبعاث α من نجم نيوتروني ومرصود بزاوية هروب Ψ

$\mu=2$

$$\frac{d^2\theta}{dp^2} + \frac{2}{r} \frac{d\theta}{dp} \frac{dr}{dp} - \sin\theta \cos\theta \left(\frac{d\phi}{dp} \right)^2 = 0 \quad (7)$$

$\mu=3$

$$\frac{d^2\phi}{dp^2} + \frac{2}{r} \frac{d\phi}{dp} \frac{dr}{dp} + 2 \cot\theta \frac{d\phi}{dp} \frac{d\theta}{dp} = 0 \quad (8)$$

$\mu=0$

$$\frac{d^2t}{dp^2} + \frac{B'(r)}{B(r)} \frac{dt}{dp} \frac{dr}{dp} = 0 \quad (9)$$

التي تصف مسار الضوء بدلالة الإحداثيات الكروية الأربعة. ولأن الفضاء الكروي هو فضاء متماثل (isotropic) فسنأخذ مسار الضوء الواقع ضمن المستوي $(\theta = \pi/2)$. وهذا يعني إن $(d\theta = 0)$. وهذا الافتراض يحقق المعادلة (7).

نضرب المعادلة (8) بـ $(dp/d\phi)$ والمعادلة (9) بـ (dp/dt) ، ومن تعريف تفاضل الدالة اللوغارتمية نحصل

$$\frac{d}{dp} \left[\ln \frac{d\phi}{dp} + \ln r^2 \right] = 0 \quad (10)$$

$$\frac{d}{dp} \left[\ln \frac{dt}{dp} + \ln B \right] = 0 \quad (11)$$

بالتعويض عن عناصر $g_{\mu\nu}$ من المعادلة (2) في المعادلة (4) نحصل على قيم $\Gamma_{\nu\lambda}^{\mu}$ غير الصفيرية [15]:-

$$\left. \begin{aligned} \Gamma_{rr}^r &= \frac{1}{2A(r)} A'(r) & \Gamma_{\theta\theta}^r &= -\frac{r}{A(r)} \\ \Gamma_{\phi\phi}^r &= -\frac{r \sin^2 \theta}{A(r)} & \Gamma_{tt}^r &= \frac{1}{2A(r)} B'(r) \\ \Gamma_{r\theta}^{\theta} &= \Gamma_{\theta r}^{\theta} = \frac{1}{r} & \Gamma_{\phi\phi}^{\theta} &= -\sin\theta \cos\theta \\ \Gamma_{\phi r}^{\phi} &= \Gamma_{r\phi}^{\phi} = \frac{1}{r} & \Gamma_{\phi\theta}^{\phi} &= \Gamma_{\theta\phi}^{\phi} = \cot\theta \\ \Gamma_{tr}^t &= \Gamma_{rt}^t = \frac{1}{2B(r)} B'(r) \end{aligned} \right\} (5)$$

الفتحة في أعلى الرمز تعني التفاضل بالنسبة لـ (r) . وباستخدام المعادلات (5) في معادلة الحركة (3) نحصل على معادلات الحركة للمحاور الأربعة:-

$\mu=1$

$$\frac{d^2r}{dp^2} + \frac{A'(r)}{2A(r)} \left(\frac{dr}{dp} \right)^2 - \frac{r}{A(r)} \left(\frac{d\theta}{dp} \right)^2 - r \frac{\sin^2 \theta}{A(r)} \left(\frac{d\phi}{dp} \right)^2 + \frac{B'(r)}{2A(r)} \left(\frac{dt}{dp} \right)^2 = 0 \quad (6)$$

المرصود والخط الوهمي بين الراصد ونقطة الانبعاث -
وزاوية انبعائه:

$$\beta = \psi - \alpha \quad (1)$$

فان هذا يعني أن زاوية الانحناء ستتأثر مباشرة
بزاوية الانبعث.

ولأننا نتعامل مع مجالات جاذبية شديدة في موقع
الانبعاث - النجوم النيوترونية - فإننا سنستخدم المعالجة
المعتمدة على نظرية النسبية العامة باعتبارها النظرية
الأكثر دقة في التعامل مع المجالات الجاذبية الشديدة
المرتبطة بالثقوب السوداء أو النجوم النيوترونية أو أي
كتل عملاقة تفوق كتلة الشمس.

العلاقة بين زاويتي الانبعث والانحناء

لدراسة انحناء الضوء المنبعث من مجال جاذبي
شديد باتجاه مجال جاذبي ضعيف، سنفترض ضوءاً
ينبعث من فضاء قرب نجم نيوتروني - كما في الشكل
(1):-

وإن هذا الفضاء يصفه الخط الأولي (line
element)

$$d\tau^2 = g_{\mu\nu} dx^\mu dx^\nu$$

$$d\tau^2 = B(r)dt^2 - A(r)dr^2 - r^2 d\theta^2 - r^2 \sin^2 \theta d\phi^2 \quad (2)$$

حيث إن $B(r) = A^{-1}(r)$ دالة للمكان. وسنستخدم
معادلة الحركة العامة في المجال جاذبي لوصف مسار
الضوء.

$$\frac{d^2 x^\mu}{dp^2} + \Gamma_{\nu\lambda}^\mu \frac{dx^\nu}{dp} \frac{dx^\lambda}{dp} = 0 \quad (3)$$

حيث p عامل يصف المسار. و (μ, ν, λ) رموز
تأخذ الأرقام (0, 1, 2, 3) تمثل الإحداثيات الكروية
الأربعة (t, r, θ, ϕ) . وإن تكرار أي منها يعني وجود
جمع على الأبعاد الأربعة. و $\Gamma_{\nu\lambda}^\mu$ علاقة الربط الريمانية
التي تعرف:-

$$\Gamma_{\nu\lambda}^\mu = \frac{1}{2} g^{\mu\rho} (g_{\rho\nu,\lambda} + g_{\rho\lambda,\nu} - g_{\nu\lambda,\rho}) \quad (4)$$

(الفارزة تعني تفاضلا بالنسبة للاحداثي الذي يمثله
الرمز الذي يليها).

وعلى الرغم من أن الدراسات والبحوث- التي درست
ظاهرة انحناء الضوء سواء ما كان منها معتمداً فيزياء
نيوتن أو قوانين البصريات أو نظرية النسبية العامة- قد
اتفقت على أن العاملين الأكثر تأثيراً في زاوية الانحناء
هما الكتلة المولدة للمجال الجاذبي (M) وبعد مسار
الضوء عن مركز هذه الكتلة (r). إلا أن هذين العاملين
ليسوا الوحيدين في التأثير على زاوية الانحناء. فلقد
أظهرت دراسة [6] أن للطاقة السوداء (Dark
energy) تأثيراً في زاوية انحناء الضوء وليس من
تأثير للثابت الكوني (Cosmological constant) فيها،
ولكن [7] اثبتنا وجود تأثير للثابت الكوني، وقام [8]
بحساب هذا التأثير معتمداً على الجهد الجاذبي.

ومن ثم فإن البحث في الثابت الكوني والطاقة
السوداء وظاهرة العدسات الجاذبية (Gravitational
lensing) وأهميتها في دراسات الكون وأبعاد المجرات
وكتلتها وأشكالها وتوزيع الكتل فيها، أدت إلى الاهتمام
المتزايد [9, 10, 11] بدراسة ظاهرة انحناء الضوء في
المجالات الجاذبية.

وإذا ما تأملنا هذه المعالجات -سواء التي تعتمد
فيزياء نيوتن أو النسبية العامة- فإننا سنجد مشتركا في
أسلوب المعالجة يقوم على افتراض اقتراب ضوء منبعث
من مجال جاذبي ضعيف من مجال جاذبي شديد. كما
سنجد ندرة في معالجات ضوء منبعث من مجال جاذبي
شديد باتجاه مجال جاذبي ضعيف، على الرغم من أهمية
مثل هذه المعالجات في دراسة الوماضات (Pulsars)
التي تتكون من نجمين أحدهما نجم نيوتروني [12, 13]
[14] فالومضات المرصودة من مشاهد على الأرض هي
أشعة منبعثة من مجال جاذبي شديد هو مجال النجم
النيوتروني ومرصودة في مجال جاذبي ضعيف هو مجال
الأرض. وعليه فإن دراسة انحراف الضوء في مثل هذه
الحالة سيكون مهماً جداً في دراسة تغير شدة الفيض
القادم إلينا من الوماضات باعتبار أن الانحناء سيؤدي
إلى انحراف مسار الأشعة القادمة إلينا وبالتالي التأثير
على كثافة الفيض المستلمة.

وحيث إن مقدار زاوية انحناء الضوء (β) المنبعث
من مجال جاذبي شديد تتأثر بزاوية انبعائه (α) - التي
هي الزاوية المحصورة بين اتجاه الانبعث والخط
الوهمي الواصل بين نقطتي الانبعث والرصد- باعتبار
أن زاوية الانحناء تمثل الفرق بين زاوية هروب الضوء
(Ψ) - التي هي الزاوية المحصورة بين اتجاه الضوء

المجلة الأردنية للفيزياء

ARTICLE

تأثير زاوية انبعاث الضوء في زاوية انحنائه

M. A. AL-Obayde and S. E. Khaleel

*Physics Department, College of Science, Mosul University, Iraq.**Received on: 16/11/2008; Accepted on: 26/3/2009*

الملخص: يهدف هذا البحث إلى بيان تأثير زاوية انبعاث الضوء من نقطة ما في مجال جاذبي شديد على زاوية انحنائه. لأجل هذا درسنا انحناء الضوء المنبعث من نقطة في مجال جاذبي شديد باتجاه مجال جاذبي ضعيف. إذ قمنا بحل معادلة الحركة لفوتون منبعث من نقطة قرب نجم نيوتروني كروي ساكن - وفقا للنظرية النسبية العامة - لإيجاد مركبات السرعة الرباعية. وبدلالة هذه المركبات وجدنا كلا من زاوية الانبعاث و زاوية الهروب. ثم وجدنا علاقة تربط بين زاويتي الانبعاث والهروب استنتجنا منها ان الضوء المنبعث بالاتجاه القطري لا يعاني انحناء في حين يرتد الضوء المنبعث بزواوية قائمة. كما توصلنا إلى معادلة تصف مسار الفوتون بدلالة زاوية الانبعاث.

كلمات مفتاحية: زاوية انبعاث الضوء، مجال الجذب، زاوية انحناء الضوء، النسبية العامة، زاوية الهروب.

The Effect of the Emission Angle of the Light on Its Bending

Abstract: The aim of this work is to demonstrate the effect of light emission angle from some point in a strong gravitational field of its bending angle. For this purpose, the light bending from a point of high gravitational field to a weaker one is studied. The general relativistic equation of motion of a photon emitted from a point on a spherical static neutron star is solved to find the four velocity components, from these components, both emission angle and escape angle were found. A relation between those two angles is found, from this relation, it is deduced that light emitted in the radial direction suffers no bending while that emitted at right angle is reflected back. A relation relating the photon path and emission angle is also deduced.

Keywords: Light emission angle; Gravitational field; Light bending angle; General relativity; Escape angle.

المقدمة

العلاقة. فقد قام الباحثان [3, 4] بدراسة ظاهرة الانحناء وحساب زاويتها وفق الميكانيك الكلاسيكي. وقام [5] بدراستها وفق قوانين البصريات التي تصف الانكسار عند اختلاف الأوساط البصرية التي يمر من خلالها الضوء.

ولكن هذا لا ينفي أن النظرية النسبية العامة [1] قدمت رياضيات أكثر دقة في دراسة الظاهرة وحساباتها.

لم يكن تنبؤ اينشتاين بانحناء الضوء [1] في الفضاء المحدب هو أول إشارة إلى ظاهرة انحناء الضوء. إذ سبقه نيوتن في الإشارة إليها - بما ينسجم مع نظريته الجسيمية للضوء- في عام (1704) في رسالته في البصريات [2].

وليست نظرية النسبية العامة هي وحدها القادرة على حساب زاوية انحناء الضوء عند اقترابه من الكتل

Authors Index

Ahmed A. M.	103
Al-Awfi S.	113
Alna'washi G.	113
AL-Obayde M. A.	125
Assayed G.	113
Bawa'aneh M. S.	113
Bsoul. I.	95
Husain M. M.	89
Kafi S. T.	103
Khaleel S. E.	125
Lipka J.	73
Medani I. M. K.	103
Najam L. A.	89
Sabir Ali A. K.	103
Shatnawi M.	113
Yousuf R. M.	89

Subject Index

Ball milling	95
Barium ferrite.....	95
Chlorophyll a	103
Coercive field.....	95
Cotton.....	103
CR-39 plastic nuclear track detectors	89
Escape angle	125
Fluorescence	103
General relativity	125
Gravitational field	125
I_{F685}/I_{F733}	103
Kinetic theory	113
Light bending angle	125
Light emission angle	125
Magnetization	95
MCL.....	89
Mössbauer spectroscopy	73
Multistream instabilities.....	113
Neutron embrittlement.....	73
Neutron irradiation.....	73
Positron annihilation	73
Radon -222 concentration levels.....	89
Reactor pressure vessel steels	73
Summer and winter conditions	103
Three-species plasma	113

المناقشة: يجب أن تكون موجزة وتركز على تفسير النتائج.

الاستنتاج: يجب أن يكون وصفا موجزا لأهم ما توصلت إليه الدراسة ولا يزيد عن صفحة مطبوعة واحدة.

الشكر والعرفان: الشكر والإشارة إلى مصدر المنح والدعم المالي يكتبان في فقرة واحدة تسبق المراجع مباشرة.

المراجع: يجب طباعة المراجع بأسطر مزدوجة ومرقمة حسب تسلسلها في النص. وتكتب المراجع في النص بين قوسين مربعين. ويتم اعتماد اختصارات الدوريات حسب نظام Wordlist of Scientific Reviewers.

الجدول: تعطى الجداول أرقاماً متسلسلة يشار إليها في النص. ويجب طباعة كل جدول على صفحة منفصلة مع عنوان فوق الجدول. أما الحواشي التفسيرية، التي يشار إليها بحرف فوقي، فتكتب أسفل الجدول.

الرسوم التوضيحية: يتم ترقيم الأشكال والرسومات والرسومات البيانية (المخططات) والصور، بصورة متسلسلة كما وردت في النص.

تقبل الرسوم التوضيحية المستخرجة من الحاسوب والصور الرقمية ذات النوعية الجيدة بالأبيض والأسود، على أن تكون أصيلة وليست نسخة عنها، وكل منها على ورقة منفصلة ومعرفة برقمها بالمقابل. ويجب تزويد المجلة بالرسومات بحجمها الأصلي بحيث لا تحتاج إلى معالجة لاحقة، وألا تقل الحروف عن الحجم 8 من نوع Times New Roman، وألا تقل سماكة الخطوط عن 0.5 وبكثافة متجانسة. ويجب إزالة جميع الألوان من الرسومات ما عدا تلك التي ستنشر ملونة. وفي حالة إرسال الرسومات بصورة رقمية، يجب أن تتوافق مع متطلبات الحد الأدنى من التمايز (1200 dpi Resolution) لرسومات الأبيض والأسود الخطية، و 600 dpi للرسومات باللون الرمادي، و 300 dpi للرسومات الملونة. ويجب تخزين جميع ملفات الرسومات على شكل (jpg)، وأن ترسل الرسوم التوضيحية بالحجم الفعلي الذي سيظهر في المجلة. وسواء أرسل المخطوط بالبريد أو عن طريق الشبكة (Online)، يجب إرسال نسخة ورقية أصلية ذات نوعية جيدة للرسومات التوضيحية.

مواد إضافية: تشجع المجلة الباحثين على إرفاق جميع المواد الإضافية التي يمكن أن تسهل عملية التحكيم. وتشمل المواد الإضافية أي اشتقاقات رياضية مفصلة لا تظهر في المخطوط.

المخطوط المنقح (المعدل) والأقراص المدمجة: بعد قبول البحث للنشر وإجراء جميع التعديلات المطلوبة، فعلى الباحثين تقديم نسخة أصلية ونسخة أخرى مطابقة للأصلية مطبوعة بأسطر مزدوجة، وكذلك تقديم نسخة إلكترونية تحتوي على المخطوط كاملاً مكتوباً على Microsoft Word for Windows 2000 أو ما هو استجد منه. ويجب إرفاق الأشكال الأصلية مع المخطوط النهائي المعدل حتى لو تم تقديم الأشكال إلكترونياً. وتخزن جميع ملفات الرسومات على شكل (jpg)، وتقدم جميع الرسومات التوضيحية بالحجم الحقيقي الذي ستظهر به في المجلة. ويجب إرفاق قائمة ببرامج الحاسوب التي استعملت في كتابة النص، وأسماء الملفات على قرص مدمج، حيث يعلم القرص بالاسم الأخير للباحث، وبالرقم المرجعي للمخطوط للمراسلة، وعنوان المقالة، والتاريخ. ويحفظ في مغلف واطي.

الفهرسة: تقوم المجلة الأردنية للفيزياء بالإجراءات اللازمة لفهرستها وتلخيصها في جميع الخدمات الدولية المعنية.

حقوق الطبع

يُشكّل تقديم مخطوط البحث للمجلة اعترافاً صريحاً من الباحثين بأن مخطوط البحث لم يُنشر ولم يُقدّم للنشر لدى أي جهة أخرى كانت وبأي صيغة ورقية أو إلكترونية أو غيرها. ويُشترط على الباحثين ملء نموذج يُنصّ على نقل حقوق الطبع لتصبح ملكاً لجامعة اليرموك قبل الموافقة على نشر المخطوط. ويقوم رئيس التحرير بتزويد الباحثين بإنموذج نقل حقوق الطبع مع النسخة المُرسلة للتنقيح. كما ويُمنع إعادة إنتاج أي جزء من الأعمال المنشورة في المجلة من دون إذن خطي مُسبق من رئيس التحرير.

إخلاء المسؤولية

إن ما ورد في هذه المجلة يعبر عن آراء المؤلفين، ولا يعكس بالضرورة آراء هيئة التحرير أو الجامعة أو سياسة اللجنة العليا للبحث العلمي أو وزارة التعليم العالي والبحث العلمي. ولا يتحمل ناشر المجلة أي تبعات مادية أو معنوية أو مسؤوليات عن استعمال المعلومات المنشورة في المجلة أو سوء استعمالها.

معلومات عامة

المجلة الأردنية للفيزياء هي مجلة بحوث علمية عالمية مُحكمة تصدر عن اللجنة العليا للبحث العلمي، وزارة التعليم العالي والبحث العلمي، عمان، الأردن. وتقوم بنشر المجلة عمادة البحث العلمي والدراسات العليا في جامعة اليرموك، إربد، الأردن. وتُنشر البحوث العلمية الأصيلية، إضافة إلى المراسلات القصيرة Short Communications، والملاحظات الفنية Technical Notes، والمقالات الخاصة Feature Articles، ومقالات المراجعة Review Articles، في مجالات الفيزياء النظرية والتجريبية، باللغتين العربية والإنجليزية.

تقديم مخطوط البحث

تُرسل نسخة أصلية وثلاث نسخ من المخطوط، مُرفقة برسالة تغطية من جانب الباحث المسؤول عن المراسلات، إلى رئيس التحرير:

أ.د. ابراهيم أبو الجرايش،

رئيس التحرير، المجلة الأردنية للفيزياء،

عمادة البحث العلمي والدراسات العليا،

جامعة اليرموك، إربد، الأردن.

هاتف : 00 962 2 72 11 111 / فرعي: 3735

فاكس : 00 962 2 72 11 121

بريد إلكتروني : jjp@yu.edu.jo

تقديم المخطوطات إلكترونياً: اتبع التعليمات في موقع المجلة على الشبكة العنكبوتية.

ويجري تحكيم البحوث الأصيلية والمراسلات القصيرة والملاحظات الفنية من جانب مُحكمين اثنين في الأقل من ذوي الاختصاص والخبرة. وتُشجّع المجلة الباحثين على اقتراح أسماء المحكمين. أما نشر المقالات الخاصة في المجالات الفيزيائية النشطة، فيتم بدعوة من هيئة التحرير، ويُشار إليها كذلك عند النشر. ويُطلب من كاتب المقال الخاص تقديم تقرير واضح يتسم بالدقة والإيجاز عن مجال البحث تمهيداً للمقال. وتُنشر المجلة أيضاً مقالات المراجعة في الحقول الفيزيائية النشطة سريعة التغير، وتُشجّع كاتبها مقالات المراجعة أو مُستكثبيها على إرسال مقترح من صفحتين إلى رئيس التحرير. ويُرفق مع البحث المكتوب باللغة العربية ملخص (Abstract) وكلمات دالة (Keywords) باللغة الإنجليزية.

ترتيب مخطوط البحث

يجب أن تتم طباعة مخطوط البحث ببنط 12 نوعه Times New Roman، وبسطر مزدوج، على وجه واحد من ورق A4 (21.6 × 27.9 سم) مع حواشي 3.71 سم، باستخدام معالج كلمات ميكروسوفت وورد 2000 أو ما استُجد منه. ويجري تنظيم أجزاء المخطوط وفق الترتيب التالي: صفحة العنوان، الملخص، رموز التصنيف (PACS)، المقدمة، طرق البحث، النتائج، المناقشة، الخلاصة، الشكر والعرفان، المراجع، الجداول، قائمة بدليل الأشكال والصور والإيضاحات، ثم الأشكال والصور والإيضاحات. وتُكتب العناوين الرئيسية بخط غامق، بينما تُكتب العناوين الفرعية بخط مائل.

صفحة العنوان: وتشمل عنوان المقالة، أسماء الباحثين الكاملة وعناوين العمل كاملة. ويكتب الباحث المسؤول عن المراسلات اسمه مشاراً إليه بنجمة، والبريد الإلكتروني الخاص به. ويجب أن يكون عنوان المقالة موجزاً وواضحاً ومعبراً عن فحوى (محتوى) المخطوط، وذلك لأهمية هذا العنوان لأغراض استرجاع المعلومات.

الملخص: المطلوب كتابة فقرة واحدة لا تزيد على مائتي كلمة، موضحة هدف البحث، والمنهج المتبع فيه والنتائج وأهم ما توصل إليه الباحثون.

الكلمات الدالة: يجب أن يلي الملخص قائمة من 4-6 كلمات دالة تعبر عن المحتوى الدقيق للمخطوط لأغراض الفهرسة.

PACS: يجب إرفاق الرموز التصنيفية، وهي متوافرة في الموقع <http://www.aip.org/pacs/pacs06/pacs06-toc.html>.

المقدمة: يجب أن توضّح الهدف من الدراسة وعلاقتها بالأعمال السابقة في المجال، لا أن تكون مراجعة مكثفة لما نُشر (لا تزيد المقدمة عن صفحة ونصف الصفحة مطبوعة).

طرائق البحث (التجريبية / النظرية): يجب أن تكون هذه الطرائق موضحة بتفصيل كاف لإتاحة إعادة إجرائها بكفاءة، ولكن باختصار مناسب، حتى لا تكون تكراراً للطرائق المنشورة سابقاً.

النتائج: يستحسن عرض النتائج على صورة جداول وأشكال حيثما أمكن، مع شرح قليل في النص ومن دون مناقشة تفصيلية.

Jordan Journal of

PHYSICS

An International Peer-Reviewed Research Journal

Published by the Deanship of Research & Graduate Studies, Yarmouk University, Irbid, Jordan

Name: الأسم:
 Specialty: التخصص:
 Address: العنوان:
 P.O. Box: صندوق البريد:
 City & Postal Code: المدينة/الرمز البريدي:
 Country: القطر:
 Phone: رقم الهاتف:
 Fax No: رقم الفاكس:
 E-mail: البريد الإلكتروني:
 No. of Subscription: عدد الاشتراكات:
 Method of Payment: طريقة الدفع:
 Amount Enclosed: المبلغ المرفق:
 Signature: التوقيع:

Cheques should be paid to Deanship of Research and Graduate Studies - Yarmouk University.

I would like to subscribe to the Journal
For

- One Year
 Two Years
 Three Years

One Year Subscription Rates

	Inside Jordan	Outside Jordan
Individuals	JD 8	€ 40
Students	JD 4	€ 20
Institutions	JD 12	€ 60

Correspondence**Subscriptions and Sales:**

Prof. Ibrahim O. Abu-AlJarayesh
 Deanship of Research and Graduate Studies
 Yarmouk University
 Irbid – Jordan
Telephone: 00 962 2 711111 Ext. 2096
Fax No.: 00 962 2 7211121



جامعة اليرموك



المملكة الأردنية الهاشمية

المجلة الأردنية
للفيزياء
مجلة بحوث علمية عالمية محكمة

المجلد (2)، العدد (2)، 2009م / 1430هـ

المجلة الأردنية
الفيزياء
مجلة بحوث علمية عالمية محكمة

المجلد (2)، العدد (2)، 2009م / 1430هـ

المجلة الأردنية للفيزياء: مجلة بحوث علمية عالمية محكمة أسستها اللجنة العليا للبحث العلمي، وزارة التعليم العالي والبحث العلمي، الأردن، وتصدر عن عمادة البحث العلمي والدراسات العليا، جامعة اليرموك، إربد، الأردن.

رئيس التحرير:

ابراهيم عثمان أبو الجرايش
قسم الفيزياء، جامعة اليرموك، إربد، الأردن.
ijaraysh@yu.edu.jo

هيئة التحرير:

ضياء الدين محمود عرفة
قسم الفيزياء، الجامعة الأردنية، عمان، الأردن.
darafah@ju.edu.jo

نبيل يوسف أيوب
الجامعة الألمانية الأردنية، عمان، الأردن.
nabil.ayoub@gju.edu.jo

هشام بشارة غصيب
رئيس جامعة الأميرة سمية للتكنولوجيا، عمان، الأردن.
ghassib@psut.edu.jo

جميل محمود خليفة
قسم الفيزياء، الجامعة الأردنية، عمان، الأردن.
jkalifa@ju.edu.jo

سامي حسين محمود
قسم الفيزياء، جامعة اليرموك، إربد، الأردن.
mahmoods@yu.edu.jo

مروان سليمان موسى
قسم الفيزياء، جامعة مؤتة، الكرك، الأردن.
mmousa@mutah.edu.jo

نهاد عبد الرؤوف يوسف
قسم الفيزياء، جامعة اليرموك، إربد، الأردن.
nihadyusuf@yu.edu.jo

سكرتير التحرير: مجدي الشناق

ترسل البحوث إلى العنوان التالي:

الأستاذ الدكتور إبراهيم عثمان أبو الجرايش
رئيس تحرير المجلة الأردنية للفيزياء
عمادة البحث العلمي والدراسات العليا، جامعة اليرموك
إربد، الأردن

هاتف 00 962 2 7211111 فرعي 3735

E-mail: jjp@yu.edu.jo

Website: <http://Journals.yu.edu.jo/jjp>

<http://jjp.yu.edu.jo>

